University of Southampton

Southampton Oceanography Centre

School of Ocean and Earth Sciences

Faculty of Science

Process Studies of The Equatorial Pacific Ocean and its Adjustment to Intraseasonal Wind Forcing

Anna Pirani

Thesis for the degree of Doctor of Philosophy

March 2004

Graduate School of the Southampton Oceanography Centre

This PhD dissertation by

Anna Pirani

has been produced under the supervision of the following persons:

Supervisors:

Prof. Peter D. Killworth

Prof. Kelvin Richards

Chair of Advisory Panel:

Prof. Harry L. Bryden

Member of Advisory Panel:

Dr. Neil C. Wells

Per Luisa & Roberto

e i miei nonni

Cesare, Marta, Nino e Antonietta.

UNIVERSITY OF SOUTHAMPTON

ABSTRACT

FACULTY OF SCIENCE
SCHOOL OF OCEAN AND EARTH SCIENCE SOUTHAMPTON
OCEANOGRAPHY CENTRE

Doctor of Philosophy

Process Studies of The Equatorial Pacific Ocean and its Adjustment to Intraseasonal Wind Forcing

BY ANNA PIRANI

MARCH 2004

The role of atmospheric intraseasonal variability on the evolution of the Equatorial Pacific Ocean is addressed in a series of process study experiments. The adjustment of the upper ocean to a Westerly Wind Event (WWE) is modelled with the Océan Parallélisé (OPA) GCM to examine the sensitivity of the oceanic response to the variability of the background state of the Equatorial ocean.

Different ocean conditions are configured in an idealised Equatorial ocean basin, depending on the strength of the background Trade winds and the horizontal viscosity. An analytical WWE is applied and we study the Kelvin wave adjustment and its sensitivity to the background ocean conditions.

The model TIW field exhibits considerable temporal and spatial variability that is sensitive to the model configuration. A viscosity regime of order $10^3 m^2 s^{-1}$ is necessary to simulate a realistic TIW field. The Kelvin wave generates velocity and SST anomalies when it encounters the TIW field and leads to a phase shift of the TIW field.

The Kelvin wave is decomposed into its normal modes and we find that the surface signature of the Kelvin wave is predominantly due to the second baroclinic mode. The Kelvin wave generally has a bimodal structure consisting of the first and second baroclinic modes. The amplitude of the second baroclinic mode is sensitive to the background mean state and is significantly diminished by a strengthened Equatorial circulation and steepened thermocline in the increased background wind field experiments and the low viscosity regime, leading to a weaker surface ocean response.

The results show that the model response to a WWE and its impact on the upper ocean depends on the oceanic conditions at the time of the wind perturbation, with the projection of the WWE onto the ocean modes determining the Kelvin wave structure.

The analysis is extended to consider two observed WWEs, one in March 1997 that led to a strong ocean adjustment during the growth of the 1997 El Niño, and one in December 2002 that did not lead to strong surface anomalies. The baroclinic structure of the Kelvin wave is a factor determining the strength of the ocean response, with the March 1997 WWE having a stronger projection onto the first and second baroclinic modes compared to the December 2002 WWE.

Acknowledgements

I would like to thank Prof. Kelvin Richards for having given me the opportunity to pursue this project, funded by the UK Universities Global Atmospheric Modelling Programme (UGAMP) and a CASE studentship with the European Centre for Mid-Range Weather Forecasts (ECMWF).

I am completely indebted to Prof. Peter Killworth and Mr Jeffery Blundell, without whom I would have never got this far. Thank you for all your patience and the time you took to help me as this encouraged and enabled me to reach the end. I am very fortunate to have had this opportunity to work as a student with you both.

I am very grateful for having being able to spend three months and numerous other visits at the ECMWF. I enjoyed working together and all stimulating discussions that I have had with Prof. Dave Anderson, Dr. Magdalena Alonso Balmaseda, Dr. Jerome Vialard, Dr. Frederic Vitart, Dr. Tim Stockdale, Prof. Tim Palmer, and all the other members of the Seasonal Forecasts team, all of whom made me feel very welcome.

There is nothing I can say that can demonstrate my gratitude and how I feel for how my parents, my grandparents and my family and Riccardo have supported me, kept me going and made me happy always. Chee-Won, Eve, Katherine and Nick have always been there for me and I also want to thank Ossie and the Harragin family. I have been so lucky to have so many wonderful friends, in particular Chess and Lizzie, Angela, all the Italian contingency, Christos, Haris, Xana, Uli, Irene, and my office mates, in particular Maria and Birgit. These have been four long years for me and with out you I would not have managed.

Contents

1 Introduction 1

1.1 Motivations 1

1.2 Objectives and Approaches 3

2 The Equatorial Pacific Region 4

2.1 Climatology 4

2.2 Modes of Variability 6

2.2.1 The El Niño Southern Oscillation 7

2.2.2 The Madden-Julian Oscillation 8

2.3 Intraseasonal Forcing and ENSO 10

2.4 Westerly Wind Events 11

2.5 Summary 13

3 Overview of Model and Experiments 14

3.1 Introduction 14

3.2 The OPA OGCM 14

3.3 The Role of Horizontal Mixing 15

3.4 Process Study Experiments 17

3.4.1 Spin Up Period 17

3.4.2 The Westerly Wind Event 19

3.4.3 Experiment Nomenclature 20

3.5 Summary 22

4 The Model Equatorial Ocean 23

4.1 Introduction 23

4.2 Energy Balance Analysis 28

4.3 Meridional Heat Transport 32

4.4 Summary 35

5 Tropical Instability Waves 36

5.1 Introduction 36

5.2 The Model TIW Field 40

5.2.1 Seasonal Variability 44
5.2.2 Wavelet Analysis 49
5.3 Interactions with a WWE-Forced Kelvin Wave 52
5.3.1 Mixing Sensitivity 57
5.3.2 Sensitivity to Wind Stress Regimes 62
5.3.3 Kinetic Energy Analysis Revisited 64
5.4 Summary 65

6 The Kelvin Wave Adjustment **67**
6.1 Introduction 67
6.2 Equatorial Waves 68
6.2.1 Kelvin Waves 69
6.2.2 Rossby Waves 71
6.3 The Eigenvalue Problem 71
6.4 Adjustment to a WWE in an Ocean GCM 75
6.4.1 Seasonal Variability 80
6.4.2 Sensitivity to Lateral Mixing 81
6.5 Propagation Through a Sloping Thermocline 84
6.6 Projection of a WWE onto modes 89
6.7 Summary 94

7 Kelvin Wave Adjustment Case Studies **96**
7.1 Introduction 96
7.2 Ocean Analysis Data 97
7.3 The Modal Structure of the Kelvin Wave 99
7.4 Projection of a WWE onto Modes 101
7.5 Summary 102

8 Conclusions **104**
8.1 The Main Results 105
8.2 Limitations 107
8.3 Future Work 108
8.4 Summary 109

List of Figures

1.1 Zonal wind stress anomaly and SST anomaly along the Equator from January 1997 to December 1998 (TAO Project webpage: www.pmel.noaa.gov/tao). 2

2.1 The distribution of chlorophyll in the eastern Pacific from a composite derived from SeaWiFS data over the period 18-25 June 2003. Red values show high levels of chlorophyll (courtesy of Prof. K. Richards). 5

3.1 Equatorial SST (°C) at 40° and 80° longitude during the 10 year spin up period for the standard configuration (iso 2yr). 18

3.2 Equatorial depth of the 20°C isotherm (m) at 40° and 80° longitude during the 10 year spin up period for the standard configuration (iso 2yr). 19

3.3 Spatial distribution of the Westerly Wind Event Perturbation, with a maximum amplitude at the centre of 0.3Pascal. 20

3.4 Variability of the depth of the 20°C isotherm at 80° longitude on the Equator over one year. (iso 2yr). 21

4.1 Annual mean vertical temperature section along the Equator (colour) and zonal velocity (contour) for the standard configuration (iso 2yr). 24

4.2 Along-Equator vertical annual mean temperature distribution. (iso 2yr, f2, f4). 25

4.3 Annual mean zonal velocity vertical section at 80° longitude for high, standard and low viscosity (iso high, 2yr, low). 26

4.4 Annual mean zonal velocity vertical section at 80° longitude for the different wind stress regimes (iso 2yr, f2, f4). 27

4.5 Meridional section at 80° longitude of mean Kinetic Energy (black) and eddy Kinetic Energy (red), in Jm^3, over the top 300m for the high, standard and low isopycnal mixing configurations (iso high, 2yr, low). 30

4.6 Meridional section at 80° longitude of mean Kinetic energy (black) and eddy Kinetic energy (red), in Jm^3, over the top 600m for different background wind stress configurations (iso 2yr, f2, f4). 31

4.7 Mean Meridional Heat Transport calculated between 60° and 100°long and eddy Meridional Heat Transport at 80°long in the top 200m for different levels of isopycnal mixing (iso high, 2yr, low). 33

4.8 Mean Meridional Heat Transport calculated between 60° and 100°long and eddy Meridional Heat Transport at 80°long in the top 200m for the different background wind stress regimes (iso 2yr, f2, f4). 34

5.1 AVHRR composites of SST in November and December 1999 showing the westward propagation of the cusp-like features associated with TIWs visible in the region of the strong SST gradient delimiting the extent of the Cold Tongue (courtesy of Prof. K. Richards). 37

5.2 SST for 1st August (iso 2yr low). 40

5.3 SST for 1st August (iso 2yr f2 f4). 41

5.4 Surface meridional velocity (ms^{-1}) timeseries at 2°N, the Equator, and 2°S at 80°long for model years 11 (red) and 12 (blue) (iso 2yr). 42

5.5 v-velocity (ms^{-1}) timeseries at locations on the Equator, with corresponding spectral amplitude (iso 2yr). 43

5.6 Equatorial meridional velocity (ms^{-1}) timeseries for year 11 below 200m at 80° longitude(iso 2yr). 44

5.7 Surface meridional velocity (ms^{-1}) 2°N during year 11 and timeseries taken at 80° longitude - mixing sensitivity (iso 2yr low). 45

5.8 Daily meridional velocity (ms^{-1}) along 80°long, averaged over the top 17 levels (iso 2yr low). . 46

5.9 Surface meridional velocity (ms^{-1}) 2°N during year 11 and timeseries taken at 80° longitude - wind stress sensitivity (iso 2yr f2 f4). 47

5.10 Wavelet analysis of equatorial meridional velocity year 11 timeseries taken at 80° longitude for the standard and low viscosity regimes. The top panels show the velocity timeseries, the second the wavelet spectrum, and the bottom the variance of the 12-64 day scale-averaged timeseries. (iso 2yr low). 50

5.11 Wavelet analysis of equatorial meridional velocity year 11 timeseries taken at 80° longitude for different wind stress regimes. The top panels show the velocity timeseries, the second the wavelet spectrum, and the bottom the variance of the 12-64 day scale-averaged timeseries. (iso 2yr f2 f4). 51

5.12 Snapshots of SST anomalies generated by a Kelvin wave propagating away from a WWE (s1c 2yr). 53

5.13 Snapshots every six days of SST anomalies generated by a Kelvin wave propagating away from a WWE as in Figure 5.12, though focusing on the period from day 50 to 68 between 70° and 90° longitude showing the slow westward-propagating SST anomalies (s1c 2yr). 54

5.14 SST (°C) anomaly along the Equator for after a WWE generated in February, April, August, and November of year 11 of the standard configuration (iso 2yr). 56

5.15 SST (°C) anomaly along the Equator for after a WWE generated in February for different horizontal mixing regimes (iso high, 2yr, low). 57

5.16 Temporal section from 15°S to 15°N at 80° longitude starting from August, showing SST anomalies generated by a Kelvin wave propagating through different isopycnal mixing regimes (iso 2yr, low and high). 58

5.17 Temporal section from 15°S to 15°N at 80° longitude starting from August, showing surface zonal velocity anomalies generated by a Kelvin wave propagating through different isopycnal mixing regimes (iso 2yr, low and high). 59

5.18 Temporal section from 15°S to 15°N at 80° longitude starting from August, showing surface meridional velocity anomalies generated by a Kelvin wave propagating through different isopycnal mixing regimes (iso 2yr, low and high). 60

5.19 SST (°C) anomaly along the Equator for after a WWE generated in February where the background wind stress is successively doubled (iso 2yr, f2, f4). 62

5.20 Temporal section from 15°S to 15°N at 80° longitude starting from August, showing meridional velocity anomalies generated by a Kelvin wave propagating through different wind stress regimes (iso 2yr, f2 and f4). 63

6.1 Dispersion relation for equatorial waves, where red is the Kelvin wave, yellow the mixed Rossby-gravity wave, green the first two gravity wave modes and blue the first two Rossby wave modes. Units of frequency (σ) are $(2\beta c)^{\frac{1}{2}}$ and those of zonal wavenumber (k) are $(2\beta/c)^{\frac{1}{2}}$. 69

6.2 Vertical structure of the zonal velocity eigenvector at 80° longitude on the Equator day1 (s1c 2yr). 72

6.3 Annual mean squared Brunt-Väisälä frequency (s^{-1}) along the Equator over the upper 500m (s1c 2yr). 73

6.4 Hovmöller of depth of the 20°C isotherm and SST along the Equator for a WWE generated in February (s1c 2yr). 75

6.5 Projection of the zonal velocity anomaly onto the modal coefficient (ms^{-1}) for the first four baroclinic modes along the Equator for a February WWE (s1c 2yr). 77

6.6 Modal analysis of zonal velocity anomaly and the zonal velocity anomaly field of a vertical section over the top 500m at 80° longitude on the Equator for a WWE generated in February (iso 2yr). The coefficient (ucoeff) is in units of ms^{-2} and the zonal velocity contour interval is $0.05ms^{-1}$. 79

6.7 Modal analysis of zonal velocity anomaly and the zonal velocity anomaly field of a vertical section over the top 500m at 80° longitude on the Equator for a WWE generated in February, April, August and November (iso 2yr). The coefficient (ucoeff) is in units of ms^{-2} and the zonal velocity contour interval is $0.05ms^{-1}$. 80

6.8 Modal analysis of zonal velocity anomaly along the Equator for a WWE generated in February (iso high 2yr low). The coefficient (ucoeff) is in units of ms^{-2}. 82

6.9 Modal analysis of zonal velocity anomaly at 80° longitude on the Equator for a WWE generated in February under different horizontal viscosity conditions (iso high, 2yr, low). The coefficient (ucoeff) is in units of ms^{-2} and the zonal velocity contour interval is $0.05ms^{-1}$. 83

6.10 Projection of the zonal velocity anomaly onto the modal coefficient (ms^{-2}) along the Equator for a WWE generated in February where the backround wind stress is successively doubled (iso 2yr, f2, f4). 85

6.11 Modal analysis of zonal velocity anomaly at 80° longitude on the Equator for a WWE generated in February where the backround wind stress is successively doubled (iso 2yr, f2, f4). The contour interval is 0.05ms^{-1}. 87

6.12 The temporal evolution of the modal projection coefficient $\tilde{X}_m$ (ms^{-2}) of modes 1 to 4 for a February WWE at the Equator, 30° longitude for the high, standard and low viscosity configurations(s1c high, 2yr, low). 90

6.13 The temproal evolution of the modal projection coefficient $\tilde{X}_m$ (ms^{-2}) of modes 1 to 4 for a February WWE at the Equator, 30° longitude for the standard, f2 and f4 wind stress configurations(s1c 2yr, f2, f4). 91

6.14 The Brunt-Väisälä frequency (s^{-1}) on day 5 of a February WWE at the Equator, 30° longitude for (a) the high, standard and low viscosity configurations (s1c high, 2yr, low) and (b) for the different background wind stress conditions (s1c 2yr, f2, f4). 93

7.1 Zonal wind stress anomaly and depth of the 20°C isotherm depth anomaly along the Pacific Equator from the 1st February 1997 to the 30th April 1997 (TAO Project webpage: www.pmel.noaa.gov/tao). 97

7.2 Zonal wind stress anomaly and depth of the 20°C isotherm depth anomaly along the Pacific Equator from the 1st November 2002 to the 31st January 2003 (TAO Project webpage: www.pmel.noaa.gov/tao). 98

7.3 Modal decomposition of zonal velocity anomaly into the first two baroclinic modes along the Pacific Equator for the March 1997 WWE and the December 2002 WWE. The coefficient (ucoeff) is in units of ms^{-1}. 100

7.4 Modal decomposition of zonal velocity anomaly into the first two baroclinic modes and vertical profile of zonal velocity anomaly over the top 500m at 80° longitude (relative to the longitude axis of Figure 7.3), at the Equator for the March 1997 WWE (left hand panels) and the December 2002 WWE (right hand panels). The coefficient (ucoeff) is in units of ms^{-1} and zonal velocity is in ms^{-1}. 101

7.5 Modal projection of an idealised WWE onto the ocean baroclinic modes representing the March 1997 WWE and the December 2002 WWE. The coefficient (ucoeff) is in units of ms^{-1}. . . . 102

List of Tables

3.1 Control run name identification table. 21

3.2 WWE experiment name identification table. Dates are all for year 11. 21

6.1 Amplitude of the first and second baroclinic modal coefficient (10^{-2}ms^{-1}) for a WWE generated in February, April, August and November (iso 2yr). 81

6.2 Amplitude of the first and second baroclinic modal coefficient (ms^{-1}) under different horizontal viscosity conditions (iso high 2yr low). 83

6.3 Amplitude of the first and second baroclinic modal coefficient (ms^{-1}) under different background wind stress conditions (iso 2yr f2 f4). 88

6.4 Projection coefficient maximum amplitude (10^{-5}ms^{-2}) for the gravest four baroclinic modes forced by a February WWE under different horizontal viscosity conditions (s1c high, 2yr, low). . 92

6.5 Projection coefficient maximum amplitude (10^{-5}ms^{-2}) for the gravest four baroclinic modes forced by a February WWE under different background wind stress conditions (s1c 2yr, f2, f4). 92

Chapter 1

Introduction

1.1 Motivations

The processes occurring in the Equatorial Pacific region are important both intrinsically and from the global perspective in terms of climate dynamics, as well as for socio-economic considerations, such that it is necessary to reproduce realistically the dynamics of this region in climate forecasting models. Some of the limitations of current forecasting efforts are related to the difficulties in capturing all the physical processes involved, including intraseasonal variability and resolving the high frequency component of the wind field. Deterministic mechanisms associated with modes of ocean-atmosphere variability are sought in order to improve the predictability of the changing state of the Equatorial Pacific system. Many models forecasting the growth of the 1997-98 El Niño event, shown in Figure 1.1, underestimated the maximum growth phase and the poor representation of the high frequency westerly wind anomalies that occurred in this period could have been part of this problem.

A key question is on the role of intraseasonal atmospheric variability in the El Niño Southern Oscillation (ENSO) Pacific system and its interaction with the Equatorial upper ocean. It is unclear whether high frequency, pulse-like Westerly Wind Events (WWEs) or the overall mean intraseasonal wind variability are the most important in terms of the oceanic adjustment. While the integral of the wind stress may be the same, the frequency is different. Models with observed mean wind variability that lack high frequency wind variability are still capable of simulating the observed ENSO events. An ENSO cycle can be generated with the mean seasonal zonal wind field, in the absence of high frequency zonal wind variability (van Oldenborgh, *pers.comm.*, 2003). Studies looking at the performance of general circulation models (GCMs) in forecasting recent ENSO events have concluded that one of the limitations of these models is the difficulty in capturing intraseasonal atmospheric variability in the Western Pacific (Slingo et al., 1996; Landsea and Knaff, 2000). It

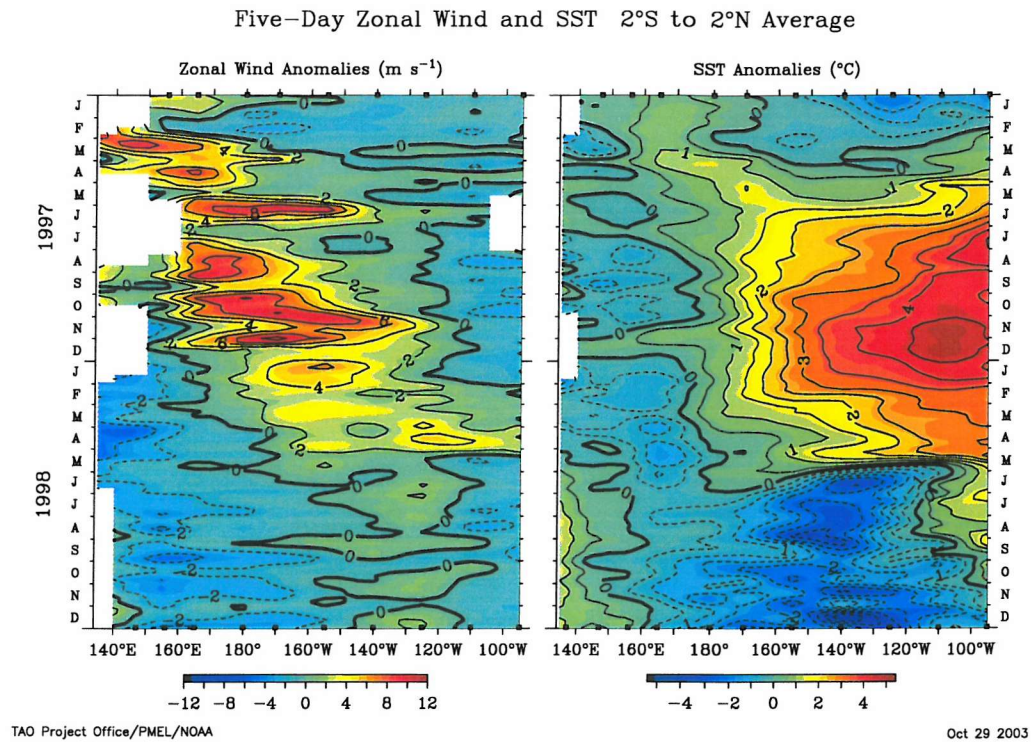

Figure 1.1: Zonal wind stress anomaly and SST anomaly along the Equator from January 1997 to December 1998 (TAO Project webpage: www.pmel.noaa.gov/tao).

is believed that ENSO is an oscillating system, as proposed by Suarez and Schopf (1988), but that its intensity is modulated by WWEs acting as random disturbances (Fedorov et al., 2002). Recent work has shown that the inclusion of WWEs in a coupled forecasting model improved the forecast of the 1997-98 El Niño event (Vitart et al., 2003).

The ocean response depends on whether its dynamics are linear, in which case the mean wind field is more important, or non-linear, where individual wind events may have a greater impact, though the linearity of the system will not be specifically addressed here. The response to an individual wind event perturbation will be studied, without considering the response to mean intraseasonal variability. Rectification of the ocean mean state occurs through non-linearity in the response, for example resulting from the wind-forced displacement of the Warm Pool and the propagation of WWE-forced Kelvin waves along a sloping thermocline. The ocean response will depend on the mean state, including its seasonality and the ENSO cycle. WWEs occur over a continuously changing ocean state, as Figure 1.1 shows. The sensitivity of the model ocean is also model dependent as mean states will differ, for example in the structure and extent of the Cold Tongue and the Warm Pool.

The interaction of certain WWEs with the mean state can be rectified by dynamical non-linearities, for example through Kelvin wave adjustment (Lengaigne et al., 2002). Locally, the WWE forced the eastward displacement of the Warm Pool edge, leading to a positive atmospheric feedback by shifting convection eastwards and continued the growth of zonal wind anomalies. Zhang and Gottschalck (2002) deterived an index of Kelvin waves forced by the intraseasonal Madden-Julian Oscillation (MJO) and so related ENSO warm events to increases in MJO activity that lead the warm events by 6-12 months. Understanding these scale interactions are not only important in terms of understanding the dynamics of the region, but also for determining the predictability of the system.

1.2 Objectives and Approaches

- To study the upper ocean response to a WWE, considering the importance of interactions between different modes of variability of different temporal and spatial scales on the evolution of the Equatorial Pacific Ocean mean state.
- To determine the effect of different ocean conditions on the adjustment to a WWE.
- To determine the sensitivity of the Equatorial Ocean and its adjustment to model configuration, considering lateral mixing.

A simplified process study framework enables, to some degree, the isolation of processes to try to facilitate the understanding of the complex Equatorial Pacific system. A general circulation model (GCM) is configured to simulate an Equatorial ocean basin and idealised wind perturbations are applied. The Kelvin wave adjustment is studied in detail, considering its sensitivity to the changing background ocean conditions, mainly in terms of the strength of the Equatorial circulation, the along-Equator thermal structure, and the level of activity of the Tropical Instability Wave (TIW) field.

The Equatorial Pacific system climatology is described in Chapter 2 together with its modes of variability and the occurrence of Westerly Wind Events. The ocean general circulation model, the configurations and experiments are presented in Chapter 3 and the simulated ocean states are described in Chapter 4. The background Tropical Instability Wave field and interactions with the wind-forced Kelvin wave are described in Chapter 5. The Kelvin wave adjustment is studied in more detail in Chapter 7. Two observed WWE and their ocean response are studied in Chapter 8 and a discussion of the main conclusions is presented in Chapter 9.

Chapter 2

The Equatorial Pacific Region

2.1 Climatology

The Equatorial Pacific Ocean is characterised by zonal asymmetry in its distribution of temperature and salinity. Sea surface temperature (SST) in the Western Pacific is the highest of the world oceans, reaching values of over 29°C. In the Eastern Pacific, the SST is cooler with values falling to around 24°C at certain times of the year. This strong temperature gradient is associated with the underlying thermocline that shoals eastwards. The along-equatorial density gradient drives the eastward flowing Equatorial Undercurrent (EUC) and the westward South Equatorial current (SEC) branches. At the Equator, the meridional flow has a divergence in the surface layers and a subsurface convergence. Warm water is thus transported polewards and cool water returns equatorwards, mainly in the region of the thermocline (Philander and Pacanowski, 1980).

Upwelling occurs in the Eastern Equatorial Pacific within and above the EUC, maintaining the cooler SSTs of the Cold Tongue that otherwise would be comparable to those in the Western Pacific (Xie, 1998). The easterly Trade winds lead to divergence in the surface layers due to poleward Ekman transport. This is compensated by a subsurface meridional convergence cell driven by the zonal pressure gradient. The zonal pycnocline rises from west to east to maintain the conservation of potential vorticity and flow in the EUC is along isopycnals. Bryden and Brady (1985) calculated a maximum upwelling velocity of $3\text{x}10^{-5}\text{ms}^{-1}$, with subsequent studies estimating similar values (for example, Weisberg and Qiao (2000)). The upwelling of nutrient rich water leads to high primary production, with a maximum in chlorophyll pigments that is clearly visible in the satellite image of Figure 2.1. Interestingly, the dynamics and thermodynamics of the upwelling region is modulated by the high phytoplankton concentration that contributes to the thermal heating of the mixed layer (Nakamoto et al., 2001).

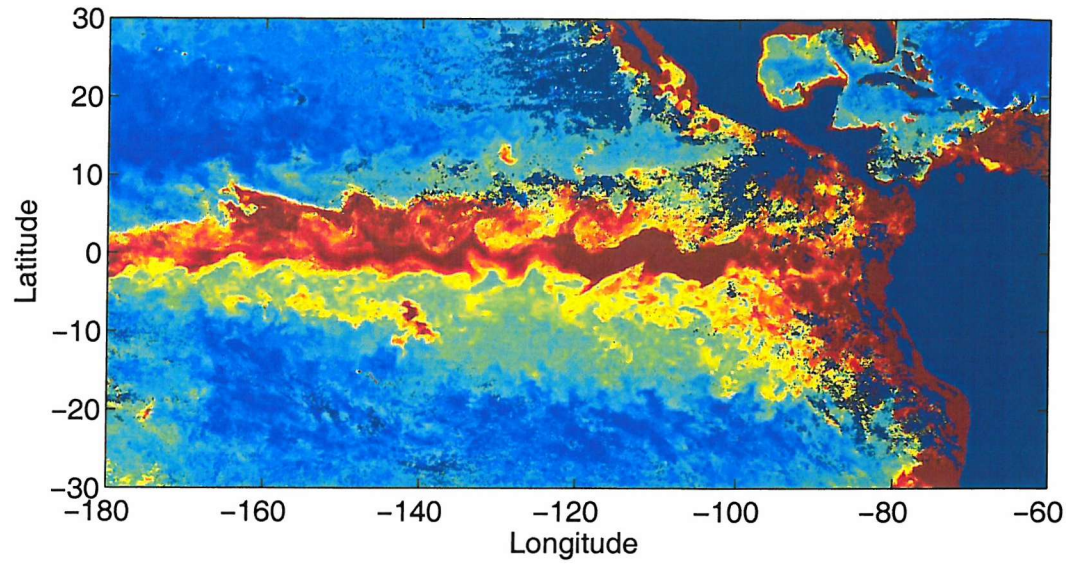

Figure 2.1: The distribution of chlorophyll in the eastern Pacific from a composite derived from SeaWiFS data over the period 18-25 June 2003. Red values show high levels of chlorophyll (courtesy of Prof. K. Richards).

The zonal SST gradient signal is coupled to the surface air temperature and the pressure gradient drives the easterly Trade winds. These form the lower part of the atmospheric Walker circulation cell over the Pacific, with its ascending branch in the Western Pacific and the sinking branch in the Eastern Pacific. The cold water tongue and upwelling of the Eastern Pacific are not maintained only by the Trades, as they are constrained by the Andes, but are also forced by the southerly winds that are drawn north over the Equator by the Inter-Tropical Convergence Zone, which is permanently located in the Northern Hemisphere of the Pacific (Xie, 1998).

The ocean and atmosphere systems are inextricably linked, as discussed by Bjerknes (1969), whereby both are the "cause and effect of each other". This coupling, known as the Bjerknes feedback, occurs during the seasonal changes in intensity of the wind field and oceanic circulation and is driven primarily by changes in insolation. In the Eastern Pacific, the Bjerknes feedback increases the initial cooling by the southerly winds by setting up the easterly Trades and spreading further westwards the extent of the cold tongue by the eastward flow of the EUC. The zonal SST temperature gradient that is generated by the Equatorial circulation in turn strengthens the Trade winds.

The climatological mean state of the Tropical Pacific differs between the Warm Pool in the west and the Cold Tongue in the east, not only in hydrography but also in terms of dynamics. The Warm Pool favours high frequency, intraseasonal coupled unstable modes, through mixed layer-wind interactions, entrainment and evaporative processes and cloud-radiation feedbacks. In contrast, equatorial wave dynamics play a much greater role in the Cold Tongue, favouring low frequency, coupled unstable modes (Wang and Xie, 1998). The Warm Pool mean conditions of a deep thermocline, high SST and weak horizontal temperature gradients act to buffer the sensitivity of the surface ocean and diminish the impact of ocean planetary wave dynamics.

Variability in the Tropical Pacific occurs at all temporal and spatial scales. A comprehensive, internationally coordinated scientific program was set up called the Tropical Ocean-Global Atmosphere (TOGA) Program that was carried out over a ten year period during 1985-1994 and focused on improving the observational monitoring of the Pacific basin with the Tropical Atmosphere-Ocean (TAO) moored buoy array and cruise programs. The program also involved a substantial modelling effort that was coordinated with the observational work, leading to a substantial increase in the understanding of the coupled Equatorial Pacific region and the ENSO phenomenon, as summarised by the National Research Council (1996) and McPhaden et al. (1998).

2.2 Modes of Variability

There are different temporal and spatial scales of variability in the tropical Pacific region. Variations in solar forcing lead to a prominent seasonal cycle. The cumulative effect of seasonally-forced equatorial waves drives variations in equatorial zonal currents, thermal structure, and dynamic height. Associated to the seasonal cycle is the variability in the Tropical Instability Wave field in the central and eastern Equatorial Pacific Ocean. At intraseasonal timescales, the Madden-Julian Oscillation (MJO) is the primary mode of variability with periods of high convective activity in the tropical Indian and Western Pacific regions. Associated with the MJO are high frequency, localised surface Westerly Wind Events that occur in the Western and Central Pacific. The El Niño-Southern Oscillation (ENSO) is the dominant mode of variability of the Tropics at interannual timescales. ENSO is a coupled ocean-atmosphere phenomenon that gives rise to basin-scale changes in the sea surface temperature (SST) of the tropical Pacific Ocean and the circulation of the tropical atmosphere, as well as influencing the climate globally through teleconnections. Finding predictability in this complex coupled system depends on understanding and being able to model

the dynamics and scale interactions governing the variability of this region.

2.2.1 The El Niño Southern Oscillation

El Niño events occur with a quasi-cyclic period of about 3-7 years, with contrasting La Niña conditions generally developing in between. SST anomalies and atmospheric convection anomalies occur together with the Southern Oscillation equatorial changes in sea level pressure between the Eastern and Western Pacific. This variability is accompanied by large oceanic zonal volumetric changes whereby the sea level increases in the Eastern Pacific during El Niño events. During the 1992-93 El Niño, the sea level at the eastern boundary rose by 32cm (Kindle and Phoebus, 1995). Upper ocean zonal volume transports can change interannually on a basin scale by as much as $64 \pm 32 \times 10^6 \mathrm{m}^3\mathrm{s}^{-1}$ (Johnson et al., 2000). The zonal displacement of the Western Pacific Warm Pool during the ENSO cycle is widely documented (McPhaden and Picaut, 1990; Delcroix and Picaut, 1998; Picaut and Delcroix, 1995; McPhaden, 1999). During the development of an El Niño event, the Warm Pool migrates eastward as a result of reversals in zonal flow, particularly in the upper 100m of the water column.

McCreary (1983) first proposed a conceptual model of ENSO where the timescales and dynamics were related to the propagation and reflection of subtropical Rossby waves and equatorial Kelvin waves, before direct observations of Kelvin waves in the equatorial Pacific had ever been made. This theory was elaborated on as the delayed-action oscillator theory (Schopf and Suarez, 1988; Suarez and Schopf, 1988; Battisti, 1988; Battisti and Hirst, 1989), rejecting the role of off-equatorial Rossby waves and based solely on equatorial wave dynamics, with wave transit times playing a central role. The model assumes that the zonal equatorial structure of the ocean leads to the central Pacific being the region of strongest coupling for oceanic and atmospheric anomalies and that adjustment to anomalies in this region occurs through the excitation of ocean equatorial waves.

A series of theories have also described ENSO as an unstable coupled mode (Philander et al., 1984; Neelin, 1991; Pontaud and Thual, 1998). For example, the SST mode proposed by Neelin (1991) results when the equatorial wave speed is faster than advection timescales so that dynamic adjustment is fast relative to coupled effects. Subsequent modelling experiments have shown that these models and the delayed action oscillator may actually be two extremes of the same behaviour. These theories do not exist independently of each other, but co-exist with varying degrees of dominance that depend on the background conditions of the ocean (Latif et al.,

1993).

Recent work in understanding the mechanisms driving ENSO has addressed the role of wind variability in the Western Pacific in forcing Kelvin wave variability, instead of Rossby wave reflection. Studies have shown that ENSO may consist of a stable dynamical regime excited by stochastic forcing (Moore and Kleeman, 1999; Penland et al., 2000). A study of the energetics of the El Niño-La Niña cycle found evidence of delayed-action oscillator processes taking place whereby perturbations developed anomalies in the coupled system during the preceding El Niño or La Niña conditions (Goddard and Philander, 2000). These results showed that adjustment processes could be more important than perturbations caused by stochastic forcing, such as WWEs. However, a recent study of the relative role of reflected Rossby waves and wind variability in forcing Kelvin waves found that wind forcing accounted for around 90% of Kelvin wave variability in the Western Pacific (Boulanger et al., 2003).

2.2.2 The Madden-Julian Oscillation

The Madden-Julian Oscillation (MJO) is an eastward propagating atmospheric signal characterised by multiple covariance between zonal wind, surface air pressure and temperature throughout the troposphere that dominates the intraseasonal variability of the Tropics (Madden and Julian, 1971, 1972). It has a period of 40-60 days and consists of a low frequency atmospheric Kelvin/Rossby wave structure, which is a large circulatory cell that is vertically coherent throughout the troposphere due to its deep convective activity. Intraseasonal convective variability in the Indian and Western Pacific consists of an eastward propagating mode travelling at 3-5ms^{-1} that is coupled to anomalies in the wind field. The organised convective structures and associated anomalies disintegrate over the cooler surface water east of the Dateline.

The intensity of MJO activity is correlated to the seasonal cycle, with its convective signal more pronounced during the boreal winter and spring. During the first three months of the year convection is located over the Equator, when the warmest SSTs are approximately symmetrical across the Equator (Salby and Hendon, 1994). There is a strong correlation between MJO wind activity and seasonal Kelvin wave activity in the Western Pacific, in contrast to the weaker correlation found in the Eastern Pacific. Near-resonance conditions may occur between the forced Kelvin waves and the wind field west of the Dateline where the MJO winds translate at speeds of around 5ms^{-1}, which is comparable to the first baroclinic Kelvin mode phase speed, while east of the Dateline the MJO translation speeds increase to around 10ms^{-1} (Hendon et al., 1998).

The main theories proposed to explain the dynamics of the MJO treat the oscillation as an atmospheric phenomenon assuming fixed SSTs and do not consider an interactive ocean role in maintaining and modulating the MJO cycle. The onset of MJO convection occurs generally over the tropical Indian Ocean. There are numerous theories for the generation of convection. Internal wave CISK (conditional instability of the second kind) theory (Chang, 1977; Lau and Peng, 1987) proposes that eastward propagating unstable modes are maintained by low level moisture convergence that leads to deep cumulus convection and condensation that releases latent heat, and so forcing further convection. The evaporation-wind feedback theory (Neelin and Cook, 1987) proposes that convection forces low-level converging winds that can cause surface latent heat flux anomalies east of the original convection, increasing low-level moisture static energy and generating further convection.

Further developments in the theory have included combining wave CISK and evaporation-feedback mechanisms (Kirtman and Vernekar, 1993). More attention has been given to the role of SSTs and the upper ocean. The coherence of surface fluxes and SST with MJO activity in observations (Zhang, 1997; Woolnough and Slingo, 2000) has led to the MJO being considered a coupled phenomenon, particularly in modelling terms (Waliser et al., 1999; Gualdi et al., 2000; Hendon, 2000; Inness and Slingo, 2003). Modelling the MJO remains an ongoing problem for the scientific community. Though most models reproduce some sort of intraseasonal variability (Slingo et al., 1999), the observed amplitude, phase speed and propagation over the Maritime Continent and into the Western Pacific are not reproduced. Forecasting errors also increase if the forecasts are initiated during periods of high MJO activity (Hendon et al., 2000).

A simple mixed layer ocean may be sufficient to simulate the coupled processes of the MJO (Waliser et al., 1999; Shinoda and Hendon, 2001). Therefore improvements in its representation are not necessarily achieved by including a fully interactive ocean (Hendon, 2000; Inness and Slingo, 2003). This can be because the ocean GCM basic state is not an accurate representation of the region (Inness et al., 2003) and because the multiscale organised cloud convection dynamics of the MJO is modelled by the atmosphere GCM sub-grid scale cloud physics parameterisation scheme.

2.3 Intraseasonal Forcing and ENSO

Lau and Chan (1988) first postulated that there could be a link between MJO activity and ENSO variability when they found that 60% of anomalous convection during the 1982-83 El Niño event was related to the MJO. Modelling results have given an indication that ENSO affects the propagation of the MJO, with intraseasonal convection reaching the Central Pacific during El Niño, compared with La Niña conditions when convection tends to be located in the Indian and Western Pacific Oceans (Gualdi et al., 1999). However, the role of the MJO in modulating the evolution of ENSO is still not conclusively known as observational and modelling studies give rise to contradicting results.

Many coupled dynamical models manage to simulate an ENSO cycle without having a realistic simulation of atmospheric intraseasonal variability and the MJO occurs in years that have low ENSO activity (Kessler and Kleeman, 2000). Studies looking at indices of MJO activity and ENSO have generally failed to find significant correlation (Slingo et al., 1999; Hendon, 2000). Indices are typically generated by a decomposition into EOF (empirical orthogonal function) components that will locate MJO variability predominantly over the Indian Ocean, where there is less scope for interaction with ENSO. Kessler (2001) found that while the first two MJO EOF modes are uncorrelated with ENSO, the third mode, which represents an east-west meandering into the Western Pacific, is associated with ENSO.

Recent developments in understanding the interaction of the MJO with the surface ocean are suggestive that the MJO interacts with the ENSO cycle. The MJO is associated with SST variability of 1.0°C in the Warm Pool, more than that due to annual and interannual variability (Lau and Sui, 1997). The 1997 wintertime MJO activity led to initial SST anomalies that caused convective activity to migrate eastwards, increasing the SST warming in the central Pacific (Hendon, 2000; Bergman et al., 2001). Kessler and Kleeman (2000) performed a hindcast of the 1997/98 El Niño with an intermediate coupled model where the rectified SST pattern produced by a MJO perturbation was applied. This led to a 50% increase in the strength of eastern equatorial Pacific SST anomalies. While the MJO is not necessarily leading the development of El Niño events, once warm anomalies develop in the Central Pacific, the MJO can migrate further east and influence the development of the event (Kessler, 2001).

A direct mechanism by which the MJO may interact with ENSO is through the forcing of intraseasonal Kelvin waves (Hendon et al., 1998; Zhang and Gottschalck, 2002). ENSO conditions will in turn affect the propagation of intraseasonal Kelvin waves by modulating the mean state. Kelvin waves propagate faster during the El Niño phase than during La Niña conditions (Benestad et al., 2002). The relative role in climate of the total intraseasonal variability generated by the MJO, or of specific events related to individual zonal wind anomalies, known as Westerly Wind Events (WWEs), remains to be elucidated. The following section will describe WWEs, as the focus of this study is the oceanic response to these perturbations.

2.4 Westerly Wind Events

High frequency westerly winds are associated with the active phase of the MJO in the western Pacific due to the occurrence of enhanced low-level convergence (Lau and Chan, 1988; Nakazawa, 1988; Slingo et al., 1999). They can also result from individual and paired tropical cyclones (Keen, 1982) and mid-latitude cold surges from the Asian continent (Harrison, 1984). Westerly Wind Events (WWEs) cause a deceleration of the easterly Trades and can lead to a complete reversal to westerly surface flow. WWEs mainly occur during the boreal winter and spring and last from 2 days to a couple of weeks (Harrison and Giese, 1991), reaching speeds from about $2ms^{-1}$ to $10ms^{-1}$ (Delcroix et al., 1993). They have a large zonal extent of the order of 1000km, while having a meridional extent of only a few hundred km. There appears to be a greater level of WWE activity preceding and during El Niño events than during La Niña periods.

Composites for different types of WWEs according to the latitudinal location of the maximum zonal wind have been constructed from daily averaged wind vector fields of Pacific island network records since 1955 (Harrison and Giese, 1991; Harrison and Vecchi, 1997). The strongest and most frequent events are those located over or south of the Equator. These have the greatest impact on the equatorial wave guide. The events last from a few days to a couple of weeks. In addition to these events, multi-regional or mega-WWEs are also identified covering areas larger than the delimited composite regions.

These wind anomalies generate an adjustment through equatorial waves that has the capability of rapidly transmitting the local response across the whole Pacific basin within timescales of a few months. Locally, WWEs lead to changes in the current structure above the thermocline including current reversals and associated horizontal pressure gradient reversals (Cronin et al., 2000). The first observational study documenting the oceanic response to a WWE was carried out by Hisard et al. (1970) during a cruise at 170°E in April 1967. Westerly and north-westerly winds prevailed for eight days. An eastward surface current was observed, together with subsurface westward flow. During a WWE in May 1986, the mixed layer response was rapid, with a Yoshida Jet (Yoshida, 1959) developing within the first three days after the start of the WWE (McPhaden et al., 1988). Approximately 8-11 days after the peak in wind forcing, subsurface pressure gradients set up by the surface flow typically lead to the evolution of a subsurface westward jet (Delcroix et al., 1993; Smyth et al., 1996; Richardson et al., 1999; Cronin et al., 2000).

Numerous studies have looked at the role of WWE occurring in the Western and Central Pacific in forcing the Eastern Equatorial Pacific (Harrison, 1989; Giese and Harrison, 1991; Kindle and Phoebus, 1995). An early modelling study that looked at the effects of the wind stress field in the Western Pacific on the equatorial wave guide showed that local and remote forcing are both almost equally important in the Eastern Pacific (Harrison, 1989). During the sea level rise of the 1991-92 El Niño, three peaks occurred in the gauge data of the Galapagos, Peru and Ecuador. Modelling results for the same period also resolved these pulses and they were found to be wave packets forced by three WWEs in the Central Pacific (Kindle and Phoebus, 1995). Intraseasonal westerly wind anomalies were important for the development of the 1986-87 and 1991-92 El Niño events (Matsuura and Iizuka, 2000).

The 1997/98 El Niño event, shown in Figure 1.1, was in some respects the strongest ever recorded and its evolution, in concurrence with high levels of intraseasonal activity has been widely studied, particularly since most forecasting attempts failed to capture its particularly intense growth rate (Barnston et al., 1999). In March-April 1997 a WWE generated a downwelling Kelvin wave that led to a warming of the central Pacific, after which the pre-wave zonal current, surface wind and SST gradient were not restored (Bergman et al., 2001). Numerous other studies have shown that the Kelvin wave adjustment to this WWE was important in the evolution of the subsequent El Niño event (Balmaseda et al., 2002; Lengaigne et al., 2002, 2003; Belamari et al., 2003).

2.5 Summary

The Equatorial Pacific region is modulated by the seasonal cycle, and intraseasonal and interannual modes of variability. As Zhang and Gottschalck (2002) have highlighted, a key question that remains to be definitively answered is whether intraseasonal variability in the Tropics is distinct from white noise in the coupled Equatorial Pacific system and whether WWEs provide stochastic forcing that impacts the evolution of ENSO. The work in this study will continue to develop the understanding of the impact of WWEs on the Equatorial ocean by modelling the Kelvin wave adjustment to WWEs. Not all WWEs lead to a strong ocean response. The response depends on the geographical location of the WWE, its intensity, duration and fetch, but less attention has been given in past studies to the role of the backgound ocean state. This includes the shoaling of the thermocline, vertical stratification, the Equatorial current system, and the Tropical Instability Wave field.

This project will study the structure of a WWE-forced Kelvin wave and how the adjustment process is sensitive to and modulated by the background ocean state. Recent work has looked at the ocean adjustment to WWEs in realistic ocean-only or coupled simulations. This study will be based on an idealised equatorial ocean where the sensitivity to the background state is investigated through a series of process studies using different mixing and background wind stress configurations. Though the configurations are not directly comparable to the Equatorial Pacific, the controlled changes in configuration and associated changes in the WWE-forced adjustment facilitate the isolation of processes and their behaviour. Finally, the results will be analysed in a realistic context and the response to two observed WWEs will be studied.

Chapter 3

Overview of Model and Experiments

3.1 Introduction

The tropical Pacific region is a coupled ocean-atmosphere system with a high level of complexity and interactions occurring at all scales, both temporal and spatial. To simplify the problem and isolate certain aspects of this system, process studies are carried out in an idealised ocean-only equatorial basin configuration using an ocean General Circulation Model (OGCM). A series of experiments involving high frequency wind perturbations representing Westerly Wind Events (WWEs) are performed under different background ocean configurations to study the oceanic adjustment process and its sensitivity to the ocean state.

3.2 The OPA OGCM

Version 8.1 of the Océan Parallélisé (OPA) ocean primitive equation general circulation model (GCM) (Madec et al., 1998) is used. It solves the Navier-Stokes equations with the momentum and continuity equations and with equations for the conservation of salt and heat and the nonlinear Jackett and McDougall (1995) equation of state, which calculates density using potential temperature. The hydrostatic approximation is made and the equations are solved on an Arakawa C grid (Bryan and Cox, 1987). The fluid is assumed to be incompressible so that the divergence of velocity is zero. The model was developed at the Laboratoire Dynamique et de Climatologie (LODYC), Paris. In this study the model is used in a z-coordinate system where the levels are geopotential surfaces. Topography would be resolved as a series of steps between levels, but here we use a flat-bottomed ocean.

The model is configured to an idealised equatorial ocean domain from 30°N to 30°S and 120° in longitude, with a resolution of 0.5x0.5°. The choice of resolution is based on earlier sensitivity tests carried out to determine the best resolution to model the equatorial circulation that was also the most efficient in terms of computing cost. The model is 5000m deep and there are 31 levels in the vertical with enhanced resolution in the top layers. A timestep of 1 hour is selected in order to meet the necessary numerical stability criterion, in relation to the grid resolution.

The model can be configured to allow the lateral diffusion and viscosity tensors to be directed along level or isopycnic surfaces. The level mixing orientation mixes properties along geopotential surfaces while the isopycnal orientation mixes along isopycnal surfaces. Observations have shown that mesoscale turbulence leads to mixing along isopycnal surfaces, rather than across them. Though experiments with level mixing have been carried out, only experiments with isopycnal mixing are presented here. Horizontal mixing is restored to 10^3 m^2s^{-1} at the northern and southern boundaries, creating a sponge layer to damp instabilities and to resolve the boundary layer. This method, which is also used by Maes et al. (1997), enables the use of lower levels of mixing in the equatorial region. A no-slip condition is applied to the bottom and lateral boundaries.

3.3 The Role of Horizontal Mixing

Processes that occur at sub-grid scales, such as turbulent mixing, need to be quantified through use of non-dynamical parameterisations as they cannot be resolved explicitly by the numerical scheme. Numerical stability in GCM simulations is generally achieved through the choice of grid spacing, timestep and level of hmethods.texorizontal mixing, without direct consideration of sub-grid scale processes and their role in determining momentum and tracer fluxes. Numerous studies have shown that in the Equatorial Pacific region, both the mean circulation and the transients are sensitive to the specification of lateral mixing (Maes et al., 1997; Guilyardi et al., 2001; Pezzi and Richards, 2003). Stockdale et al. (1993) found that horizontal viscosity is an important indicator of model performance, more so than horizontal resolution. The level of horizontal viscosity and diffusivity influences the dynamics and thermodynamics of the the Equatorial ocean (Maes et al., 1997), and, through the sensitivity of SST, also of the coupled system (Guilyardi et al., 2001).

Lateral turbulence mixing is the result of mesoscale turbulence, which is resolved explicitly if the model is eddy-resolving, and submesoscale turbulence that must always be parameterised and is never solved explicitly. In a non-eddy resolving configuration of OPA, mesoscale eddy-induced turbulence is parameterised by the Gent and McWilliams (1990) scheme. Submesoscale turbulence leads to the cascade of energy toward the grid scale that is necessary to preserve numerical stability, while not being directly related to the explicitly resolved mesoscale turbulent processes. The OPA has four parameterisations of lateral mixing available. The configuration used here employs the isopycnal mixing scheme. Vertical turbulent mixing is assumed to depend linearly on the gradients of velocity, temperature and salinity. The vertical eddy viscosity and diffusivity coefficients amethods.texre computed here by a 1.5 turbulence closure scheme based on a prognostic equation for turbulent kinetic energy, which is generated by shear and destroyed by stratification (Gaspar et al., 1990).

Maes et al. (1997) carried out experiments with the OPA model studying the sensitivity of the Equatorial Pacific mean circulation to varying levels of lateral viscosity and diffusivity. Integrations with varying levels of lateral mixing (10^2, 10^3, and $10^4 m^2 s^{-1}$) over the 10°N to 10°S band were performed with the horizontal mixing terms orientated along le years with WWE perturbations applied at different times of yevel surfaces. The circulation is enhanced when low levels of lateral mixing are applied. This leads to stronger vertical shear, a source of turbulent kinetic energy (TKE), which increases vertical eddy diffusivity and viscosity. Lateral and vertical sub-grid scale mixing should not be treated separately due to this coupling of processes occurring on the vertical and lateral planes (Maes et al., 1997).

Recent studies have shown that lateral mixing oriented along isopycnal surfaces gives a better representation of tropical circulation in GCMs (Lengaigne et al., 2002; Pezzi and Richards, 2003). Diapycnal diffusion is reduced by using an isopycnal mixing scheme so that the pycnocline is tighter and the equatorial current system is accelerated. A sensitivity study using an isopycnic-coordinate model showed that the strength of the EUC was more dependant on the choice of viscosity regime, as well as on the choice of wind stress forcing, than horizontal resolution (Megann and New, 2001). Mixing sensitivity studies are carried out here as a continuation of the work described here to study further the sensitivity of the Equatorial circulation and its adjustment processes. The choice of lateral diffusivity and viscosity follow on from work by Maes et al. (1997), though all the experiments here use the isopycnal orientation. Particular attention is given to the sensitivity of the Tropical Instability Wave field to lateral mixing.

3.4 Process Study Experiments

The model is forced from rest by the Hellerman and Rosenstein (1983) monthly mean zonally-averaged wind climatology and is spun up for a ten year period. The model is only forced by the zonal component of the wind field as a simplification of the predominantly zonal surface wind circulation of the Trade winds in the Equatorial Pacific. The Hellerman and Rosenstein (1983) wind climatology is considered to be suitable for a process study of the equatorial region, despite this climatology having generally stronger values of wind stress in the Tropics than other climatologies (Josey et al., 2002). The surface wind stress provides an air-sea momentum flux that is the surface boundary condition of the vertical turbulent momentum fluxes. The spin up is initiated from temperature and salinity climatology fields (Levitus and Boyer, 1994) and the SST and SSS fields are restored to mean fields (Levitus and Boyer, 1994) with a monthly timescale, which is long enough not to significantly affect the background Tropical Instability Wave (TIW) field. A restoration timescale that is comparable to the 20-30 day TIW frequency would damp the TIW signal.

Experiments are carried out after a spin up of ten years with WWE perturbations applied at different times of year 11. The perturbation experiments are all carried forward to two years after the start of the WWE. Control runs are simultaneously run with the same configuration as each perturbation experiment, but without the WWE, against which the perturbation experiments can then be compared.

3.4.1 Spin Up Period

The initial spin up in the equatorial region takes less than two years due to the rapid adjustment by the equatorial wave guide, but the spin up is nonetheless extended to ten years to produce multiple years with a well defined seasonal cycle. Figure 3.1 shows the ten year timeseries of SST for the standard configuration at two locations on the Equator. After the first year of integration, the SST at 40° longitude, on the edge of the Warm Pool, fluctuates with a seasonal cycle between 25 and 26°C. At 80° longitude, in the Cold Tongue region, the SST adjusts to between 22 and 24°C. The seasonal fluctuation at the two locations is correlated, though there is more variability in the Cold Tongue than the Warm Pool due to the presence of Tropical Instability Waves (TIWs) and the shallow thermocline.

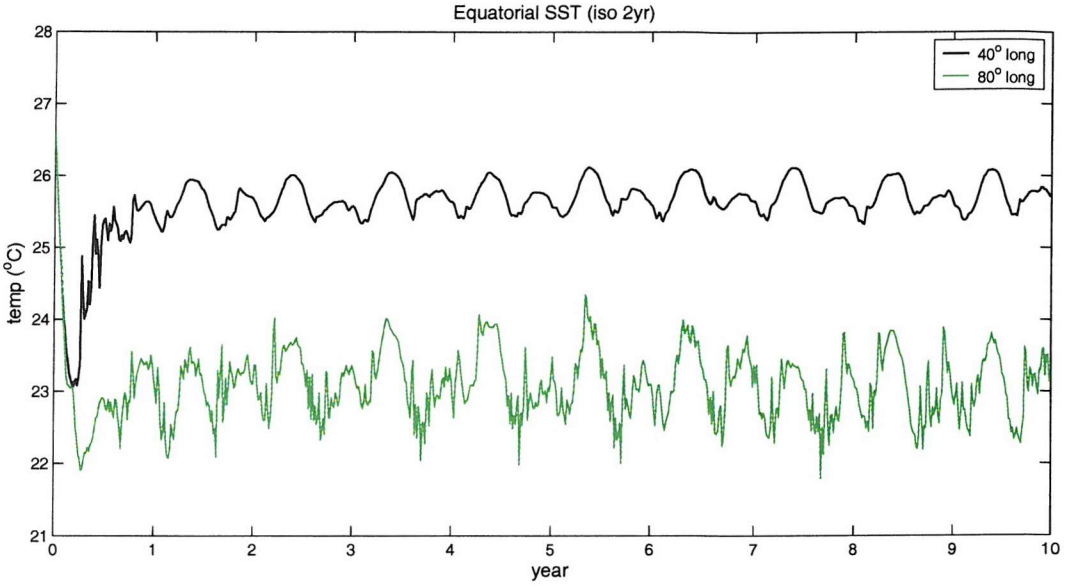

Figure 3.1: Equatorial SST (°C) at 40° and 80° longitude during the 10 year spin up period for the standard configuration (iso 2yr).

Figure 3.2 shows the ten year timeseries of the depth of the 20°C isotherm at the same locations as in Figure 3.1 at the Equator. The greatest variability occurs in the eastern basin at 80° longitude, following the seasonal variability in upwelling at the eastern boundary. The seasonal fluctuations are also present, though weaker at 40° longitude. These locations both show a rapid spin up during the first two years of integration. Both the surface temperature signals in Figure 3.1 and the deeper signal of the depth of the 20°C isotherm do not show any model drift due to the monthly restoration of the surface fields.

Both fields show some degree of interannual variability, despite the fixed forcing fields due to the non-linearities of the system such as the formation of Tropical Instability Waves. Though there are sponge layers at the poleward boundaries, propagating boundary signals may influence the Equatorial region of the domain. Reflection also occurs at the lateral boundaries. The model domain has been chosen to be extensive enough so that the Equatorial region that we are interested in is as isolated as possible from noise related to the boundary. Another source of additional noise could be the sub-tropical regions where any gyre circulation that may form will take longer to spin up to a steady state than the Equatorial circulation.

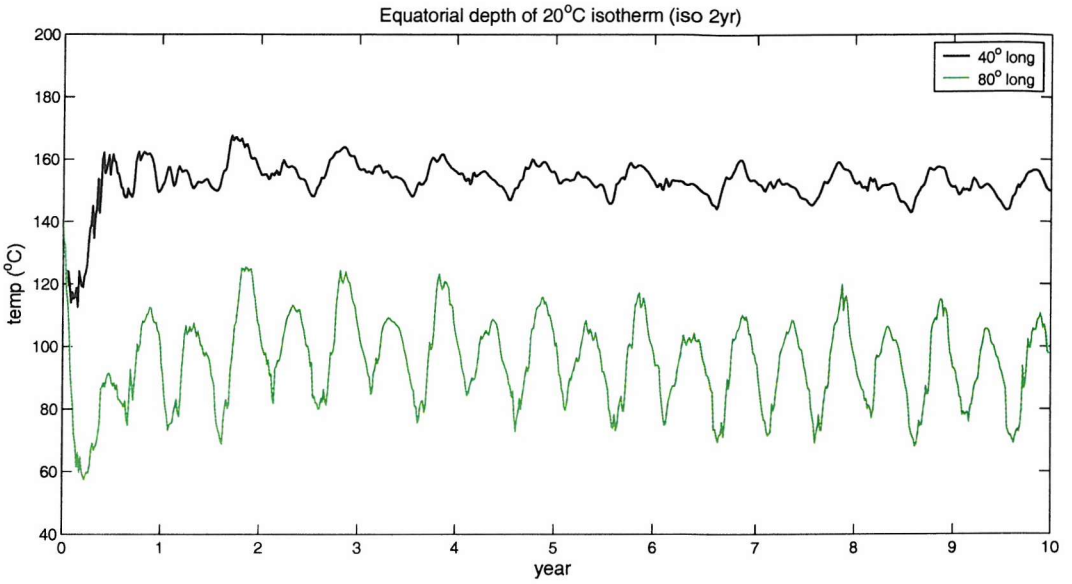

Figure 3.2: Equatorial depth of the 20°C isotherm (m) at 40° and 80° longitude during the 10 year spin up period for the standard configuration (iso 2yr).

3.4.2 The Westerly Wind Event

The system is perturbed by the initiation of an analytical westerly wind event (WWE). The WWE is applied to the u-points of the model for the u-component of the prescribed wind stress. It is Gaussian in distribution, with a zonal extent of 5° and a meridional extent of 3°, decaying exponentially away from the centre. The spatial distribution of the perturbation is derived from experiments carried out by Zhang (1995), where a layer ocean model of the Equatorial Pacific was forced by a WWE. The centre of the event is located at the equator and at 30° longitude and it has a maximum amplitude of 0.3 Pascal that develops as a half sinusoid over ten days. Figure 3.3 shows the location and spatial distribution of the WWE perturbation at its maximum amplitude. The location of the WWE is chosen so that it occurs in the western part of the basin. It is located sufficiently far from the western boundary so that eastward propagating signals reflected by the western boundary influence the least possible the Kelvin wave adjustment that will occur east of the WWE.

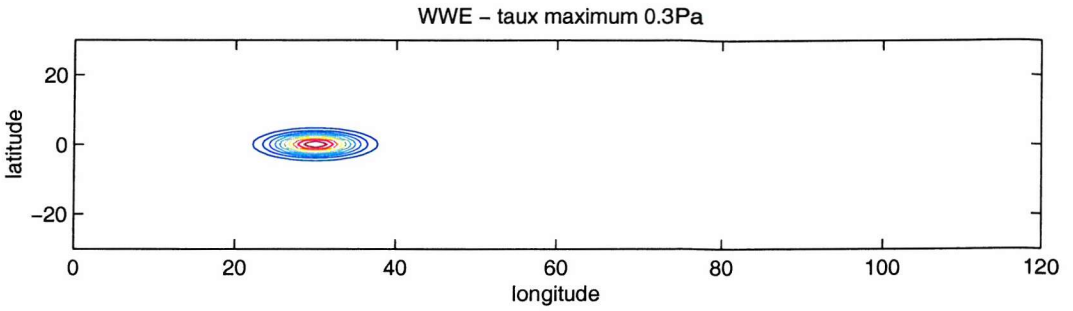

Figure 3.3: Spatial distribution of the Westerly Wind Event Perturbation, with a maximum amplitude at the centre of 0.3Pascal.

The WWE is stationary, though observed WWEs generally propagate eastwards. The perturbation is only applied to the wind stress field, with no associated heat flux anomaly associated to it. Though this is a simplification, it is in order to isolate the dynamic response from the thermodynamic response that would otherwise also occur.

3.4.3 Experiment Nomenclature

Details of the nomenclature for all control integrations are given in Table 3.1. The 'iso 2yr' configuration is referred to as the standard configuration for both the mixing sensitivity studies and the experiments where the background wind field is varied. Previous studies have shown that this resolution and level of horizontal mixing is suitable to model the Equatorial ocean (Maes et al., 1997; Pezzi and Richards, 2003). The nomenclature for the WWE experiments of the standard (iso 2yr) configuration are given in Table 3.2. The names of experiments based on the other configurations follow the same pattern, with the second part of the identification name denoting the configuration, such as 'slc high'.

The timings of the WWE are chosen following the annual variability of the depth of the 20°C isotherm. Figure 3.4 shows this variability at 80° longitude at the Equator. Two maxima in depth occur, one in boreal spring and the other in late autumn, and two minima, in early spring and in summer, due to the seasonal variability of the background wind field. The WWE are timed to initiate so that the Kelvin wave generated arrived at 80° longitude around the maximum and minimum peaks.

configuration	mixing tensor orientation (m^2s^{-1})	lateral viscosity	background wind stress
iso 2yr	isopycnal	10^3	Hellerman and Rosenstein (1983) (HR)
iso high	"	10^4	HR
iso low	"	10^2	HR
iso f2	"	10^3	HR x 2
iso f4	"	10^3	HR x 4

Table 3.1: Control run name identification table.

experiment	WWE start	WWE end
s1c 2yr	01 feb	10 feb
s2c 2yr	01 april	10 april
s3c 2yr	01 aug	10 aug
s4c 2yr	01 nov	10 nov

Table 3.2: WWE experiment name identification table. Dates are all for year 11.

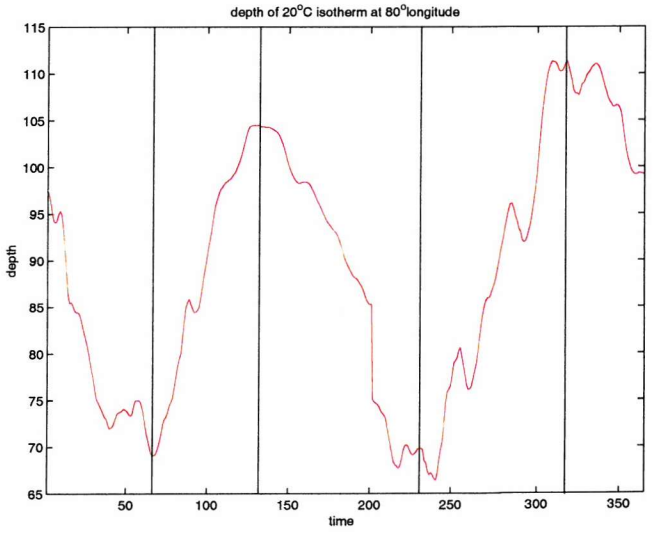

Figure 3.4: Variability of the depth of the 20°C isotherm at 80° longitude on the Equator over one year. (iso 2yr).

3.5 Summary

The OPA OCGM has been configured to test the sensitivity of the Equatorial ocean and its adjustment to a WWE perturbation to levels of lateral mixing and the strength of the background wind field. The model domain is a simplified representation of the Equatorial Pacific, though the zonal extent of the model is around 40° longitude shorter than in reality. There are some limitations with such an idealised approach, such as the poor resolution of the western boundary and subtropical gyres and the model ocean must be maintained by restoring to climatological fields. Such compromises are necessary to achieve a balance between computational cost, simplification of the system and having the capability to resolve the dominant processes of interest.

Chapter 4

The Model Equatorial Ocean

4.1 Introduction

The main features of the Equatorial Pacific are simulated by all the configurations in terms of temperature and zonal velocity distributions. A Cold Tongue develops in the eastern basin and a Warm Pool in the western basin. The circulation within 5° of the Equator is dominated by zonal flow with an eastward flowing Equatorial Undercurrent (EUC) and westward flowing north and south branches of the South Equatorial Countercurrent (SEC). The rest of this chapter will describe the standard configuration and comment on whether it can be compared to the observed Equatorial Pacific. The sensitivity of the model ocean to the level of horizontal mixing and the strength of the background wind field is addressed and the energetics and thermodynamics of the configurations are studied.

The annual mean temperature (colour) and velocity (contour) field of the top 500m along the Equator of the standard configuration (iso 2yr) is shown in Figure 4.1. There is an along-Equator sloping thermal structure with a well defined Warm Pool in the western basin. The upward tilting isotherms are indicative of upwelling in the eastern basin. This is matched by the zonal velocity section that captures the eastward and upward flowing EUC, with its maximum located within the thermocline. Increasing the lateral viscosity leads to a relaxation of the thermocline, a slight warming of the Warm Pool SSTs and a warming of the Cold Tongue SSTs as upwelling is reduced by a more diffuse thermocline. Reducing the viscosity leads to an increase in the annual variability in SST in the Cold Tongue.

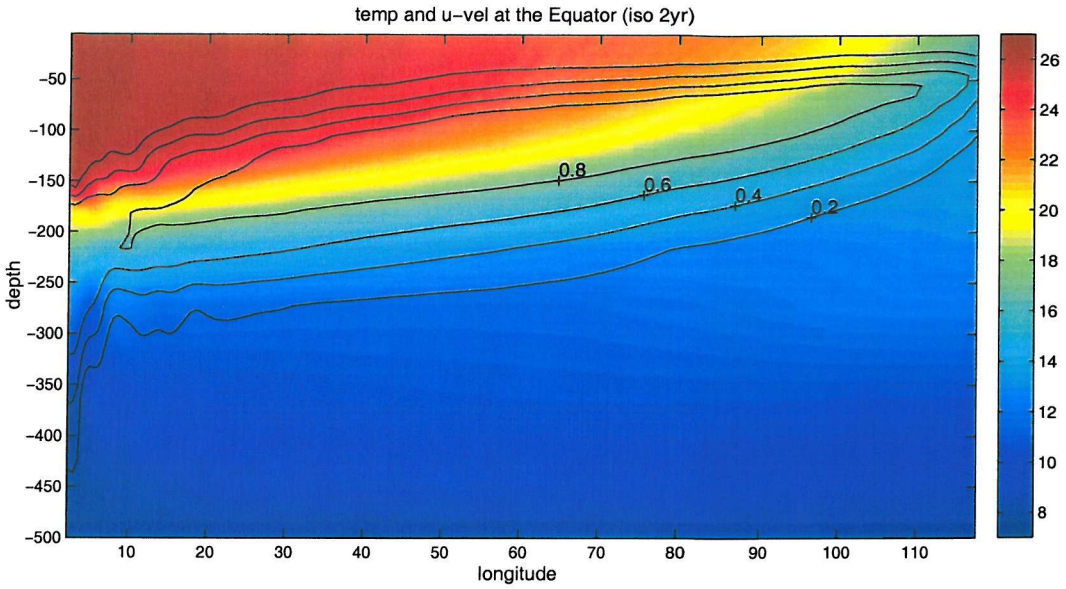

Figure 4.1: Annual mean vertical temperature section along the Equator (colour) and zonal velocity (contour) for the standard configuration (iso 2yr).

When the background wind field is gradually increased, the thermocline gradient increases in steepness, as shown in Figure 4.2. Upwelling increases in strength so that there is a linear 5°C reduction in the mean Cold Tongue minimum surface temperature with each increase in wind stress magnitude. The westward extent of the Cold Tongue also increases, as does the extent of the Tropical Instability Wave (TIW) field. The Warm Pool is effectively eroded away by the increase in mesoscale mixing that leads to a decrease of 1°C of the mean maximum Warm Pool surface temperature. A greater zonal extent of the domain is necessary for the f4 configuration in order to resolve the Warm Pool structure, though this would increase the computation time considerably. Though these thermocline structures are unrealistic in terms of the actual Equatorial Pacific Ocean, they provide a set of configurations with which one can study the propagation of a WWE-generated Kelvin wave through a sloping thermocline.

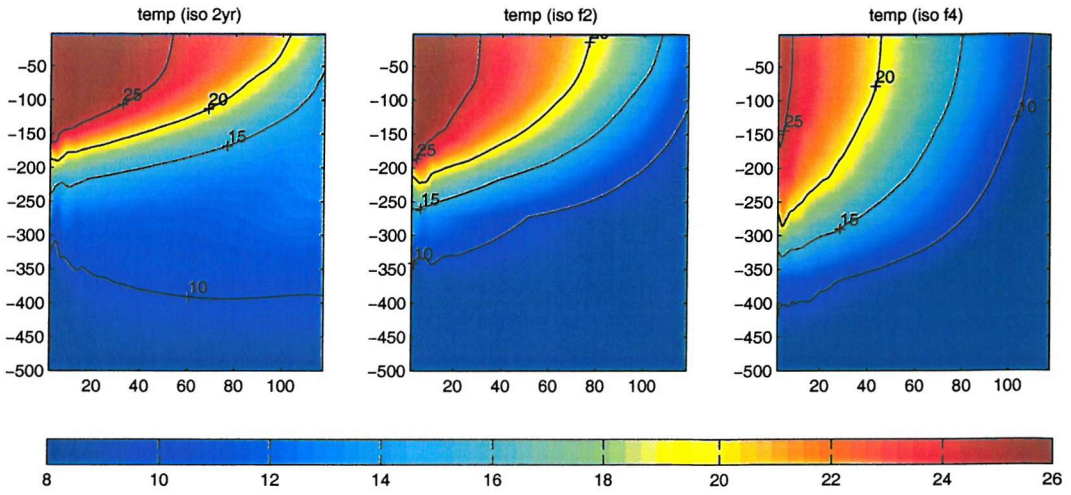

Figure 4.2: Along-Equator vertical annual mean temperature distribution. (iso 2yr, f2, f4).

Figures 4.3 and 4.4 show annual mean zonal velocity across a section at 80° longitude from 15°S to 15°N for the different mixing and background wind stress configurations respectively. The characteristic zonal circulation of the Equatorial region is evident, with an eastward flowing EUC and the two surface branches of the westward flowing SEC. As Figure 4.3 shows, increasing viscosity leads to a weakening of the zonal currents, while a decrease leads to an increase in the maximum velocity to over 1ms^{-1}. The depth of the EUC core does not change with the changing viscosity and remains throughout at a depth of 100m. While the vertical extent of the EUC is unaffected, the lateral distribution becomes progressively tighter as viscosity is decreased. The EUC in the high viscosity regime lies between 5° of the Equator, while in the low viscosity regime it is constrained within 2° of the Equator. Increasing the background wind field also leads to an increase in the maximum velocity of the EUC to over 1ms^{-1}, as shown in Figure 4.4. The vertical extent of both the EUC and SEC branches increases, with the EUC reaching depths of 700m in the f4 configuration, and the core of the EUC deepens to around 200m.

A comparison of the configurations addressing the sensitivity of the Equatorial circulation to lateral mixing with the sensitivity experiments by Maes et al. (1997) shows that we obain similar results showing the importance of lateral mixing in modelling the equatorial ocean. The EUC core is shallow in the high viscosity regime relative to the lower viscosity regimes. The following section demonstrates that we also find that the lateral mixing regime is an important consideration as it affects the Kinetic energy balance, and hence the dynamics of the EUC, and the meridional heat transport of the equatorial region. Maes et al. (1997) also found that a viscosity of $10^2\text{m}^2\text{s}^{-1}$, the low viscosity regime, gave an unrealistic vertical structure of the

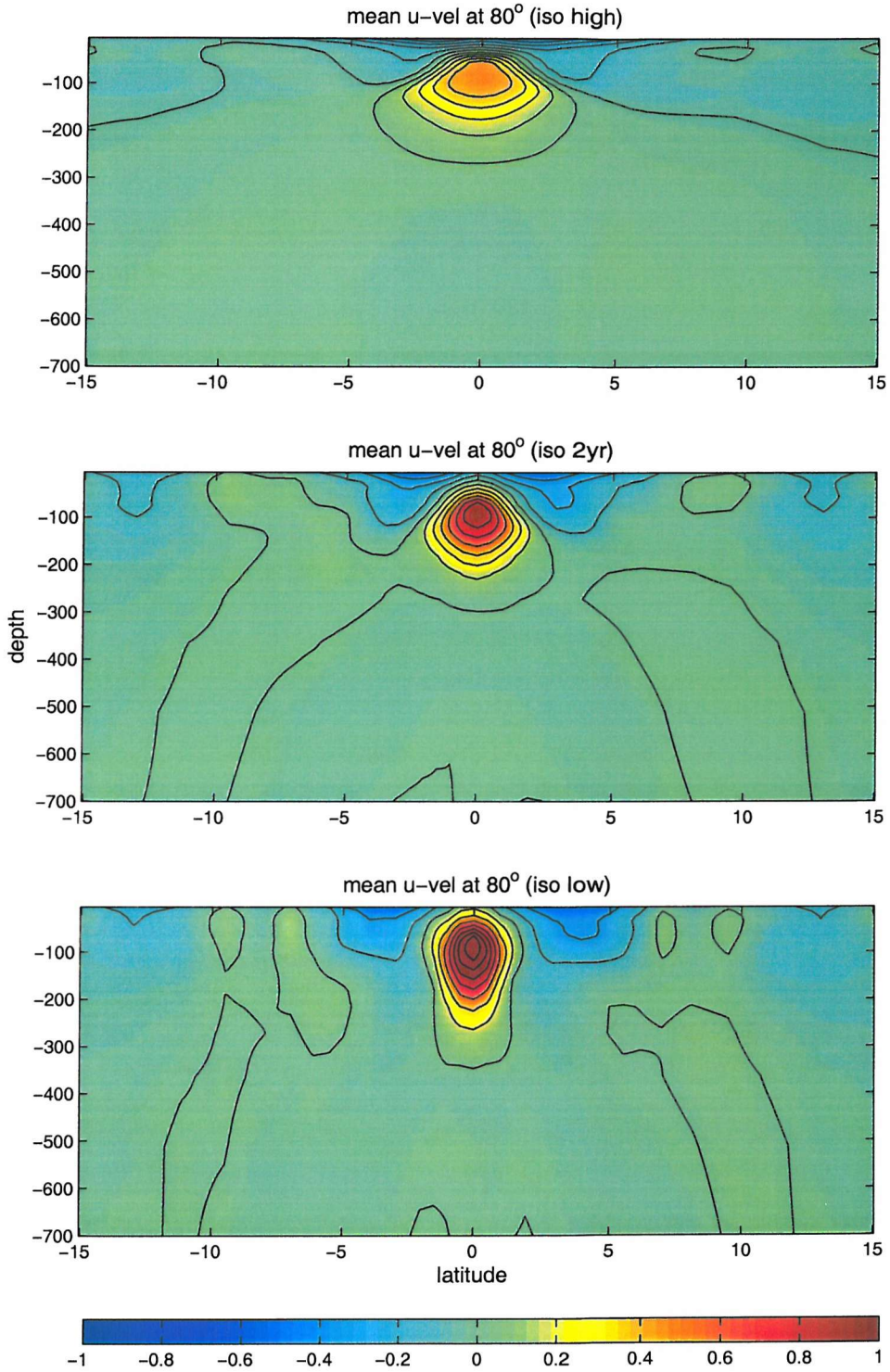

Figure 4.3: Annual mean zonal velocity vertical section at 80° longitude for high, standard and low viscosity (iso high, 2yr, low).

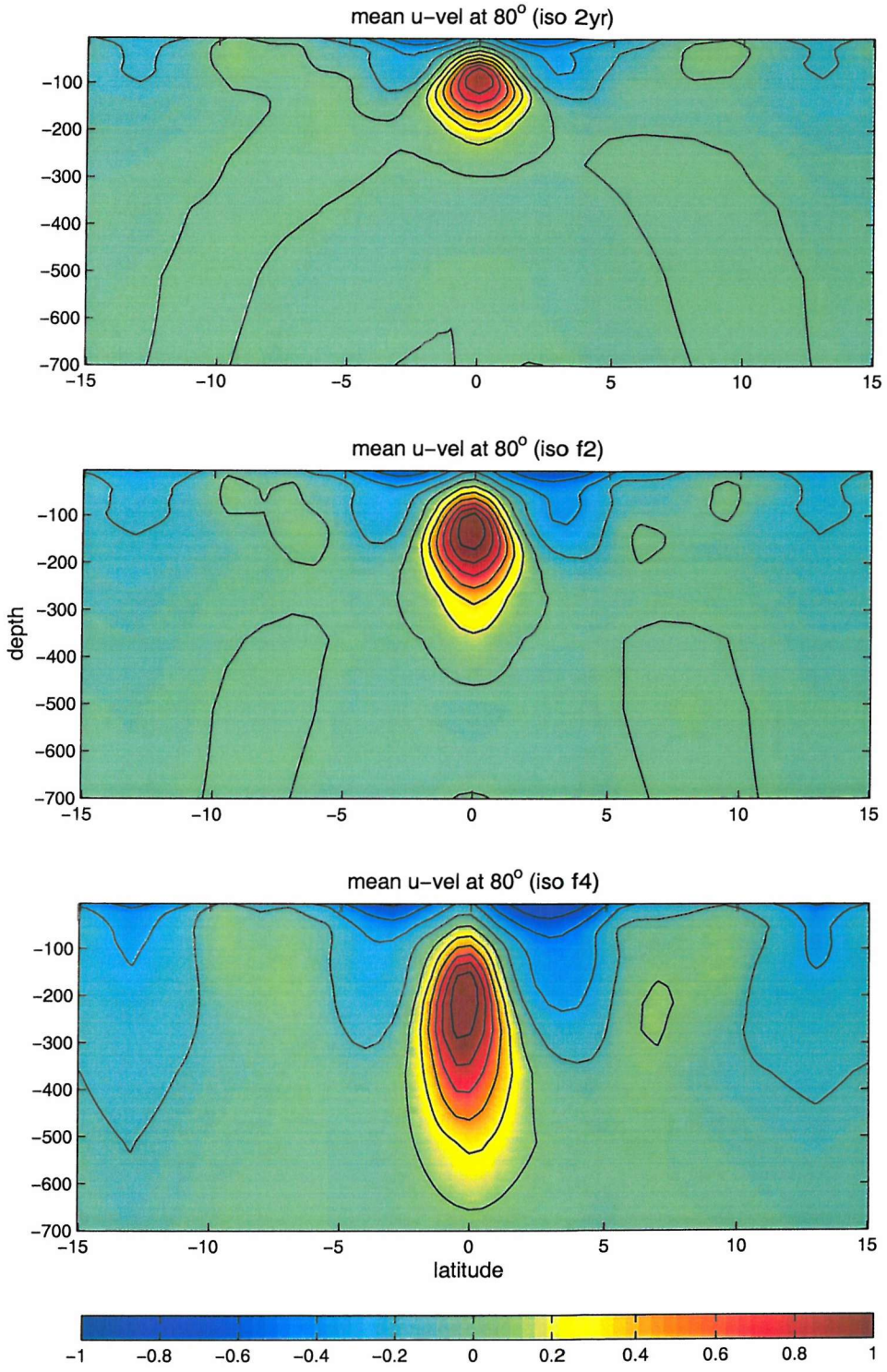

Figure 4.4: Annual mean zonal velocity vertical section at 80° longitude for the different wind stress regimes (iso 2yr, f2, f4).

equatorial current system. Observational results (Brady and Bryden, 1987) have shown that the eddy viscosity coeffiecients in the vicinity of the EUC to be of the order of $10^3 m^2 s^{-1}$. The results of the standard configuration confirm that a lateral viscosity of $10^3 m^2 s^{-1}$ is necessary for modelling this region, as found also by Maes et al. (1997).

4.2 Energy Balance Analysis

The Kinetic energy (KE) balance of the circulation is decomposed into the mean KE and eddy KE components to separate the mean component of the equatorial circulation from the eddy component, assuming that the eddy KE describes regions of TIW activity while the mean KE describes the distribution of mean flow. The calculation is made with two years of daily instantaneous meridional and zonal velocity data at a meridional section at 80° longitude from 15°N to 15°S. The KE balance is given by

$$KE_{total} = KE_{mean} + KE_{eddy} \tag{4.1}$$

$$KE_{mean} = \frac{1}{2}\rho(\bar{u}^2 + \bar{v}^2) \tag{4.2}$$

$$KE_{eddy} = \frac{1}{2}\rho(\overline{u'^2} + \overline{v'^2}) \tag{4.3}$$

where the overbar denotes a mean, which is calculated over two control years, and the prime the velocity anomaly calculated by subtracting the daily instantaneous fields from the mean during these two years. The middle panel in Figure 4.5 shows the mean and eddy KE field of the standard (iso 2yr) configuration. The equatorial zonally-dominated flow is closely related to the mean KE field, with a maximum at the core of the EUC. Surface peaks in mean KE, corresponding to the branches of the SEC, are asymmetric with greater penetration north of the Equator. As as result, the depth of the mixed layer is deeper north of the Equator. The eddy KE field calculated over two years is symmetric, while the instantaneous transient flow is asymmetric, as this depends on the seasonal cycle of the Tropical Instability Wave (TIW) field forced by the seasonally varying background wind field. The magnitude of eddy KE decreases away from the surface to the top of the thermocline.

The top and bottom panels of Figure 4.5, of high and low viscosity respectively, illustrate how the circulation is sensitive to horizontal mixing. The mean KE strengthens by an order of magnitude as viscosity is lowered and the zonal circulation intensifies. The vertical extent of the mean KE in the region of the EUC deepens, though the maximum remains at around -100m. The lateral extent of the EUC tightens so that it lies close to the Equator in the low viscosity case. The eddy KE also increases in magnitude as viscosity is lowered. The TIW field is absent in the high viscosity case, as it is damped out, though there is still a very weak eddy KE signature as two lobes poleward of the Equator. These lobes strengthen and are positioned further poleward as viscosity is decreased. In the low viscosity case the maximum in eddy KE of over $90 Jm^3$ is located at the Equator, with weaker peaks located at 5° either side of the Equator. This suggests that a low viscosity regime leads to an increase in barotropic instability at the Equator, with a weaker increase in baroclinic instability.

Linearly increasing the background wind field leads to a linear acceleration of the zonal circulation and increase in mean KE, as shown in Figure 4.6. The vertical extent of both the EUC and the SEC branches increases, with the EUC reaching a depth of over -600m in the f4 configuration, while being confined only to the top 200m in the standard configuration (iso 2yr). The eddy KE also increases in magnitude and vertical extent, with the strengthening of the maximum at the Equator to around $90 Jm^3$, as seen in the low viscosity case.

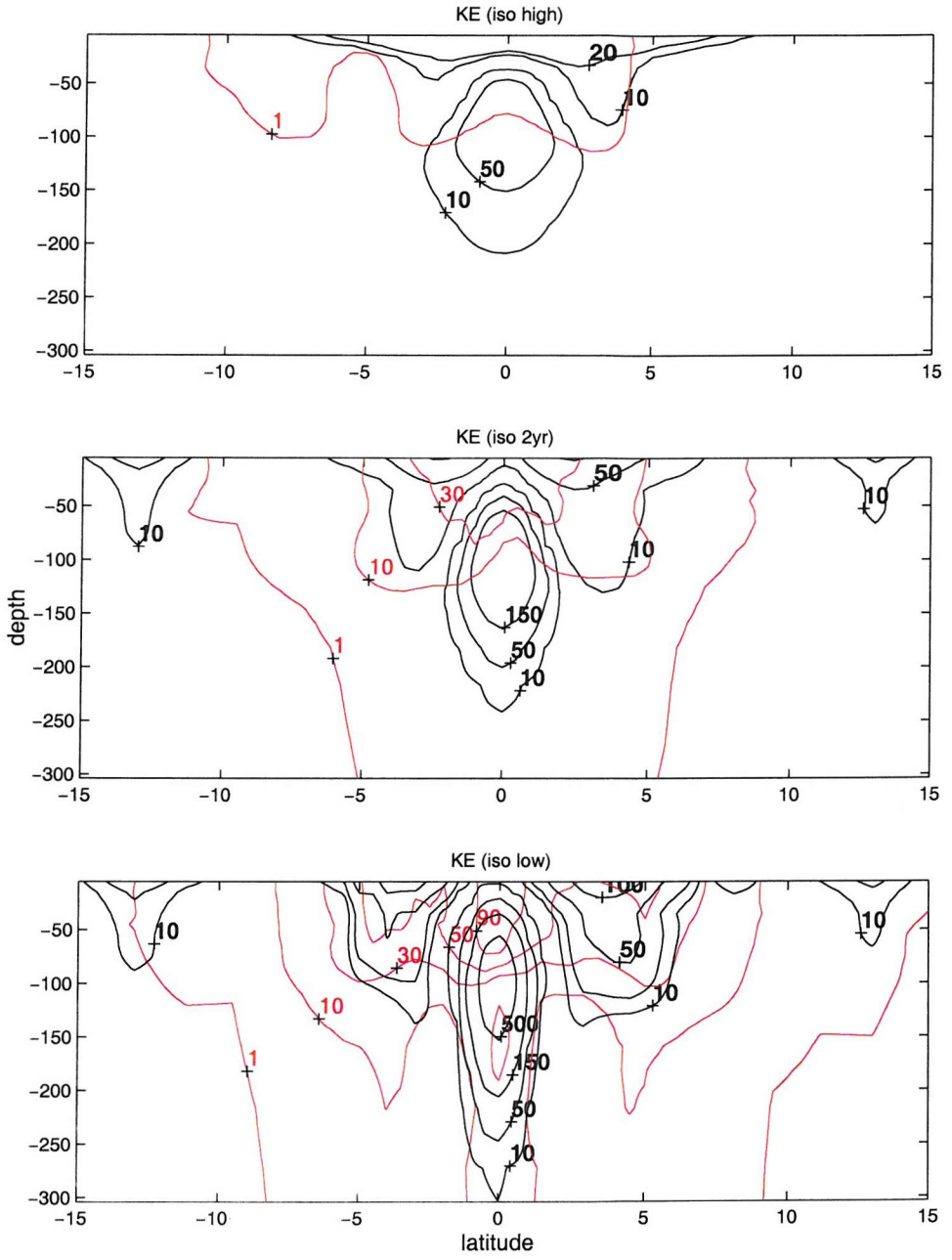

Figure 4.5: Meridional section at 80° longitude of mean Kinetic Energy (black) and eddy Kinetic Energy (red), in Jm^3, over the top 300m for the high, standard and low isopycnal mixing configurations (iso high, 2yr, low).

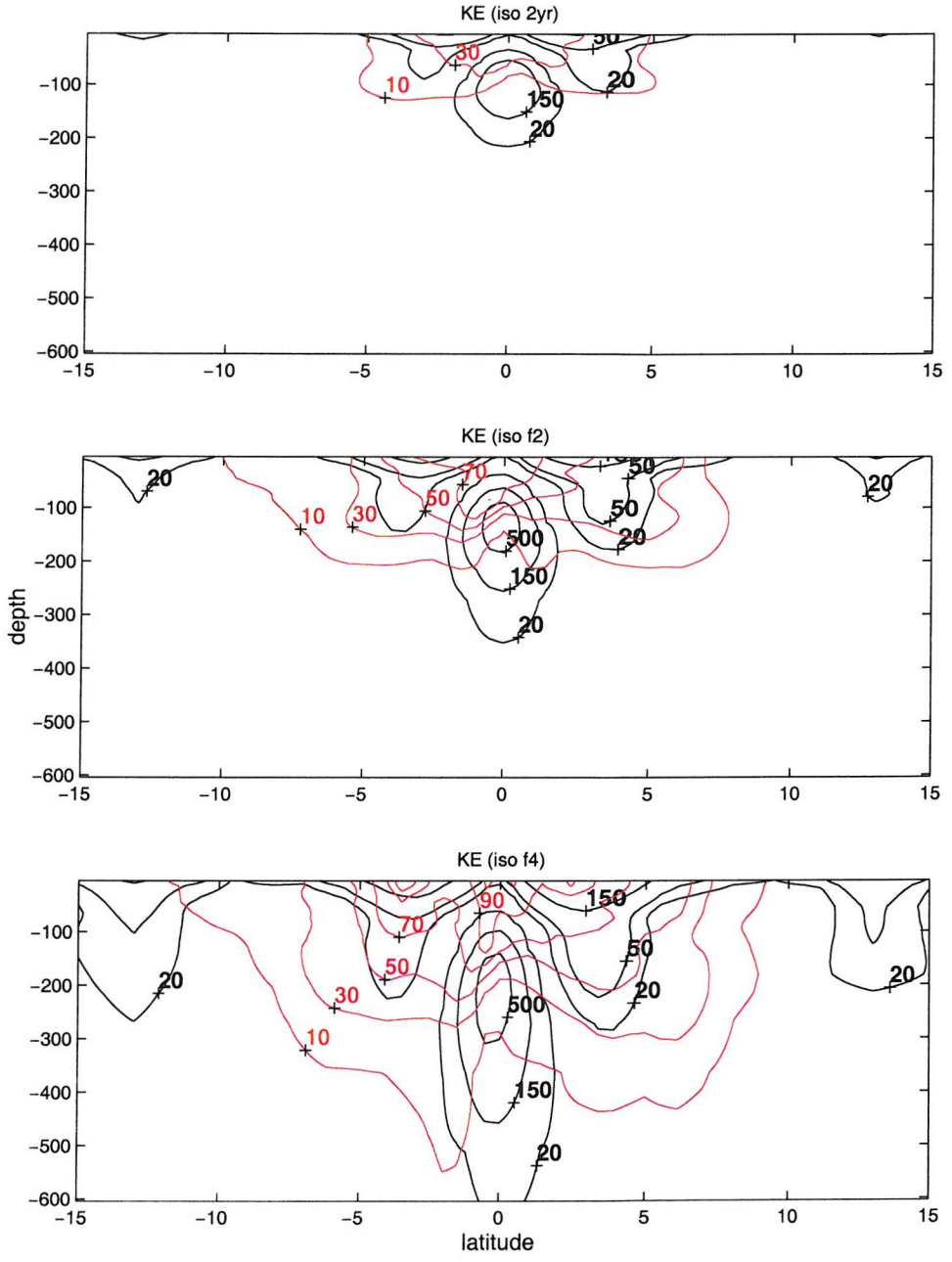

Figure 4.6: Meridional section at 80° longitude of mean Kinetic energy (black) and eddy Kinetic energy (red), in Jm^3, over the top 600m for different background wind stress configurations (iso 2yr, f2, f4).

4.3 Meridional Heat Transport

The annual mean, depth integrated meridional heat transport (MHT) has been calculated by linearly interpolating between meridional velocity and temperature sections from 15°N to 15°S at 60°, 80° and 100° longitude. The eddy component of the MHT has been calculated only for the 80° longitude section. This location was selected since there is the strongest TIW signal here in the standard configuration (iso 2yr). The total MHT is composed of a mean MHT component and an eddy MHT component, as follows

$$MHT_{total} = MHT_{mean} + MHT_{eddy} \tag{4.4}$$

$$MHT_{mean} = \rho_o C_p \int\int \overline{vT} dz dx \tag{4.5}$$

$$MHT_{eddy} = \rho_o C_p \int\int \overline{v'T'} dz dx \tag{4.6}$$

where ρ_o is the mean density (1020kgm^{-3} and C_p is the specific heat capacity (4093 JKg^{-1}K^{-1}). The overbar denotes a mean that is calculated over two years and the prime represents the anomlay calculated by subtracting the daily instantaneous fields from the mean. The analysis of the MHT budget in terms of the mean and eddy components gives an indication of the redistribution of heat by the mean and transient flow. The mean MHT budget in the upper equatorial Pacific region consists of a poleward flux of heat due to the divergence generated by the upper ocean circulation. This is compensated at depth by a convergence by the abyssal flow.

The MHT balance of the standard configuration (iso 2yr) is shown in blue in Figure 4.7. The mean MHT is poleward with a maxima at 5°N and 5°S of 5PW. The eddy MHT, due to the presence of the TIW field, opposes the mean MHT with an equatorward heat flux that is an order of magnitude smaller, with maxima of 0.3PW just within 5° either side of the Equator. The eddy MHT occurs in the upper 200m of the ocean, in good comparison with observations (Bryden and Brady, 1989).

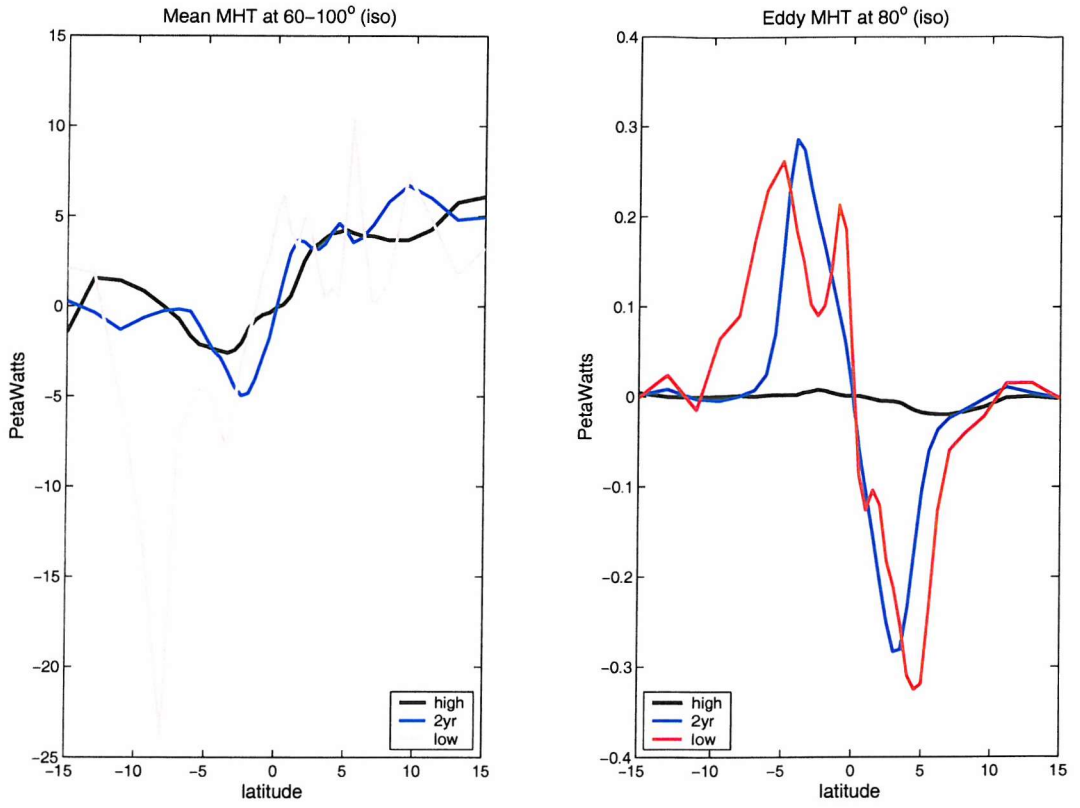

Figure 4.7: Mean Meridional Heat Transport calculated between 60° and 100°long and eddy Meridional Heat Transport at 80°long in the top 200m for different levels of isopycnal mixing (iso high, 2yr, low).

The response of the mean and eddy component of the MHT to increasing levels of horizontal mixing is shown in red and black in Figure 4.7. The fluctuations in the mean MHT, particularly in the low mixing case result from the meridional velocity integral being non-zero in this calculation. A consistent definition of the heat transport relies on the mass transport being zero. This problem results here as global output for the model domain was not available and the calculation had to be made by interpolation across meridional sections at 60°, 80° and 100° longitude, and not from the lateral boundaries. This problem arose due to data storage capacity limitations. Taking this into account, the changes in mixing regime do not modify greatly the mean MHT. The greatest poleward heat flux, of around 5PW, occurs in the Northern Hemisphere. The eddy MHT is sensitive to high levels of viscosity that damp out the TIW field, reducing the eddy MHT almost to zero PetaWatts. The eddy MHT results show similarity in magnitude either side of the Equator between the standard 2yr and low mixing configuration, of around 0.3PW, with the maximum being located slightly more poleward in the low mixing case.

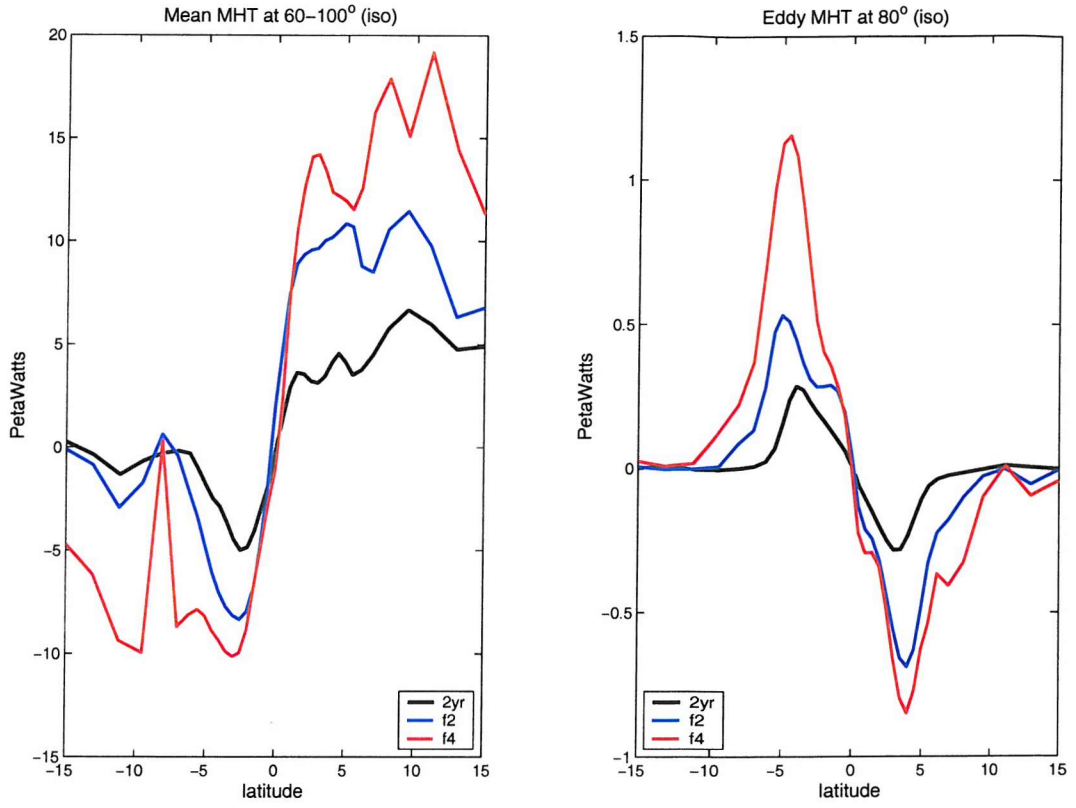

Figure 4.8: Mean Meridional Heat Transport calculated between 60° and 100°long and eddy Meridional Heat Transport at 80°long in the top 200m for the different background wind stress regimes (iso 2yr, f2, f4).

The MHT is sensitive to the background wind stress regime, as Figure 4.8 shows. There is an overall increase in the mean MHT from 5PW to 20PW as wind stress is increased, as the zonal circulation is strengthened and meridional divergence is increased. The eddy MHT also increases as the Tropical Instability Wave field becomes more energetic, increasing the equatorward heat transport. The vertical extent of the eddy MHT increases as wind stress increases, reaching depths of over 300m in the f4-wind regime, though this is not shown here. The increase in eddy MHT is greatest in the southern hemisphere for the f4-wind regime, reaching maximum levels comparable to the mean MHT of over 1.0PW.

4.4 Summary

The idealised configurations all simulate an Equatorial circulation dominated by zonal flow that leads to a poleward MHT. The upward tilting EUC lies within the thermocline, and there is a Warm Pool in the western basin and a Cold Tongue in the east. Reducing lateral viscosity leads to a tightening of the EUC. Simulating the TIW field, which is completely damped out when lateral mixing is set to $10^4(m^2s^{-1})$, is important due to the associated implications for the distribution of eddy KE and the equatorward MHT. Climate models often have a resolution that is too low to simulate the TIW field and find a persistant cold bias in the eastern Equatorial Pacific as a result. The following chapter will describe the TIW field and its sensitivity to different regimes in more detail.

Successively increasing the background wind field leads to a more energetic zonal circulation and an increase in the eddy KE and MHT due to the increase in TIW activity. The increase in mesoscale mixing that results from the increase in wind stress reduces the extent and maximum SST of the Warm Pool and increases upwelling in the eastern basin, with the Cold Tongue reaching the western basin. The thermocline becomes successively steeper as wind stress is increased, providing a basis with which to study the propagation of a WWE-forced Kelvin wave along a steep thermocline gradient.

Chapter 5

Tropical Instability Waves

5.1 Introduction

Tropical Instability Waves (TIWs), were first observed in current meter data in the Equatorial Atlantic Ocean by Düing et al. (1975) and in infra-red images of the Pacific Ocean by (Legeckis, 1977). Figure 5.1 shows Advanced Very High Resolution Radiometer (AVHRR) composites of SST showing the TIW field in the Equatorial Pacific. The surface cusp-shaped features are the signature of three-dimensional vortices driven by shear instability (Flament et al., 1996; Kennan and Flament, 2000). TIWs have a zonal wavelength of 700-2000km, a period of 20-40 days and a phase speed of 20-80cms^{-1} (Qiao and Weisberg, 1995). A TIW signature is always observed when the meridional SST gradient at 140°W is greater than 0.25°C per 100km (Contreras, 2002). TIWs have a strong seasonal cycle, closely related to the seasonal variability of the wind field, mean flow and thermal structure of the Equatorial region. The background flow becomes unstable from around June with a maximum during boreal summer and winter with a quiescent period of low TIW activity during the spring period (Vialard et al., 2003).

On interannual timescales, TIW activity is strongest during La Niña conditions and weakest during El Niño conditions. TIWs are a source of negative feedback in the ENSO cycle as, during La Niña years, the enhanced level of eddy activity that brings warm water to the Equator acts against the development of cold SST anomalies in the Eastern Pacific (Vialard et al., 2001). This may be a factor involved in maintaining the asymmetry between the generally stronger warm and weaker cold ENSO events.

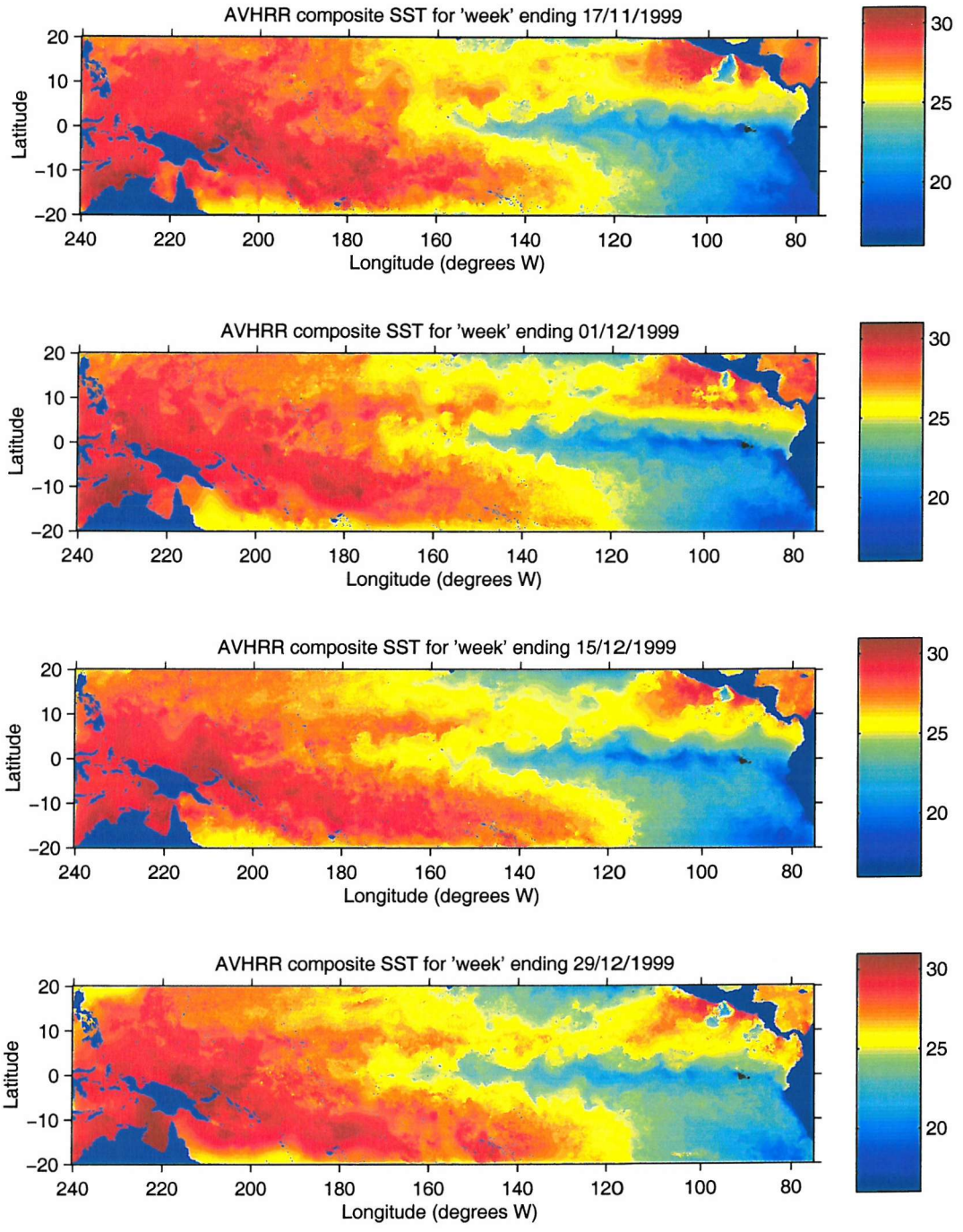

Figure 5.1: AVHRR composites of SST in November and December 1999 showing the westward propagation of the cusp-like features associated with TIWs visible in the region of the strong SST gradient delimiting the extent of the Cold Tongue (courtesy of Prof. K. Richards).

Philander (1976) modelled the zonal equatorial flow affected by the β-plane and divergence with $1\frac{1}{2}$ and $2\frac{1}{2}$ layer models and, through linear stability analysis, found the flow instability to be due to the shear between the South Equatorial Current and the North Equatorial Countercurrent. This was then confirmed by GCM simulations of the equatorial region with spatially constant winds (Semtner and Holland, 1980) and with monthly mean winds (Cox, 1980), attributing baroclinic instability as the main instability process. Spatially constant winds generate waves symmetrically about the Equator (Semtner and Holland, 1980) but observed waves are generated mainly north of the Equator due to the non-symmetric wind field and associated velocity and temperature distribution.

Despite modelling studies of varying complexity being successful in reproducing instability waves of a similar nature to those observed, the processes that generate the instabilities have not yet been explained conclusively as there are multiple sites and processes generating the instabilities. The equatorial region of TIW activity in the eastern Pacific is generated by barotropic instability that draws on the Kinetic Energy (KE) of the mean flow. The northern region of TIW activity in the Eastern Pacific is generated by baroclinic instability arising from the reservoir of available Potential Energy (PE) generated by the strong meridional temperature gradient that maintains an equatorial temperature front. The dominant process affecting the barotropic conversion term is the strong meridional shear between the EUC core and the northern branch of the SEC (Yu et al., 1995; Masina et al., 1999). Decreasing viscosity leads to an increase in barotropic instability due to the increase in shear between the EUC and SEC (Pezzi and Richards, 2003).

The magnitude of the mean baroclinic conversion term in the eastern Pacific is greatest in the region 1°N-5°N, in the upper 300m, coinciding with the strong meridional temperature gradient, which is maintained by wind-driven upwelling and surface divergence. This, combined with the weakly stratified mixed layer, leads to the presence of a eddy PE reservoir available for baroclinic conversion (Yu et al., 1995; Masina et al., 1999). Baroclinic instability appears to be due to the variable upper ocean temperature field (Philander et al., 1992) referred to a frontal instability (Yu et al., 1995). South of the equator the baroclinic conversion term is weaker and shallower, reflecting the shallower mixed layer and weaker meridional temperature gradient (Masina et al., 1999).

The SEC has a key role in maintaining the observed TIW phase speed as there is a correlation in the variability of the near surface current speeds and TIW phase speeds (Contreras, 2002). The most important factor in determining wavelength is the magnitude of the meridional velocity shear, not the strength of the currents (Philander, 1978).The strength of the SEC determines the period of the instability waves, with waves with a shorter period being generated when the current is stronger (Cox, 1980; Seigel, 1985). Even though there is a comparable shear regime between the southern SEC branch and the EUC, this region is not barotropically unstable. The north-south asymmetry in TIW activity has not been attributed to the presence of the NECC but to the asymmetries in the SEC branches and the equatorial temperature front (Yu et al., 1995).

The region of TIW activity south of the Equator in the eastern Pacific region is not explained by a local energy analysis (Masina et al., 1999). The presence of an eddy KE maximum is therefore attributed to a non-local source that has been redistributed through the advection and divergence of energy. Horizontal and vertical KE advection explains part of the signal, with vertical advection being the dominant subsurface term, suggesting that KE is being advected upwards from the bottom of the mixed layer. At depth there is also a positive eddy pressure flux resulting form horizontal and vertical divergence. Wavelet analysis of the meridional velocity field south of the Equator in the central Pacific shows that the wave signal maximum is in the thermocline, suggesting that the instability seems to be generated below the surface, in contrast to the instability region north of the Equator (Masina and Philander, 1999).

The first half of this chapter will describe the TIW field of the different configurations, discussing the seasonal variability, the sensitivity to lateral mixing and the TIW field that results when the background wind stress is gradually increased, this itself being a source of mixing. The second half of the chapter will study the impact of a WWE-forced Kelvin wave on the background TIW field and how the TIW field in turn affects the propagation of the Kelvin wave.

5.2 The Model TIW Field

The standard model control run (iso 2yr) simulates TIWs with the same basic characteristics as those observed in the Equatorial Pacific, though the cusp-shaped features are visible either side of the Equator as the model configuration is more symmetric. The characteristics of the TIWs are sensitive to the specific configuration used, where wind stress, horizontal mixing tensor orientation and strength are varied. Figures 5.2 and 5.3 show the SST signature of the TIW field for the different configurations, where the level of isopycnal mixing and the background wind stress are varied.

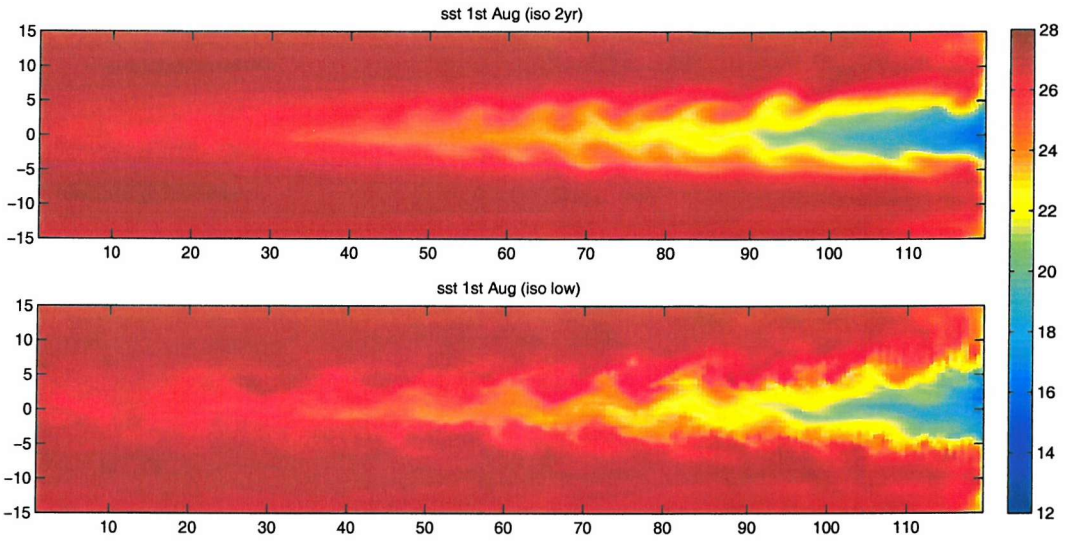

Figure 5.2: SST for 1st August (iso 2yr low).

The top panel of both figures shows the standard configuration TIW field. The wavelength of the TIWs in the standard configuration is just under 1000km, comparing well with observations of TIWs in the Pacific having a wavelength of 700-2000km. The model domain effectively represents the Equatorial Pacific from the eastern boundary at 80°W to 200°W, so that the TIW extends further west than in reality and there is a less extensive Warm Pool in the western basin. The westward extent of the TIW field increases slightly as viscosity is reduced, and considerably when the background wind field is increased. The wavelength increases as well. In the low viscosity case, it increases to over 1000km and the structure of the cusp-shaped features becomes more filamented. The wavelength increases to over 1000km in the f2 case and to around 2000km in the f4 case, always within the scale found in observations.

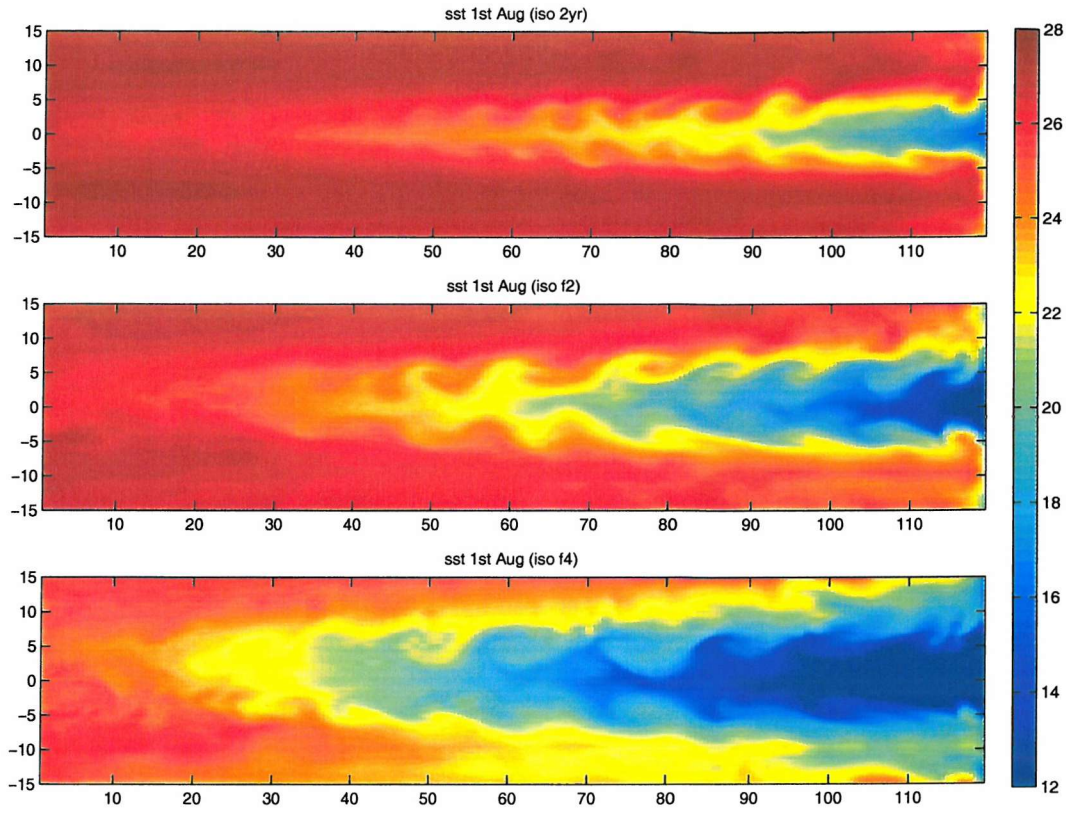

Figure 5.3: SST for 1st August (iso 2yr f2 f4).

After a ten year spin up integration, the seasonal cycle is well established, as shown previously by Figures 3.1 and 3.2. Successive years are not identical, as Figure 5.4 shows the timeseries of surface meridional velocity at 2°N, the Equator, and 2°S at 80° longitude for years 11 and 12 after the spin up period. Year 11 is shown in red and year 12 in blue, with year 12 lagging behind the year 11 cycle. The regularity of the oscillations seen at the Equator have also been identified in observations and have been attributed to barotropic instability. North and south of the Equator the variability is attributed more to baroclinic instability. The quiescent period in TIW activity is visible at all the three latitudes, but more clearly so poleward of the Equator. The variability observed between the different latitudes results from the asymmetric wind stress forcing and temperature and salinity relaxation fields. It is also a consequence of the non-linear nature of the TIW dynamics and their interactions with the mean flow (Masina and Philander, 1999).

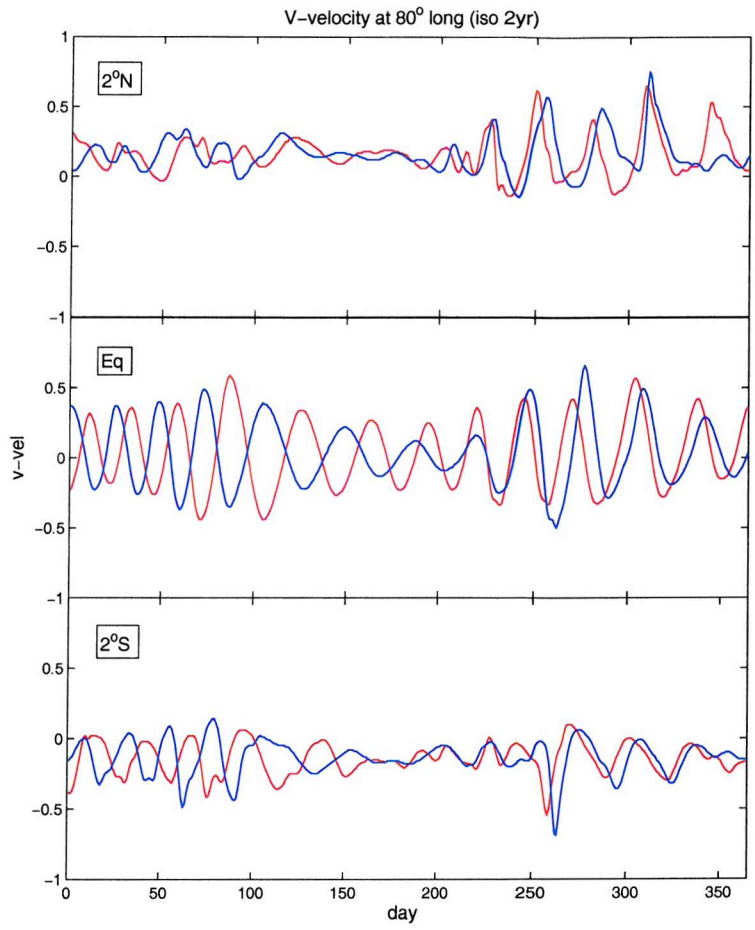

Figure 5.4: Surface meridional velocity (ms^{-1}) timeseries at 2°N, the Equator, and 2°S at 80°long for model years 11 (red) and 12 (blue) (iso 2yr).

Figure 5.5 shows the surface meridional velocity timeseries of year 11 at different locations (40, 60, 80 and 100°) along the Equator, together with the amplitude spectrum calculated for the timeseries of both years 11 and 12. Periods greater than 50 days are excluded in the plot to isolate the variability related to the TIW field. The total meridional velocity field is considered without performing any filtering as it is the field with the strongest TIW signature (Masina and Philander, 1999) and filtering does not modify the timeseries significantly. The period varies between 25 to 35 days and the amplitude spectrum increases from west to east, slightly decreasing again at 100°long, suggesting that TIWs are not generated at the eastern boundary itself, but west of it. In the case of the high viscosity regimes, the TIWs are completely damped out, but there is nevertheless a poleward meridional velocity of between 0.1 and 0.2ms^{-1} at 2°N and 2°S of the Equator.

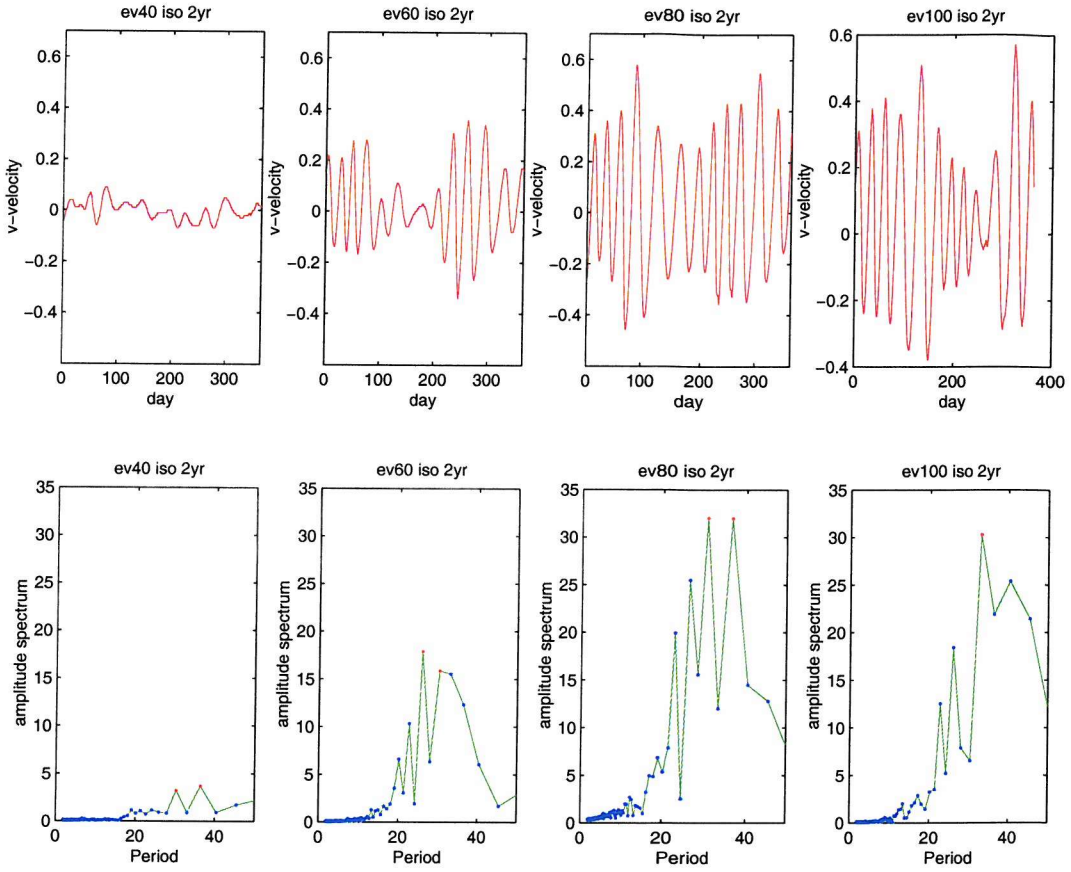

Figure 5.5: v-velocity (ms^{-1}) timeseries at locations on the Equator, with corresponding spectral amplitude (iso 2yr).

TIWs are a near-surface instability and have a vertical extent that reaches the depth of the thermocline. The motion related to the the instability waves is mostly concentrated above the thermocline, but by no means confined there. The surface instability generates internal Rossby-gravity and Rossby waves that propagate downwards and away from the region of eddy activity (Philander, 1978; Cox, 1980; Brentnall, 1999; Masina and Philander, 1999). Figure 5.6 shows a vertical section of meridional velocity below 200m at 80° longitude at the Equator with evidence of TIW-related energy propagating to the abyss. The figure shows the full depth of the ocean, though excluding the top 200m as the meridional velocities associated with the TIWs are an order of magnitude stronger than the sub-thermocline velocities. The downward propagation of energy from the TIW field means that the representation of TIWs in models is important in terms of being a source of energy for the Equatorial deep ocean. The role of the Equatorial deep ocean is often neglected in modelling studies as it is treated as an area of no motion.

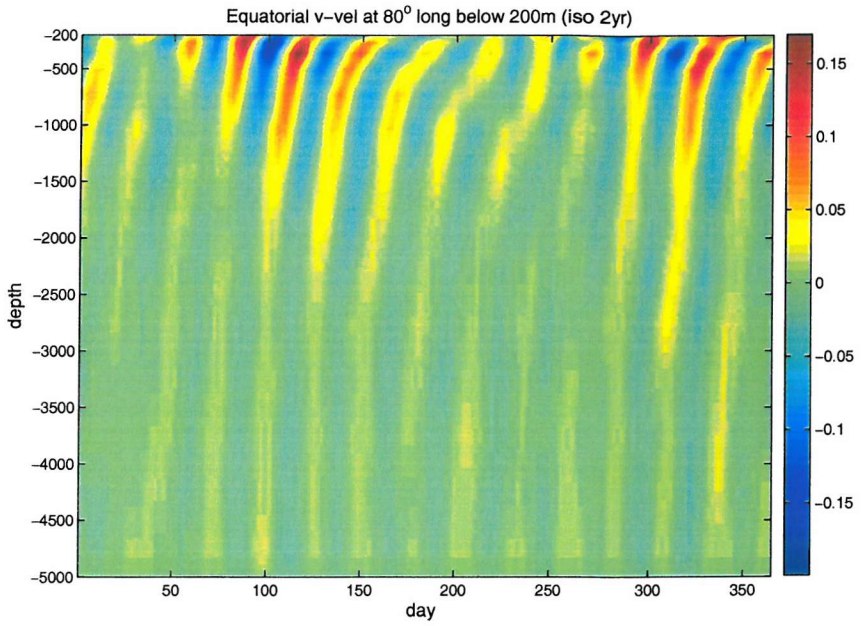

Figure 5.6: Equatorial meridional velocity (ms^{-1}) timeseries for year 11 below 200m at 80° longitude(iso 2yr).

5.2.1 Seasonal Variability

The model TIW exhibits seasonality as it is forced by the seasonally varying Hellerman and Rosenstein (1983) wind climatology. The top left hand panel of Figure 5.7 shows a Hovmöller plot of meridional velocity along 2°N of the standard configuration (iso 2yr). The strongest period of TIW activity is during the boreal late summer, autumn and winter. The quiescent period occurs later than in observations, commencing in July, instead of June, and finishing at the end of August. During the periods of TIW activity, at the beginning and at the end of the year, the TIWs extend in to the central, western basin. The bottom panel of Figure 5.7 of the timeseries of meridional velocity at 80° longitude for the standard configuration, in red, shows that the second half of the year is the most energetic.

Increasing the viscosity damps out the TIW field altogether. Lowering the viscosity produces a more irregular TIW structure, as shown in the top right hand panel of Figure 5.7. There is no clearly defined quiescent period, though there is a reduction in activity that remains to a certain extent in the late spring. The instabilities extend further west, across the whole of the domain, compared to the standard (iso 2yr) case. However, the additional variability in the low viscosity TIW field is the result of the emergence of numerical noise than due to a modification of the physical processes associated to TIWs. The timeseries in the lower panel of Figure5.7 shows that the amplitude of the TIWs is comparable for the periods of activity at beginning and end of the year. Adequately representing the mesoscale field, which is clearly

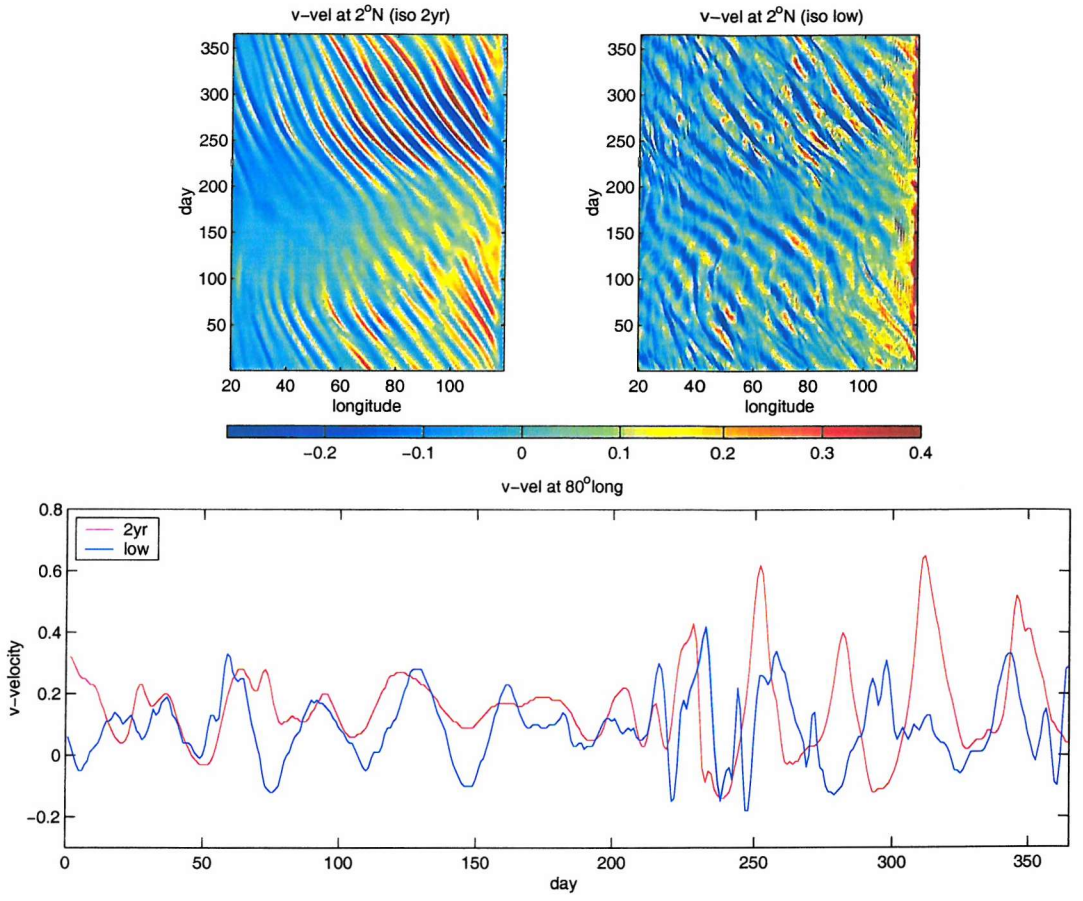

Figure 5.7: Surface meridional velocity (ms^{-1}) 2°N during year 11 and timeseries taken at 80° longitude - mixing sensitivity (iso 2yr low).

sensitive to the level of horizontal mixing, in Equatorial modelling is an important issue. Mixing schemes generally only allow for constant horizontal viscosity and diffusivity values. A scheme where mixing is enhanced at the Equator and enables the use of lower levels of viscosity off the Equator generates a well developed TIW field, while preventing the development of unrealistically strong equatorial currents (Pezzi and Richards, 2003).

A different view of the seasonality of the TIW field and its sensitivity to lateral mixing is shown by the temporal evolution of daily meridional velocity over year 11 along 80° longitude from 15°N to 15°S is shown in Figure 5.8. The standard configuration exhibits a TIW field that is comparable to observations, with a maximum in activity in the boreal summer-autumn period and another weaker period of activity in the spring with the maximum velocities located north of the Equator. There is some coherence in the structure of the velocity structure across the Equator. In the low mixing case, the nature of the TIW field has additional regions of instability at the Equator that are related to the peak in eddy KE observed for the low viscosity

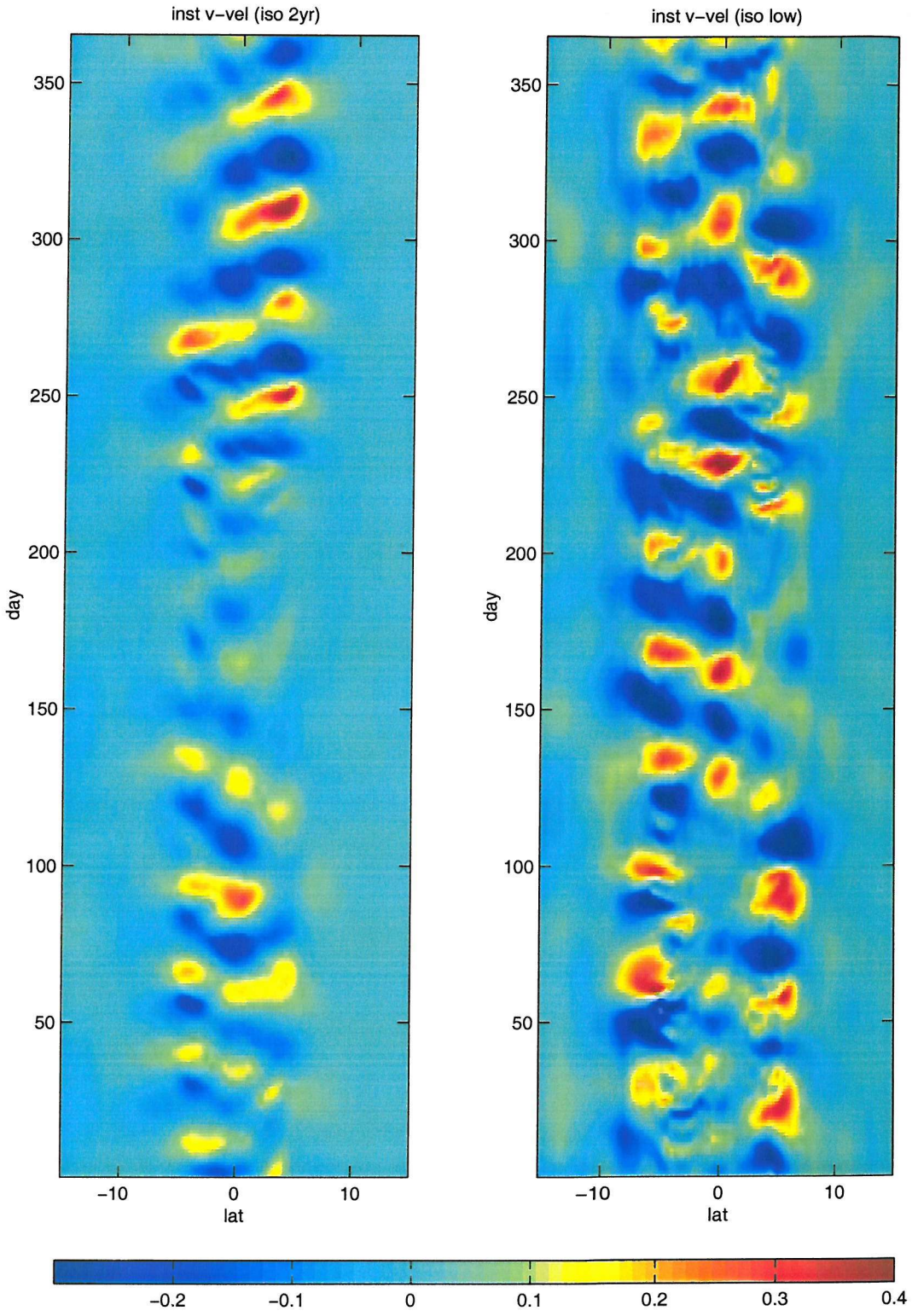

Figure 5.8: Daily meridional velocity (ms^{-1}) along 80°long, averaged over the top 17 levels (iso 2yr low).

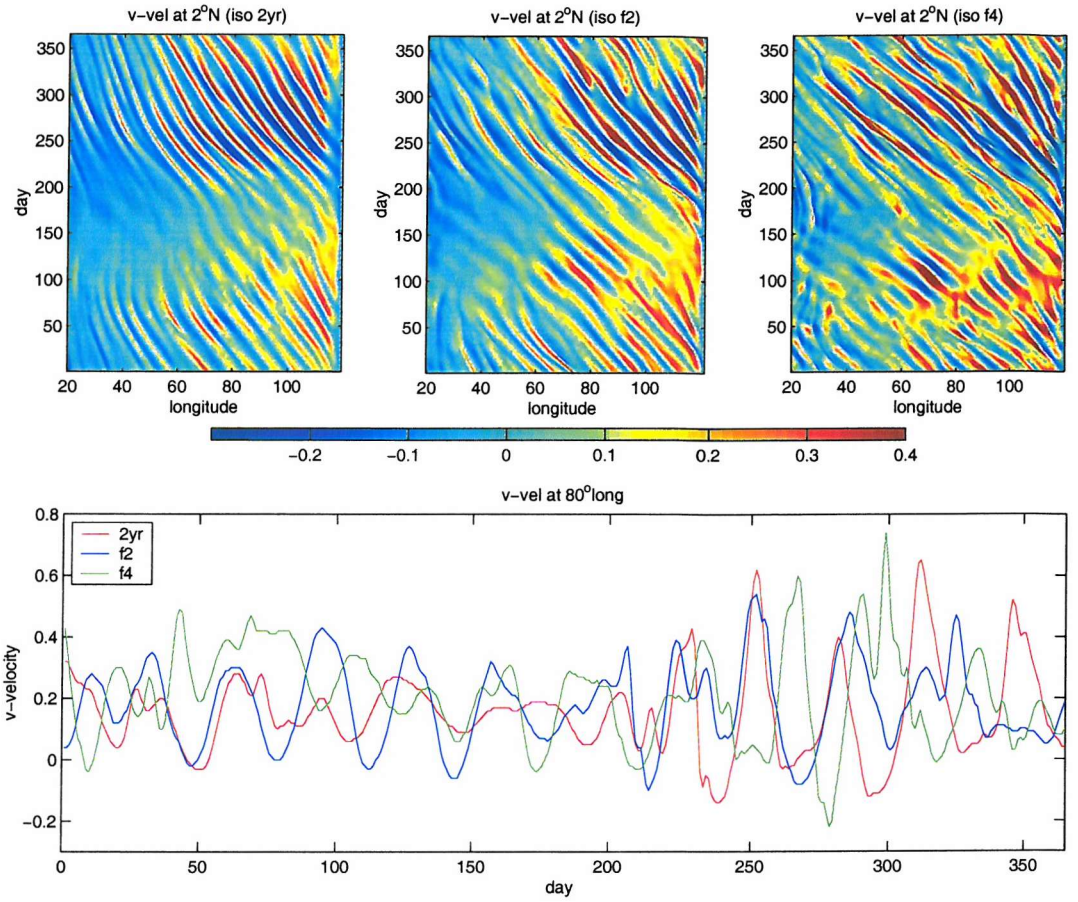

Figure 5.9: Surface meridional velocity (ms^{-1}) 2°N during year 11 and timeseries taken at 80° longitude - wind stress sensitivity (iso 2yr f2 f4).

configuration shown previously in Figure 4.5. This agrees with findings by Pezzi and Richards (2003) where a decrease in viscosity leads to an increase in barotropic instability at the Equator, as well as a weak increase in baroclinic instability poleward of the Equator.

The meridional extent of the TIW field increases in the low viscosity regime with the associated meridional velocity field spanning a region of 10° either side of the Equator, while the TIWs in the standard configuration are within 5° of the Equator. It must be noted that the horizontal grid of the model configuration has a resolution change here, where the meridional grid spacing gradually increases poleward to reduce computational cost. While a lower viscosity regime may simulate more eddy activity in the equatorial region, it is also necessary to increase resolution over a wider area to spatially resolve this increased activity.

Figure 5.9 shows the meridional velocity field at 2°N over model year 11 under different wind stress regimes. The bottom panel shows the timeseries for each regime taken at 80° longitude. Increasing the background wind stress leads to an increase in amplitude of the oscillations in the meridional velocity. However, after the increase in amplitude observed for the f2 case, the amplitude does not increase greatly in the f4 case. The structure of the instabilities becomes more chaotic when the wind stress is multiplied by a factor of four (iso f4). The breakdown in structure of the instabilities could be an indication of instability wave breaking (Brentnall, 1999). The frequency also increases as wind stress is increased and the quiescent period is eroded with TIWs appearing all year round throughout the basin.

5.2.2 Wavelet Analysis

A 2-D wavelet analysis (Torrence and Compo, 1998) is performed on timeseries of v-velocity of year 11 at 80° longitude at the Equator. Wavelet analysis is used to resolve the considerable temporal variability of the TIW field throughout the year, while a Fourier analysis would only consider the mean spectral characteristics of the timeseries. Figure 5.10 shows the analysis for the standard and low viscosity configurations. The top panels show the timeseries. Below, the wavelet power spectrum identifies the periods of coherent variability related to the presence of TIWs that are identified in red with time, against period. The thick black lines show the 95% confidence interval. The bottom panels show the associated variance, giving an indication of the spread in period.

The Equatorial meridional velocity signal at the Equator does not have the distinct quiescent period visible previously at 2°N in Figure 5.4, though there is a reduction in amplitude, period and variance in the boreal spring. The variance in period increases to between 16 to 31 days, during the active TIW phases in early spring and late summer. Reducing the viscosity increases the amplitude of the oscillations during spring and summer. The variance in period during this time increases by over a factor of ten, compared with the variance in the standard configuration (iso 2yr), varying between 16 and 64 days. This has quantified the increase in variance of the TIW field in a low viscosity regime that we have seen in it spatial distribution. The variance in period mainly increases in the second half of the year, while the first 100 days are comparable to the standard configuration.

The wavelet analysis of the Equatorial meridional velocity at 80° longitude during year 11 is repeated for the different background wind stress regimes, as shown in Figure 5.11. Doubling the background wind stress increases the variance in period to more than double that of the standard configuration. However, doubling the wind stress again does not lead to a further increase in variance. Variability increases during the year though, with the oscillations changing in amplitude throughout the year. The seasonal signal that was clearly visible in the standard configuration is not evident in the higher background wind stress configurations.

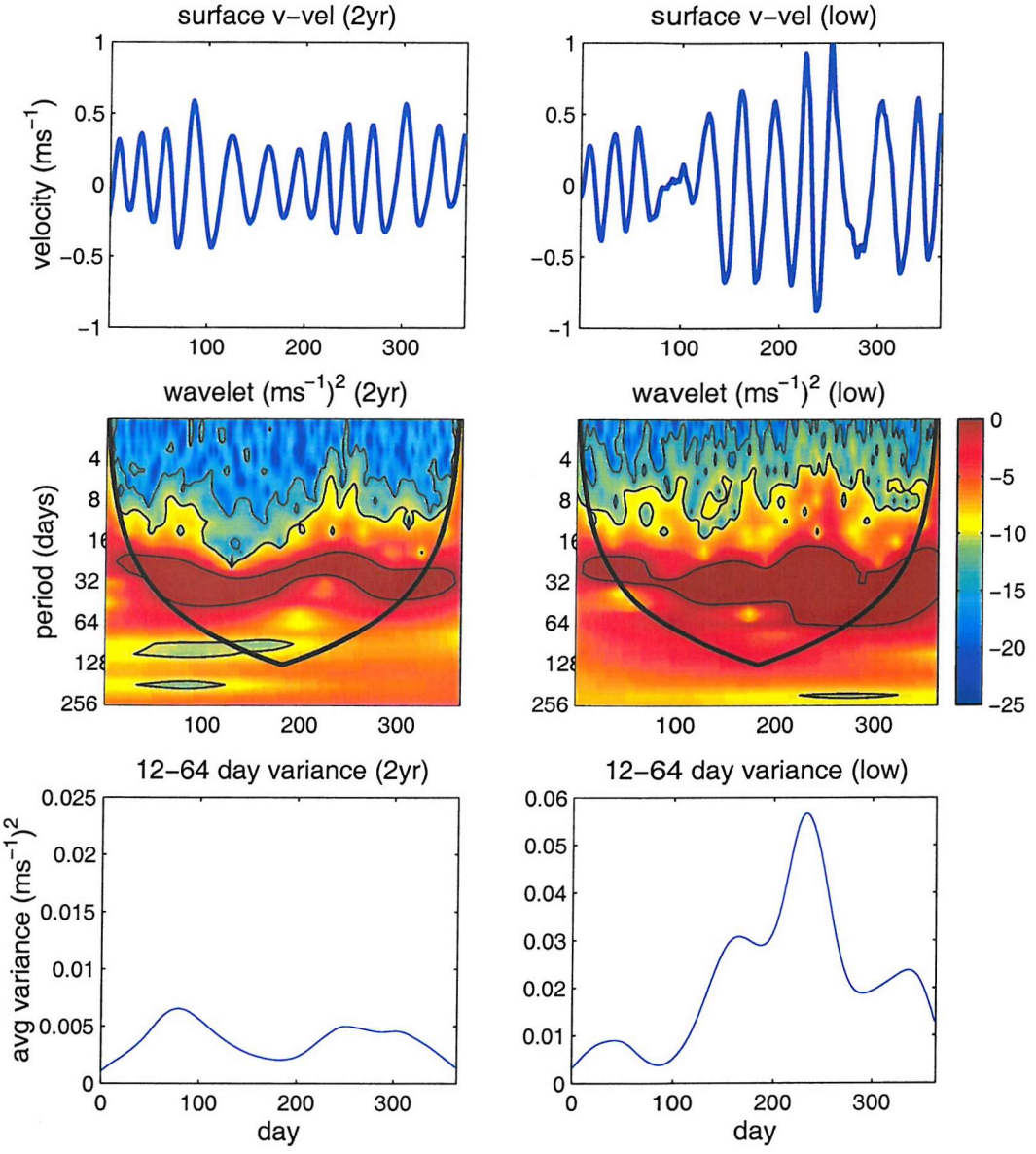

Figure 5.10: Wavelet analysis of equatorial meridional velocity year 11 timeseries taken at 80° longitude for the standard and low viscosity regimes. The top panels show the velocity timeseries, the second the wavelet spectrum, and the bottom the variance of the 12-64 day scale-averaged timeseries. (iso 2yr low).

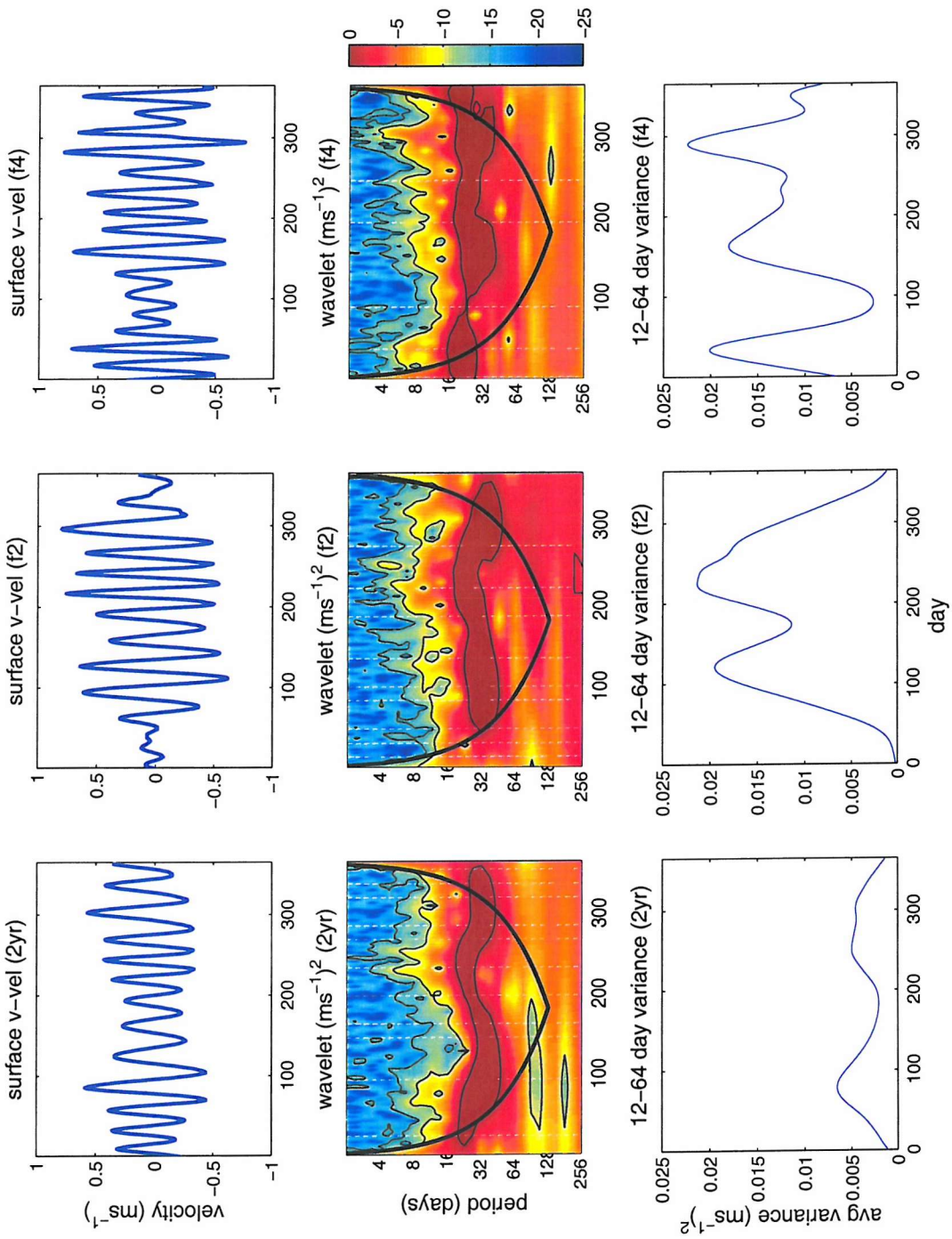

Figure 5.11: Wavelet analysis of equatorial meridional velocity year 11 timeseries taken at 80° longitude for different wind stress regimes. The top panels show the velocity timeseries, the second the wavelet spectrum, and the bottom the variance of the 12-64 day scale-averaged timeseries. (iso 2yr f2 f4).

5.3 Interactions with a WWE-Forced Kelvin Wave

The modulation of the Tropical Instability Wave (TIW) field of the Pacific Ocean by a Kelvin wave generated by a Westerly Wind Event (WWE) was first documented by Harrison and Giese (1988). Their model results show meridional velocity and SST anomalies generated along the Equator related to a passing Kelvin wave. The meridional velocity anomaly is unexpected as a linear Kelvin wave only generates zonal velocity anomalies. The occurrence of such anomalies suggests that the background flow is perturbed by the Kelvin wave, altering the background shear. Giese and Harrison (1991) found that the propagation of anomaly signals depends significantly on propagation by instability waves, the amplitudes of which are increased by the shear in the water column created by a downwelling Kelvin wave. More recently, Benestad et al. (2002) also suggested that TIWs and Kelvin waves may interact through the perturbation of the background velocity field, which may lead to the generation of further instabilities.

Allen et al. (1995) suggested that the Rossby waves generated by the reflection of an incoming Kelvin wave at the eastern boundary could be responsible for 'phase locking' the TIW field. The reflecting Rossby waves may actually constitute the TIW field (Benestad et al., 2001), or at least impart coherence on the TIW field (Lawrence et al., 1998; Lawrence and Angell, 2000). Benestad et al. (2001) find that the phase of the TIWs is most sensitive to local wind stress variability, but that they may also be affected by remote wind stress variability though the arrival of Kelvin waves. In the perturbation experiments performed here, a WWE is initiated in the western basin at different times of year 11. The following results show the eastward propagation of the Kelvin wave that is generated by the WWE into the region of TIWs. The WWEs are initiated to coincide with the periods of seasonally enhanced or reduced TIW activity observed in the standard configuration.

Figure 5.12 shows snapshots of SST anomalies resulting from the Kelvin wave generated by a wind event in February for the standard configuration. The Kelvin wave generates a SST signature as it propagates away from the WWE source. The positive and negative anomalies remain coherent for 20-30 days after the Kelvin wave has propagated further east, with anomalies still present in the central basin when the Kelvin wave reaches the eastern boundary. A weaker anomaly results west of the WWE site due to the westward propagating Rossby wave forced by the WWE. The SST anomalies propagate westwards after the occurrence of the Kelvin wave if daily snapshots are viewed as a movie. These features occur in the central and eastern end of the basin, where the background TIW field is present. The SST anomalies

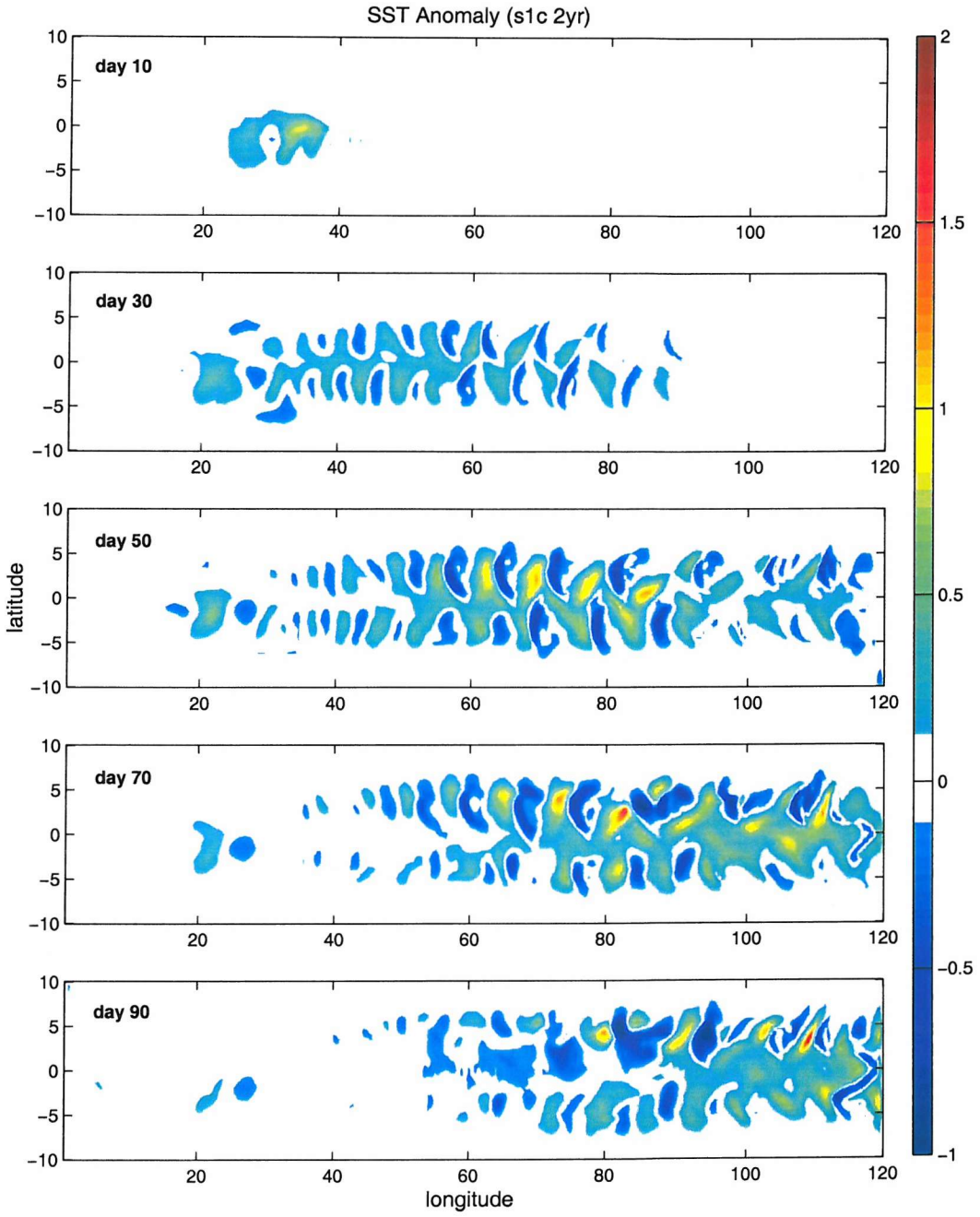

Figure 5.12: Snapshots of SST anomalies generated by a Kelvin wave propagating away from a WWE (s1c 2yr).

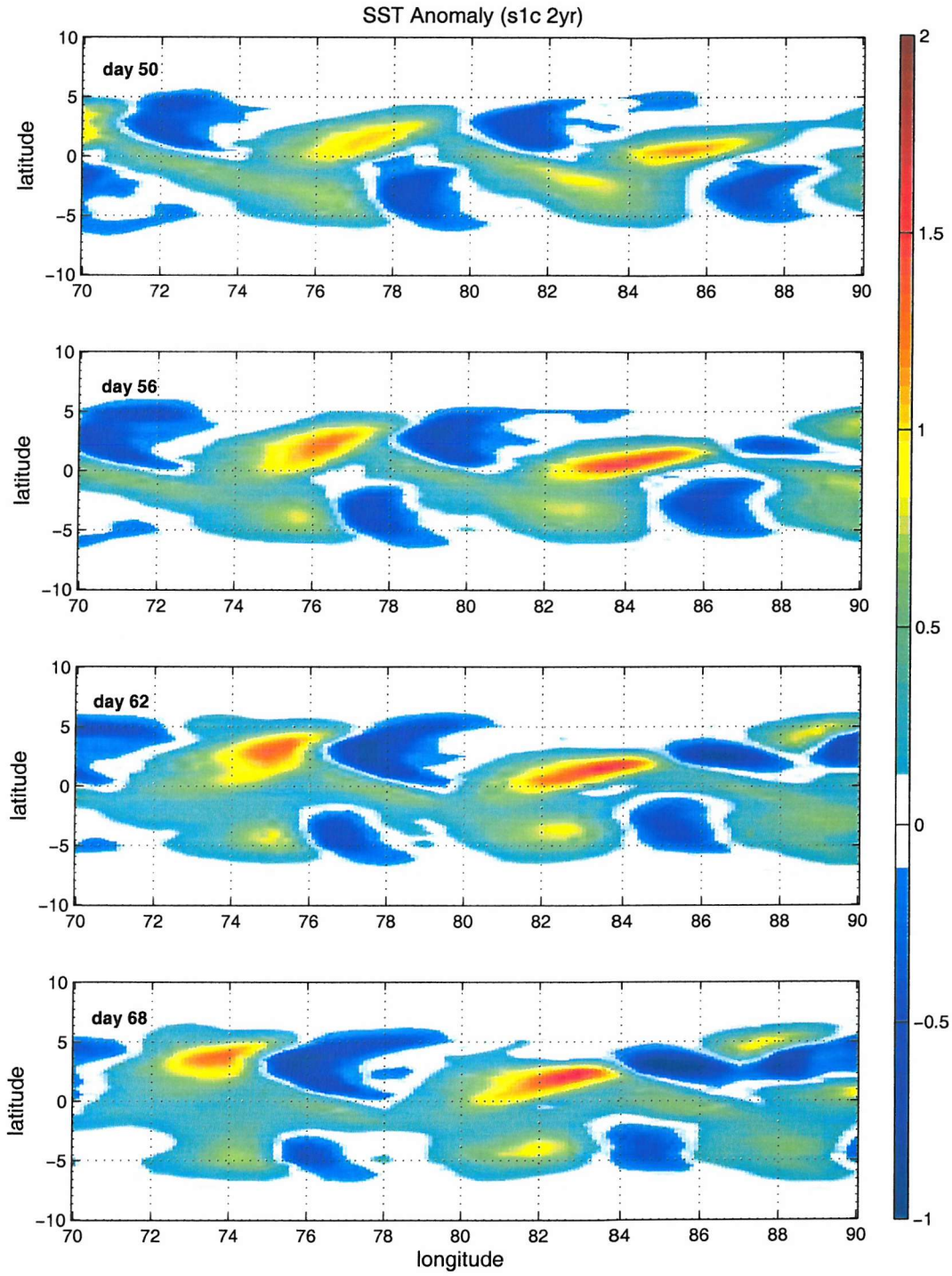

Figure 5.13: Snapshots every six days of SST anomalies generated by a Kelvin wave propagating away from a WWE as in Figure 5.12, though focusing on the period from day 50 to 68 between 70° and 90° longitude showing the slow westward-propagating SST anomalies (s1c 2yr).

generated by the Kelvin wave slowly propagate westwards. This is resolved in Figure 5.13 that is a magnification of a region in Figure 5.12, with snapshots every six days from day 50 to 68, focusing on the region 70° and 90° longitude. The propagating features are clearest in the central, eastern part of the basin, where there is a background TIW field present, suggesting that the coherent SST features are associated with the background TIW field.

The generation of these anomalies depends on the time of the year of the WWE perturbation, in relation to the seasonal cycle of the background TIW field. The amplitude of the anomalies are modulated according to whether the Kelvin wave is propagating through an active TIW period or the quiescent period, with weaker anomalies occurring during a weaker TIW field. Figure 5.14 shows a hovmöller plot of the SST anomalies generated by the WWE-forced Kelvin wave as it propagates eastward along the Equator during different times of year 11. The westward component in the anomaly field is present east of 60° longitude, throughout the TIW region, as was observed by Harrison and Giese (1988). This interaction is sensitive to the seasonal variability of the TIW field and the SST anomaly features are absent or weaker during periods of weaker TIW activity, in the quiescent period in spring, and stronger in the early part of the year and later in summer-autumn. The warming that occurs in the far eastern basin is associated with the Rossby wave formed by the reflection of the Kelvin wave at the eastern boundary. The warming that occurs immediately east of the WWE site is the result of the eastward advection of surface water by the formation of a Yoshida surface jet. The westward propagating Rossby wave generated by the WWE also leads to a slight perturbation of the SST field.

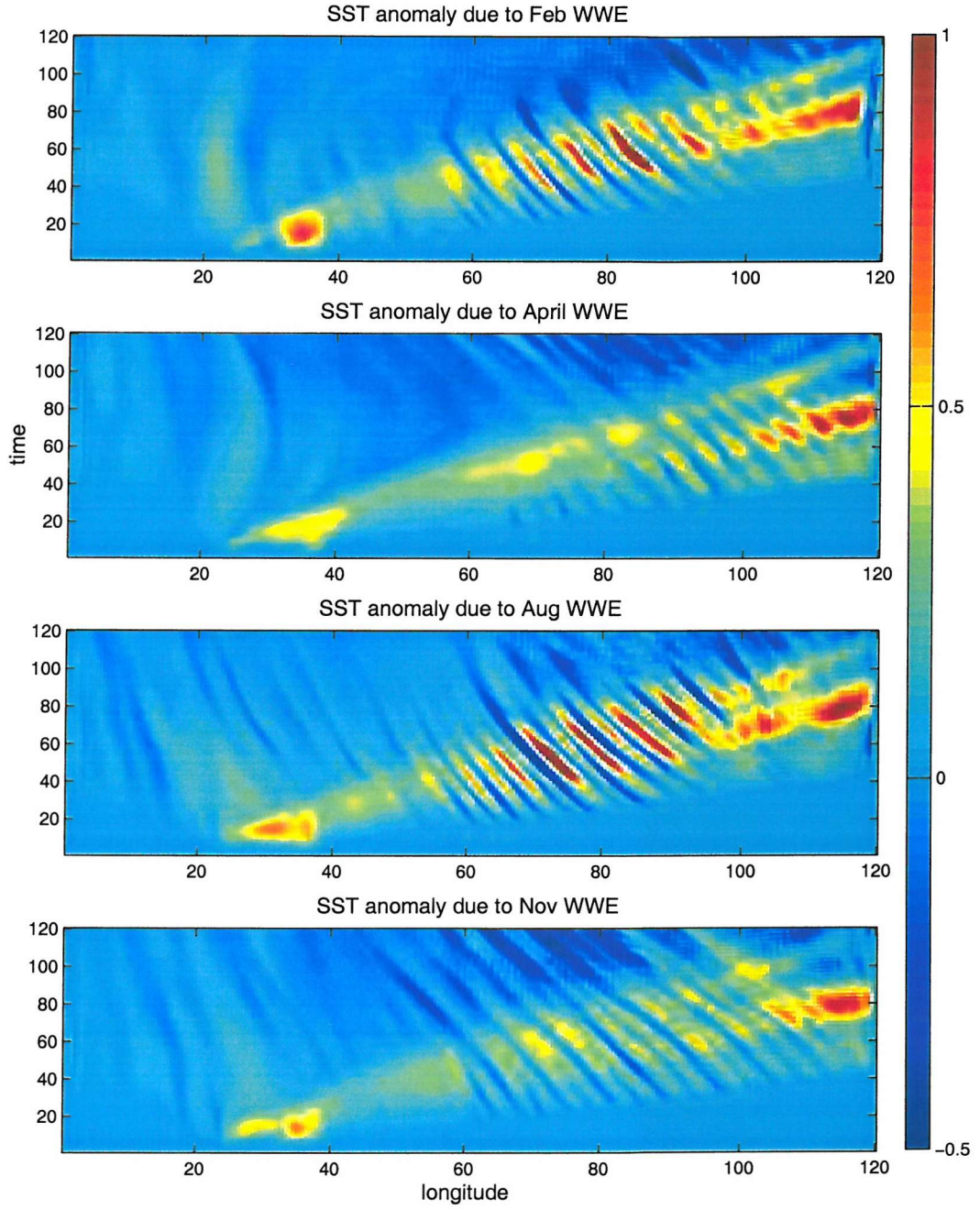

Figure 5.14: SST (°C) anomaly along the Equator for after a WWE generated in February, April, August, and November of year 11 of the standard configuration (iso 2yr).

5.3.1 Mixing Sensitivity

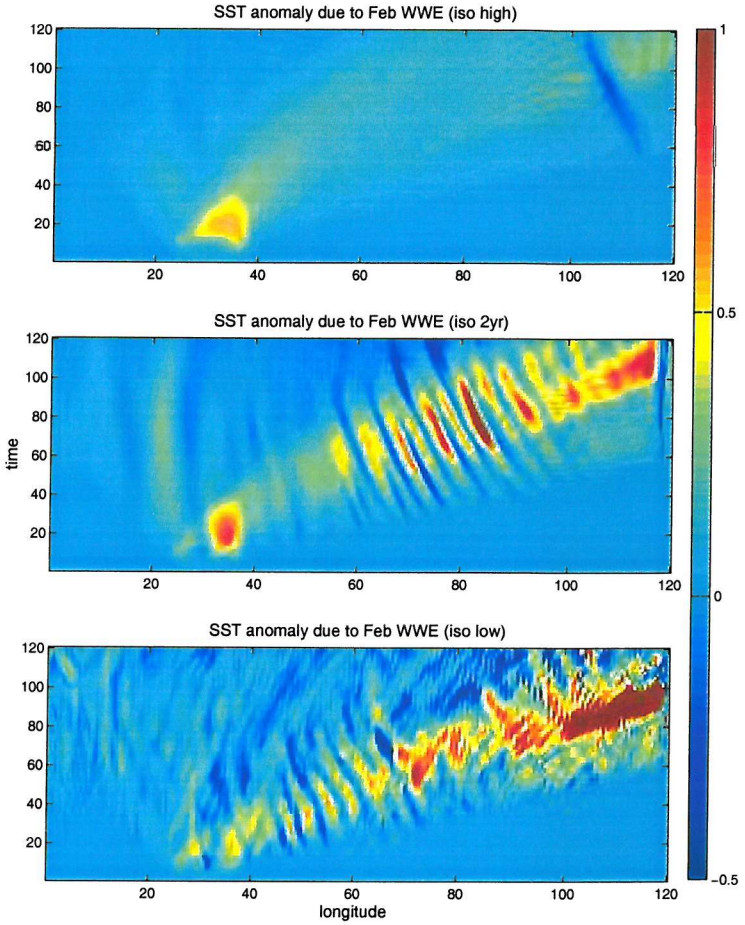

Figure 5.15: SST (°C) anomaly along the Equator for after a WWE generated in February for different horizontal mixing regimes (iso high, 2yr, low).

Figure 5.15 shows the temporal evolution of the Equatorial SST perturbations generated by a WWE that occurs at the beginning of February for the high, standard and low viscosity regimes. The TIW field is completely damped out in the high viscosity case, in the top panel of Figure 5.15, so that the WWE-forced Kelvin wave propagating through these conditions does not generate strong SST anomalies in the region that would otherwise have TIW activity. The westward propagating Rossby wave formed by the reflection of the Kelvin wave is clearly visible in the absence of other westward propagating anomalies. In the standard and low viscosity cases, SST anomalies are generated in the central, eastern basin. The structure in the low viscosity case is, however, less coherent and more chaotic than the standard case, as is the background TIW field itself.

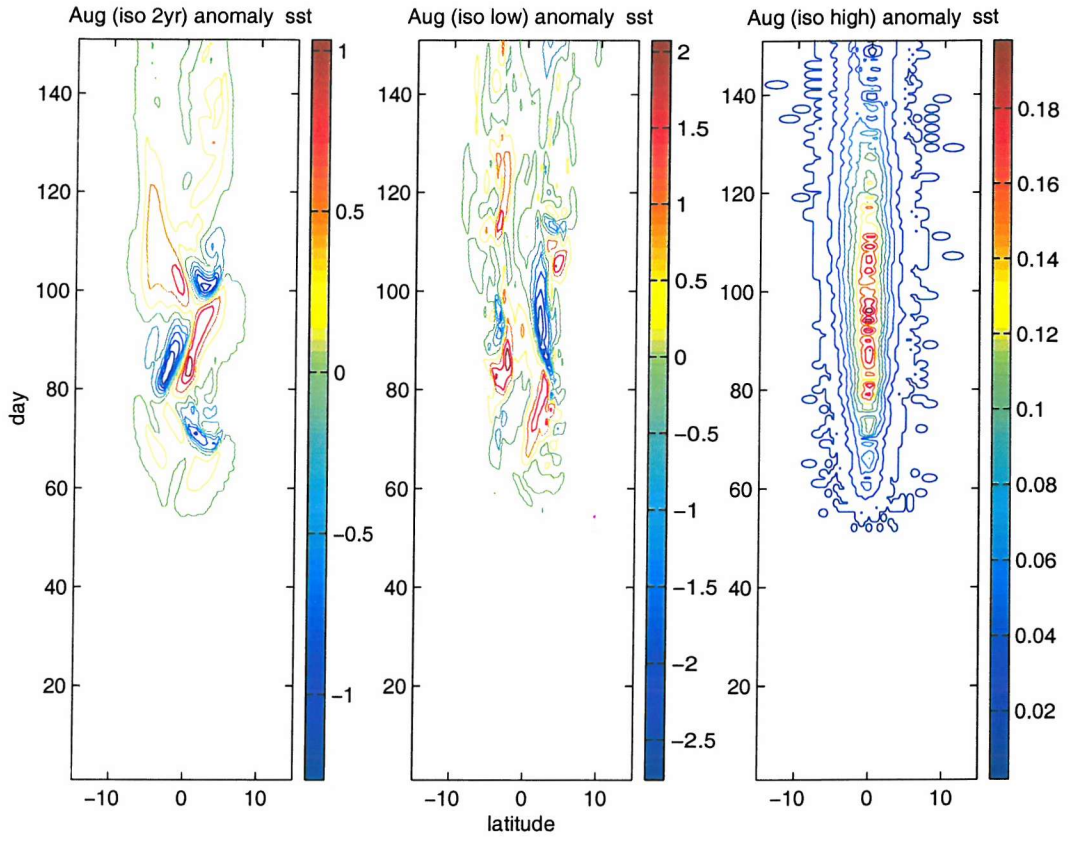

Figure 5.16: Temporal section from 15°S to 15°N at 80° longitude starting from August, showing SST anomalies generated by a Kelvin wave propagating through different isopycnal mixing regimes (iso 2yr, low and high).

The SST perturbations generated by the Kelvin wave forced by a WWE in August as it enters the region of TIW activity can be seen in Figure 5.16. The SST anomaly timeseries is from a meridional section from 15°S to 15°N at 80° longitude for the different mixing regimes. Positive and negative anomalies occur in the standard and low viscosity configurations within 5° either side of the Equator. The low viscosity case has stronger SST anomalies, with anomalies double in magnitude compared to the standard configuration, reaching 2°C. The high viscosity case, with no TIW field regime, has only a warm SST anomaly response to the propagating Kelvin wave, reaching a maximum of 0.2°C, that is centred at the Equator and persists for about a month.

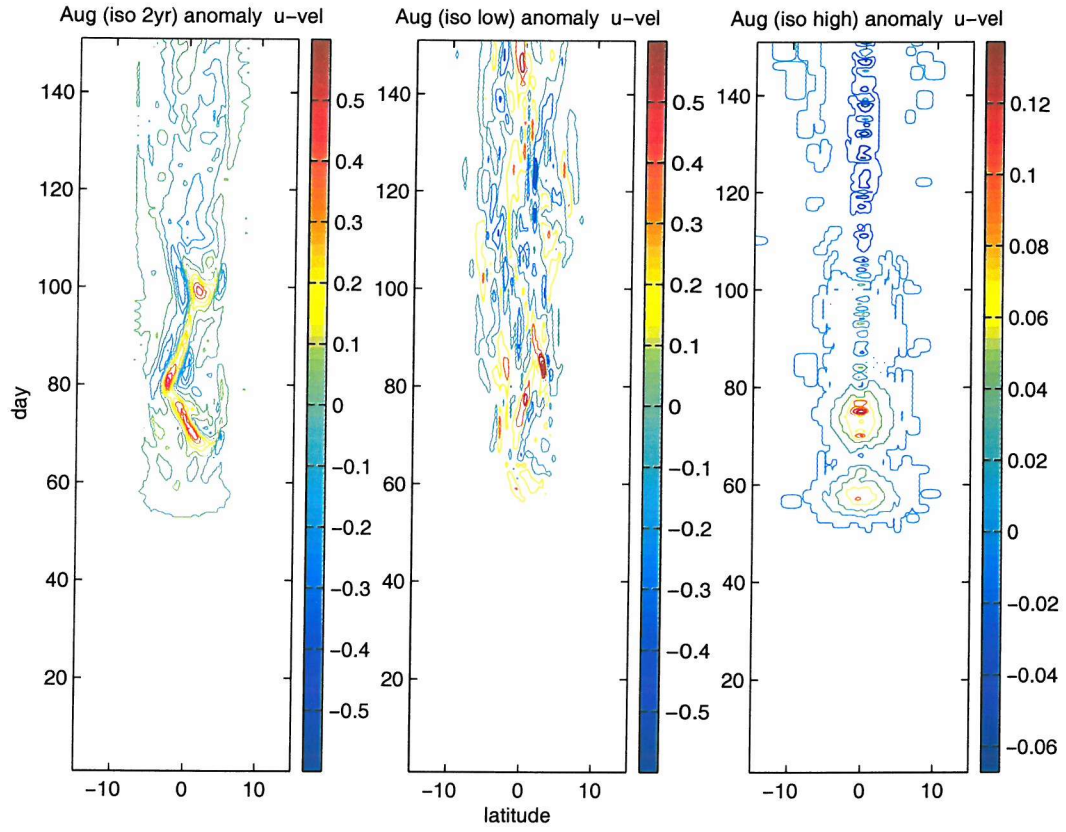

Figure 5.17: Temporal section from 15°S to 15°N at 80° longitude starting from August, showing surface zonal velocity anomalies generated by a Kelvin wave propagating through different isopycnal mixing regimes (iso 2yr, low and high).

Figure 5.17 shows the temporal evolution of the surface zonal velocity anomaly across the same meridional section. The anomalies generated in the standard and the low viscosity cases are of the same order of magnitude, reaching $\pm 0.5 \mathrm{ms}^{-1}$. For the high viscosity case, the zonal velocity anomalies are much weaker, only reaching around $0.1 \mathrm{ms}^{-1}$. They are predominantly eastward and two maxima are visible, one occurring just before 60 days since the WWE and the other after 70 days, both centred at the Equator. These are identified as the the zonal velocity signatures of the first and second baroclinic modes of the Kelvin wave, as will be described later in Chapter 6.

Figure 5.18 shows that surface meridional velocity anomalies are also generated by the WWE-forced Kelvin wave. Anomalies of $\pm 0.4 \text{ms}^{-1}$ are generated, which are of a similar magnitude to meridional velocities related to the TIW field. The structure of the meridional velocity anomalies in a low viscosity regime becomes more erratic, as does the background TIW meridional velocity field itself. In the high viscosity case the meridional velocity anomalies are much weaker, only reaching 0.015ms^{-1}. The background TIW field is absent in this regime so the anomalies present are not due to the interaction process present in the other two configurations. This leads to the conclusion that the velocity and SST anomalies present in the other configurations can be attributed to the presence of a background TIW field and the interaction of the wind generated Kelvin wave with these instability waves.

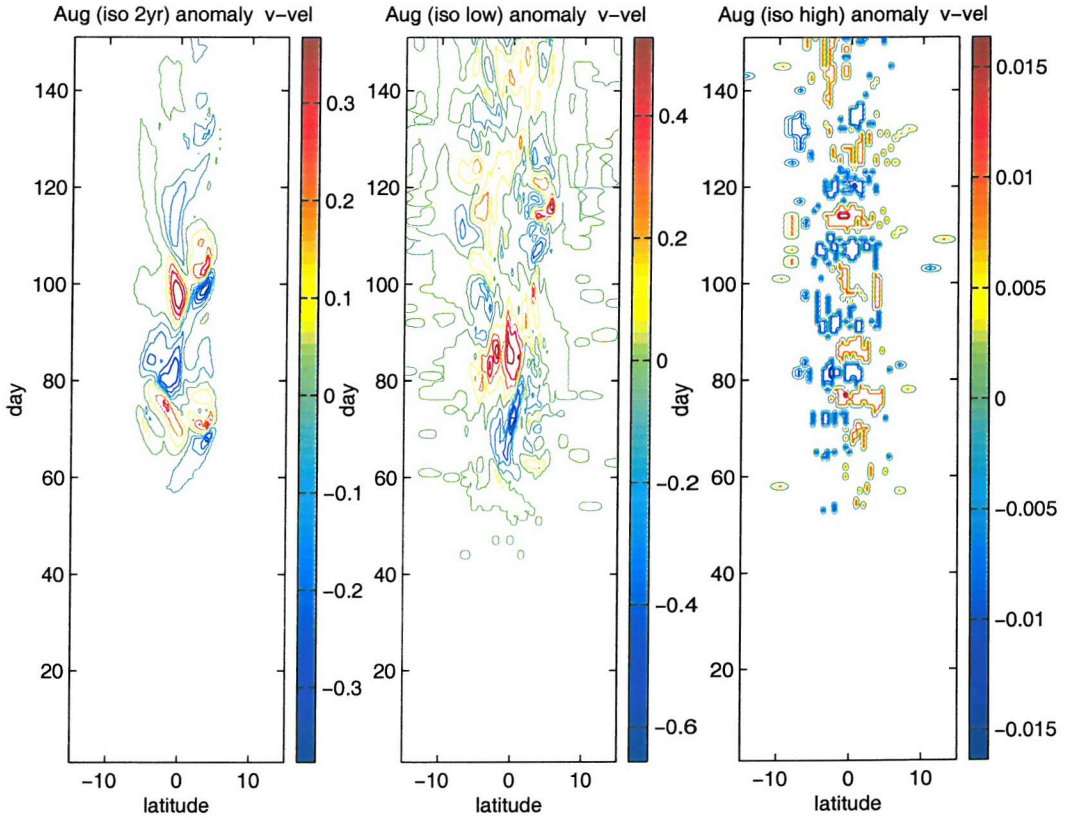

Figure 5.18: Temporal section from 15°S to 15°N at 80° longitude starting from August, showing surface meridional velocity anomalies generated by a Kelvin wave propagating through different isopycnal mixing regimes (iso 2yr, low and high).

A cross correlation analysis of the instantaneous meridional velocity from 15°S to 15°N across 80° longitude from day 60 to 120 of the control run and the perturbed WWE runs was carried out. We find that the perturbed surface meridional velocity field is lagged behind the unperturbed field. The anomalies in the standard and low viscosity configurations are therefore the result of a phase shift in the TIW caused by the Kelvin wave, not a change in amplitude. The TIW field in the standard configuration lags by 3 days, and in the low viscosity case by 1 day.

5.3.2 Sensitivity to Wind Stress Regimes

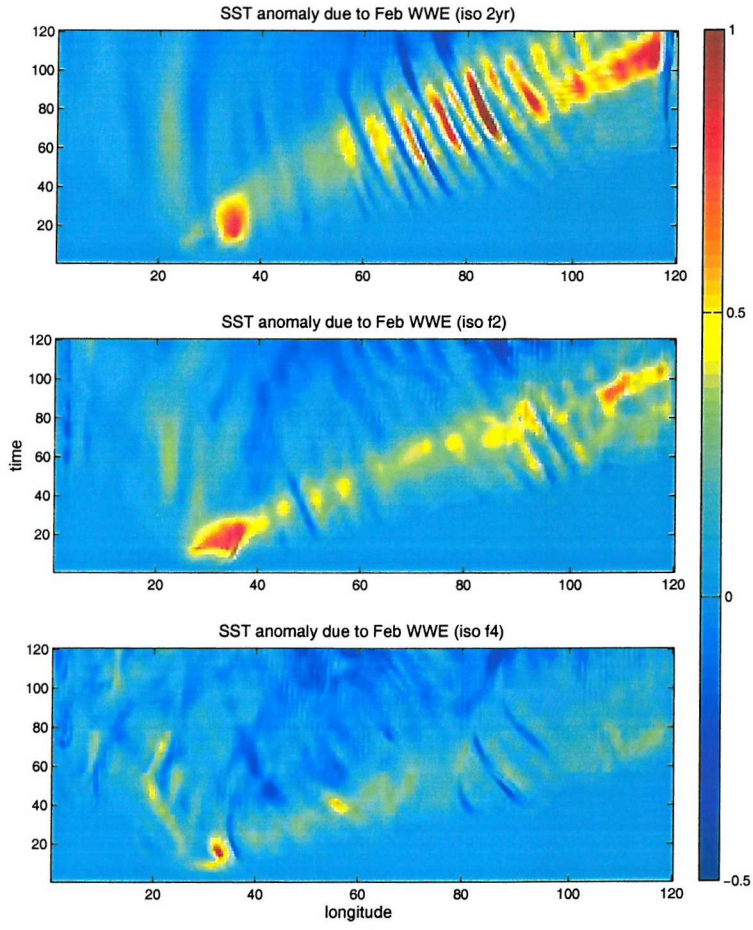

Figure 5.19: SST (°C) anomaly along the Equator for after a WWE generated in February where the background wind stress is successively doubled (iso 2yr, f2, f4).

The SST anomalies generated by a February WWE in different background wind stress regimes are shown in hovmöller plots along the Equator in Figure 5.19. The SST anomaly decreases as the background wind stress increases. This is despite the increase in the TIW activity described in the first half of this chapter. There is also a reduction in the presence of westward propagating structures as wind stress increases. The thermocline gradient increases with wind stress, though the Kelvin wave propagates to the eastern boundary in each case. Chapter 6 will discuss the reason why there is a weaker surface signal when there is a stronger background wind stress and steeper thermocline gradient. The timeseries of meridional velocity anomalies across a section at 80° longitude generated by a Kelvin wave forced by an August WWE propagating through different wind stress regimes are shown in Figure 5.20. Weaker anomalies are generated in the successively stronger wind stress conditions. Cross correlation of the control and unperturbed meridional velocity from 15°S to 15°N across 80° longitude from day 60 to 120 has shown that there is

a decrease in the phase lag of the background TIW field as the background wind stress increases, with a lag of under 0.5 days in the f4 configuration

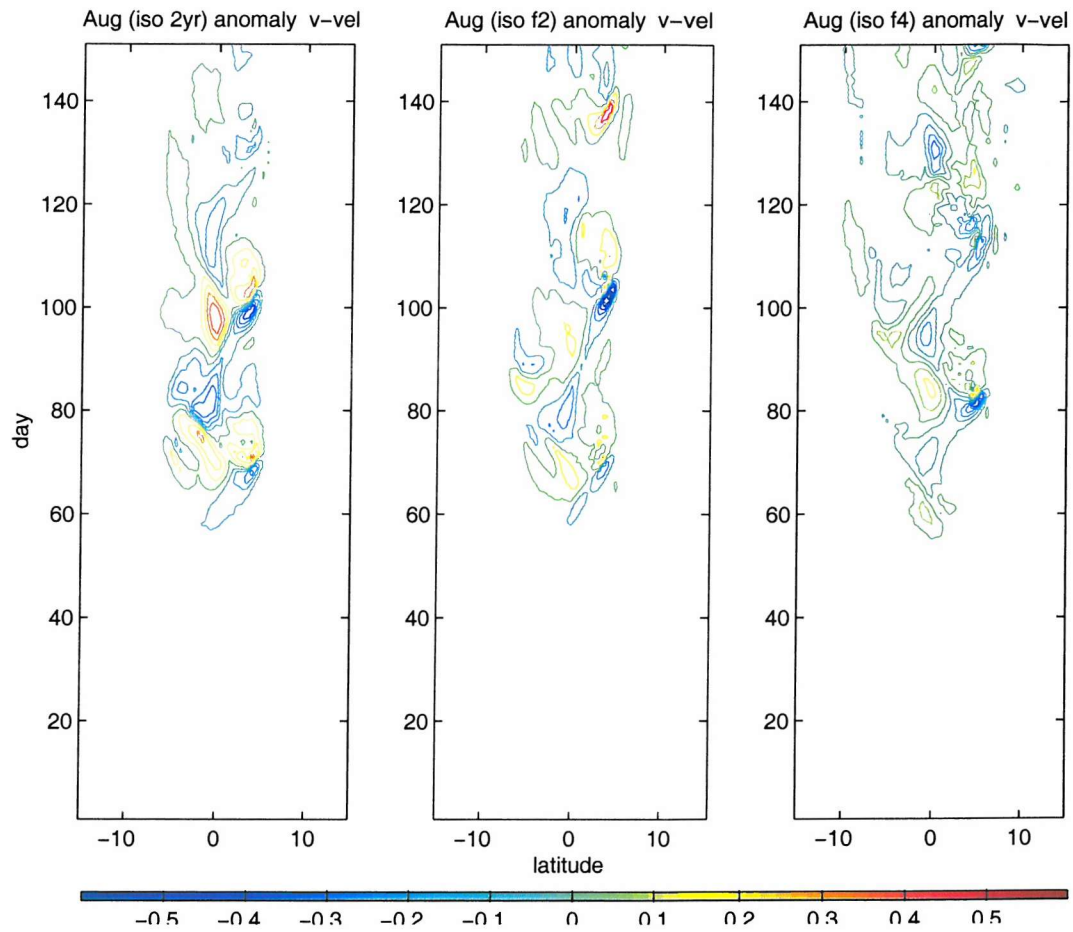

Figure 5.20: Temporal section from 15°S to 15°N at 80° longitude starting from August, showing meridional velocity anomalies generated by a Kelvin wave propagating through different wind stress regimes (iso 2yr, f2 and f4).

5.3.3 Kinetic Energy Analysis Revisited

Cross correlation results have shown that the TIW field that is perturbed by a WWE-forced Kelvin wave lags behind the control field. This suggests that the Kelvin wave only leads to a phase change of the background field that results in westward propagating SST and velocity anomalies. The Kinetic Energy (KE) analysis described in Chapter 4 has been revisited in order to examine in more detail the Kelvin wave-induced perturbation of the background TIW field to examine whether the Kelvin wave leads in an increase in instability. If an overall increase in eddy KE had occurred, it would have indicated an additional source of eddy activity, hence a new source of instability. The analysis was repeated, as before, along sections taken at 80°longitude, calculating the depth integrated mean and eddy KE terms over the top 200m. The analysis was performed over the three months following the WWE forcing, when the anomalies related to the ocean adjustment are greatest, and the results compared to the perturbation-free control run. The analysis was carried out for the response to the August WWE to study the interaction of the oncoming Kelvin wave with the most active period of the background TIW field. However, there was no clear trend in the results that indicated an increase in eddy KE as the Kelvin wave propagated through the background TIW field.and the results have proved inconclusive.

A more thorough analysis of the eddy KE equation could have been carried out, following Masina and Philander (1999); Masina et al. (1999). The calculation of the time mean conversion of eddy PE to eddy KE, the baroclinic conversion term (-g$\overline{\rho' w'}$), and of the mean KE to eddy KE, the barotropic conversion term ($-\rho(-\overline{u'v'}(\delta\bar{u}/\delta y))$), would have determined whether the Kelvin wave led to a source of instability. This was not carried out due to a limit in the available time and, in particular, due to the difficulty in treating divergence in a localised region of the domain. This would also be a problem if the whole model domain was used for the calculation due to the open north and south boundaries. Nonetheless, this type of analysis could have provided more information on the energetics of the interaction between the WWE-forced Kelvin wave and the background TIW field as weak changes in the instability wave field could have been detected more accurately, as well as determining the source of the instability.

5.4 Summary

The idealised Equatorial model ocean of the standard (iso 2yr) configuration, which has a 0.5°x0.5° resolution and a lateral viscosity of $10^3 m^2 s^{-1}$, generates a TIW field with a period that varies between 16 and 32 days. The seasonality of the TIW field compares well with observations, with a quiescent phase separating the boreal late winter, early spring and the summer-autumn active phases. The TIW field is important for redistributing momentum and for transporting heat equatorward, as well as being a source of energy for the deep ocean, with internal Rossby-gravity and Rossby waves propagating vertically to the ocean bottom.

The model TIW field is sensitive to changes in lateral mixing. A high viscosity regime does not generate a TIW field at all, while a low viscosity regime has a TIW field that is more chaotic in structure and exhibits greater variability in period than the standard configuration, losing the quiescent phase in the boreal spring. While the dominant source of instability in the standard configuration is around 5°N, reducing viscosity leads to an increase in instability at the Equator. This agrees with previous results that suggest this occurs due to an increase in the barotropic conversion of energy at the Equator (Pezzi and Richards, 2003). Gradually increasing the background wind stress leads to an increase in the westward extent of the TIW field, reducing the mean Warm Pool temperature maximum due to the increase in mesoscale mixing. The seasonality originating from the background wind forcing is lost, with TIWs occurring throughout the year. Though the variance of the period increases as the background wind stress is increased, the increase that occurs in a low viscosity regime is greater.

A Kelvin wave generated by a WWE interacts with the background TIW field as it propagates through the central and eastern basin. In the high viscosity configuration, where the background TIW field is damped out all together, the Kelvin wave only leads to a weak surface velocity and temperature signature associated with the propagating baroclinic Kelvin modes. For all the other configurations, where there is an active TIW field, cross correlation has shown that the Kelvin wave leads to velocity and SST anomalies resulting from a phase shift of the TIW field that are strongest in the low viscosity regime. When the TIW field is damped out in the high viscosity regime, there is no such SST anomaly generated. Increasing the strength of the background wind field however leads to a weaker interaction between the Kelvin wave and the TIWs. An analysis of the eddy KE during the period of interaction between the Kelvin wave and the TIW field has not determined whether the Kelvin wave leads to an additional perturbation of the instability field. We can only con-

clude that the Kelvin wave leads to a phase shift of the existing TIWs, with a lag of up to three days compared to the unperturbed TIW field. There was no increase in TIW amplitude resulting from the presence of the Kelvin wave, as expected by Giese and Harrison (1990).

Chapter 6

The Kelvin Wave Adjustment

6.1 Introduction

Gill (1983) modelled the response of the Equatorial Pacific Ocean to changes in wind stress with a simple linear reduced-gravity model and found that the sea level and surface current anomalies of the 1972 El Niño could be decomposed into a cumulative contribution of equatorially-trapped Kelvin and Rossby waves. Studies using GEOSAT altimeter-derived sea level and surface current anomalies of the 1986-89 period confirmed the role of equatorial waves in basin-wide adjustments. Delcroix et al. (1994) found that 71% of the total variance of the surface geostrophic zonal current anomalies within 4°N and 4°S can be accounted for by the first baroclinic Kelvin mode and the first meridional Rossby mode. Second and third Rossby modes propagating at theoretical phase speeds have also been identified during the 1992-93 El Niño using TOPEX/POSEIDON altimetry data and TOGA/TAO array measurements (Boulanger and Menkes, 1995). Modelling results of an OGCM integration over the 1985-94 TOGA period have also shown that the wind field generates long equatorial waves on interannual timescales (Boulanger et al., 1997) and the wind field within 2°N and 2°S was successfully reconstructed using only first Kelvin and Rossby mode variability in the ocean surface velocity field.

Observations have shown that wind forcing is the main mechanism generating waves propagating away from the western boundary (Boulanger and Menkes, 1995). Analysis of GEOSAT data also led to the conclusion that wind forcing is more important in the generation of equatorial waves near the western boundary, and not reflection of incoming waves (Picaut and Delcroix, 1995). Boulanger et al. (2003) found that though reflection is 80-90% efficient at the western boundary, the wind contribution in the Western Pacific dominates Kelvin wave variance.

When the upper ocean is forced with a stationary wind patch, Kelvin and Rossby waves radiate away from the forced region according to linear theory, where the ocean response is the sum of equatorial waves (Giese and Harrison, 1990, 1991). By increasing the strength of the wind forcing the amplitude of the lower baroclinic modes increases while that of the higher modes decreases. This is the result of non-linear interactions between the wind forcing and the background ocean state that is modulated by the EUC, a sloping thermocline and instability waves (Giese and Harrison, 1990).

Kelvin wave dynamics are studied by modelling the adjustment process to forcing by a Westerly Wind Event. Various techniques are available for studying the changing characteristics of a Kelvin wave during its propagation along the Equator. Long and Chang (1990) used multiple scale analysis and other workers have performed modal decomposition of the wave properties (Gill, 1985; Benestad et al., 2002). Here we analyse the modal structure of the Equatorial wave adjustment along the whole equator, as well as looking in more detail at the Kelvin wave structure at 80° longitude, in the eastern basin.

6.2 Equatorial Waves

The are three solutions of the equations of motion for waves trapped at the Equator, with the equatorial Rossby radius setting the width scale for the equatorial waveguide. Figure 6.1 shows the dispersion relation for each solution; the first two gravity wave modes (green), the first two Rossby wave modes (blue), and the mixed Rossby-gravity, or Yanai, wave (yellow). If the meridional velocity is zero, we also reach a solution for the Kelvin wave (red).

The Coriolis component of the shallow water equations disappears at the Equator so that the relation between frequency and the meridional wave number (l) in the dispersion relation of Equatorial waves is dependant on latitude. The meridional wavenumber goes to zero at a certain latitude and becomes imaginary, leading to spatial decay. The waves are therefore trapped within an 'Equatorial waveguide' so that energy can only disperse in the zonal direction and not in the meridional direction. The meridional spatial decay scale is given by the Equatorial Rossby radius of deformation (Gill and Clarke, 1974) given by

$$a_e = (c/2\beta)^{\frac{1}{2}} \tag{6.1}$$

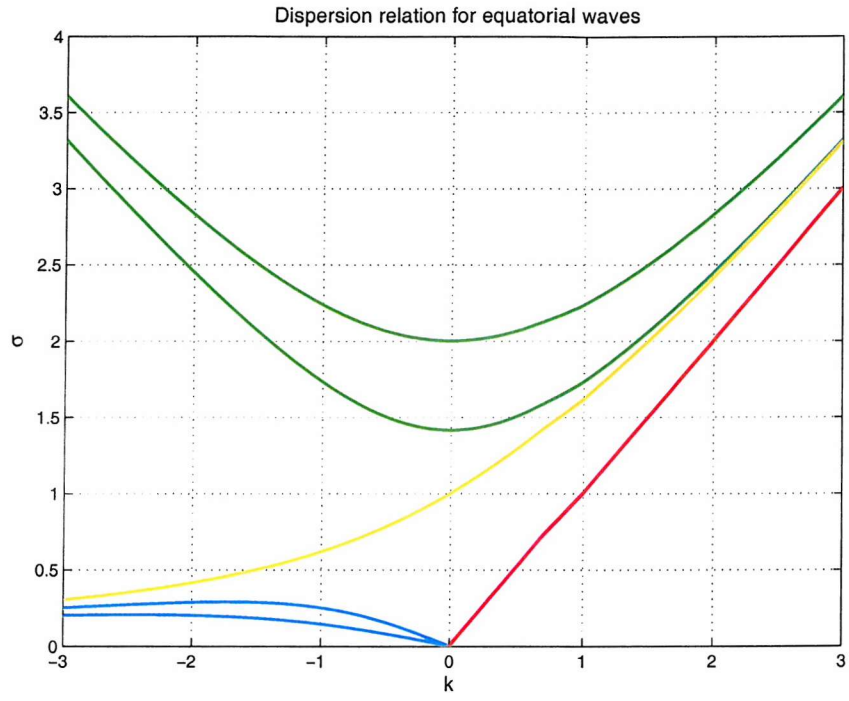

Figure 6.1: Dispersion relation for equatorial waves, where red is the Kelvin wave, yellow the mixed Rossby-gravity wave, green the first two gravity wave modes and blue the first two Rossby wave modes. Units of frequency (σ) are $(2\beta c)^{\frac{1}{2}}$ and those of zonal wavenumber (k) are $(2\beta/c)^{\frac{1}{2}}$.

where c is the phase speed ($c = \sqrt{gh}$) and β is the meridional gradient of the Coriolis parameter.

6.2.1 Kelvin Waves

The Kelvin wave is considered using the linearised shallow water equations on a β-plane, assuming hydrostatic motion, the Boussinesq approximation and a flat bottom (Gill, 1982), as shown by

$$u_t - \beta y v = -g\eta_x \tag{6.2}$$

$$v_t + \beta y u = -g\eta_y \tag{6.3}$$

$$\eta_t + h\Big(u_x + v_y\Big) = 0 \tag{6.4}$$

h is the depth of the layer being considered. The meridional velocity component is not included as this is absent in a linear Kelvin wave. The equations are thus reduced to

$$u_t = -g\eta_x \tag{6.5}$$
$$\beta y u = -g\eta_y \tag{6.6}$$
$$\eta_t + hu_x = 0 \tag{6.7}$$

The surface elevation, η is removed between equations 6.5 and 6.6 to give the one dimensional wave equation,

$$u_{tt} - ghu_{xx} = 0 \tag{6.8}$$

whose general solution consists of two waves travelling zonally in opposite directions. Only the eastward propagating solution is physically valid as the other grows exponentially away from the equator. The solution for an infinite train of Kelvin waves (Gill, 1982) is given by

$$\eta_{Kelvin} = e^{-\beta y^2/2c} F(x - ct) \tag{6.9}$$
$$u_{Kelvin} = (c/g) e^{-\beta y^2/2c} F(x - ct) \tag{6.10}$$
$$v_{Kelvin} = 0 \tag{6.11}$$

where F is an arbitrary function. The Kelvin wave is non-dispersive and propagates eastward with the same phase speed as in the absence of rotation. The meridional structure of the Kelvin wave is a Gaussian and the zonal velocity field is in geostrophic balance with the pressure field, as seen in equation 6.5. The dispersion relation for a Kelvin wave is linear

$$\omega = kc \tag{6.12}$$

where ω is frequency, k is the zonal wavenumber.

6.2.2 Rossby Waves

The unperturbed potential vorticity field of the Earth is not constant but varies with latitude. This leads to occurrence of Rossby, or planetary, waves that are trapped at the Equator due to the vanishing Coriolis force. The dispersion relation for Equatorially-trapped Rossby waves (Gill, 1982) is given by

$$\omega = -\beta k/(k^2 + (2n+1)\beta/c) \tag{6.13}$$

Long waves ($k \rightarrow 0$) propagate westward and are approximately non-dispersive. Short waves ($k \rightarrow \infty$) are dispersive and the group velocity is eastward, opposite to the phase velocity.

6.3 The Eigenvalue Problem

If the shallow water equations are considered, assuming a flat ocean bottom, that the fluid is hydrostatic and the Boussinesq approximation is valid, then separation of variables technique can be applied (Gill and Clarke, 1974; Gill, 1982). The problem is reduced to considering only variations in the horizontal by expanding the components of the momentum equations onto a sum of normal modes. Zonal velocity, for example, can be expanded as

$$u = \sum \tilde{U}_n(x,y,t)\hat{u}_n(z) \tag{6.14}$$

where $\tilde{U}_n$ is the temporal horizontal function of each mode (n) and $\hat{u}_n$ the eigenfunction of each mode that satisfies a vertical Strum-Liouville eigenvalue problem for an ocean of constant depth H with no mean flow, which can be solved as

$$\hat{u}_{zz} + \left(\frac{N}{c_i}\right)^2 \hat{u} = 0 \tag{6.15}$$

where N^2 is the Brunt-Väisälä frequency and c_i is the internal mode phase speed of long gravity waves. The eigenvalue problem is solved with the condition that the rigid lid approximation is made so that $\hat{u}$ goes to zero at the surface (z = 0) as well as at the ocean bottom (z = -H), and since the eigenfunctions of the Strum-Liouville problem are orthogonal, as shown by

$$\int_{-H}^{0} \hat{u}_m(z)\hat{u}_n(z)dz = 0 \tag{6.16}$$

if $m \neq n$. For an ocean of finite depth that is discretized into a series of levels (n), the solution will give zero to n modes. The barotropic mode $(n = 0)$ has a phase speed much greater than that considered here, resulting from the density difference across the sea surface being much greater than the density difference within the ocean. There is a series of baroclinic modes $(n = 1, n)$ that are ordered so that c_n decreases as n increases.

The eigenvalue problem in Equation 6.15 is solved in the form of the matrix $\mathbf{A}\hat{u} = \lambda\mathbf{B}\hat{u}$, where λ is the eigenvalue, as in Killworth et al. (1997) and Figure 6.2 shows the vertical structure of the first four baroclinic modes.

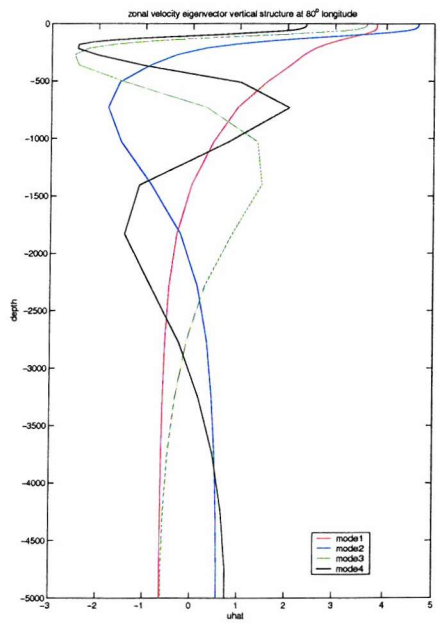

Figure 6.2: Vertical structure of the zonal velocity eigenvector at 80° longitude on the Equator day1 (s1c 2yr).

Modal analysis assumes a background density structure. The Equatorial Pacific has a spatially and temporally varying stratification that must be taken into account. The zonally varying stratification at the Equator is shown by the equatorial annual mean squared Brunt-Väisälä frequency in Figure 6.3. The decomposition of the zonal velocity anomaly is therefore computed here against the locally varying background control (unperturbed) density profile. If the analysis is repeated using a constant Brunt-Väisälä frequency (N^2=1) of $10^{-4}s^{-1}$ the dominant signal of the Kelvin wave is in the first baroclinic mode, with a much weaker second mode, compared to the results presented in Section 6.4. The phase speed does not change, though the amplitude weakens. The modal structure of the westward propagating Rossby wave also changes and there is a weaker signal imparted from the background

TIW field.

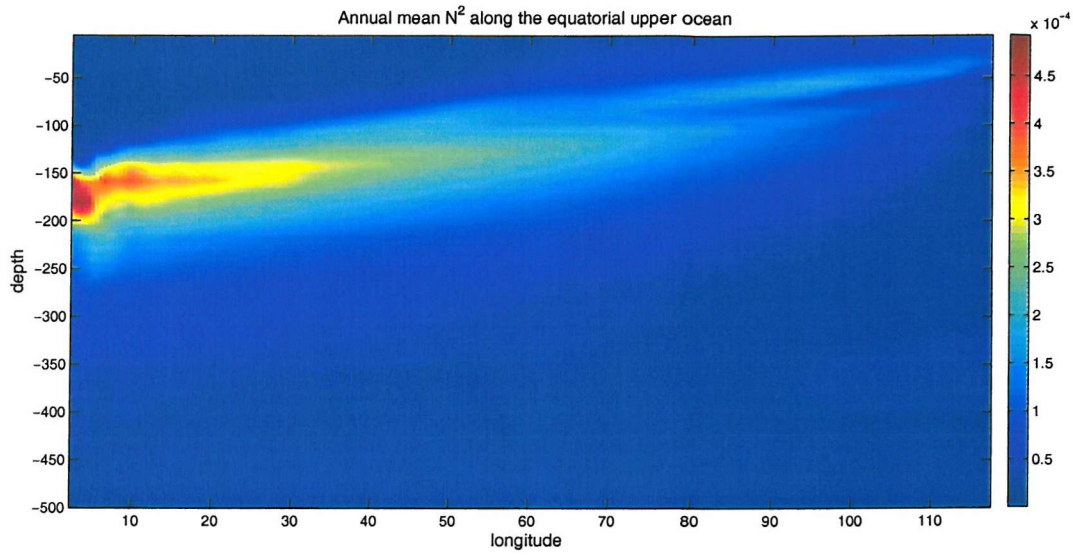

Figure 6.3: Annual mean squared Brunt-Väisälä frequency (s^{-1}) along the Equator over the upper 500m (s1c 2yr).

As we will see in Figure 6.5, the modal analysis is not 'clean' as signals related to all the modes are present in each panel and all four modes show variability after the arrival of the first mode, despite each mode propagating at a successively slower phase velocity. As the Kelvin wave predominantly projects onto the first two baroclinic modes, the discussion of the higher baroclinic modes is unreliable. The inaccuracy of the solution may result from the formulation of the problem. An assumption of no mean flow has been made and this may not be appropriate for the Equatorial region due to the strong zonal circulation. The unperturbed modes have been calculated in two different ways and the discrepancy between the results is of a 10% error. This is the result of finite differencing over a relatively poor vertical resolution of 31 levels. For the purpose of this study, the results produced for the first two modes are defined clearly enough for consideration.

6.4 Adjustment to a WWE in an Ocean GCM

A WWE located at the Equator, 30° longitude generates an upper ocean equatorial planetary wave adjustment, as shown in Figure 6.4. Both anomaly fields show an eastward propagating downwelling Kelvin wave and a weak signature produced by a westward propagating Rossby wave. The depth of the 20°C isotherm anomaly shows the Kelvin wave signal as a series of rays, though the signal ends where the 20°C isotherm shoals at the surface. The SST Kelvin wave signal demonstrates that the wave reaches the eastern boundary. The sensitivity of this structure to the background ocean state is studied in the following sections by projecting the Kelvin wave onto the baroclinic modes. The unperturbed modes are calculated first from the control density structure and then these are projected onto the zonal velocity anomalies generated by the WWE. This projection coefficient is plotted in the subsequent figures.

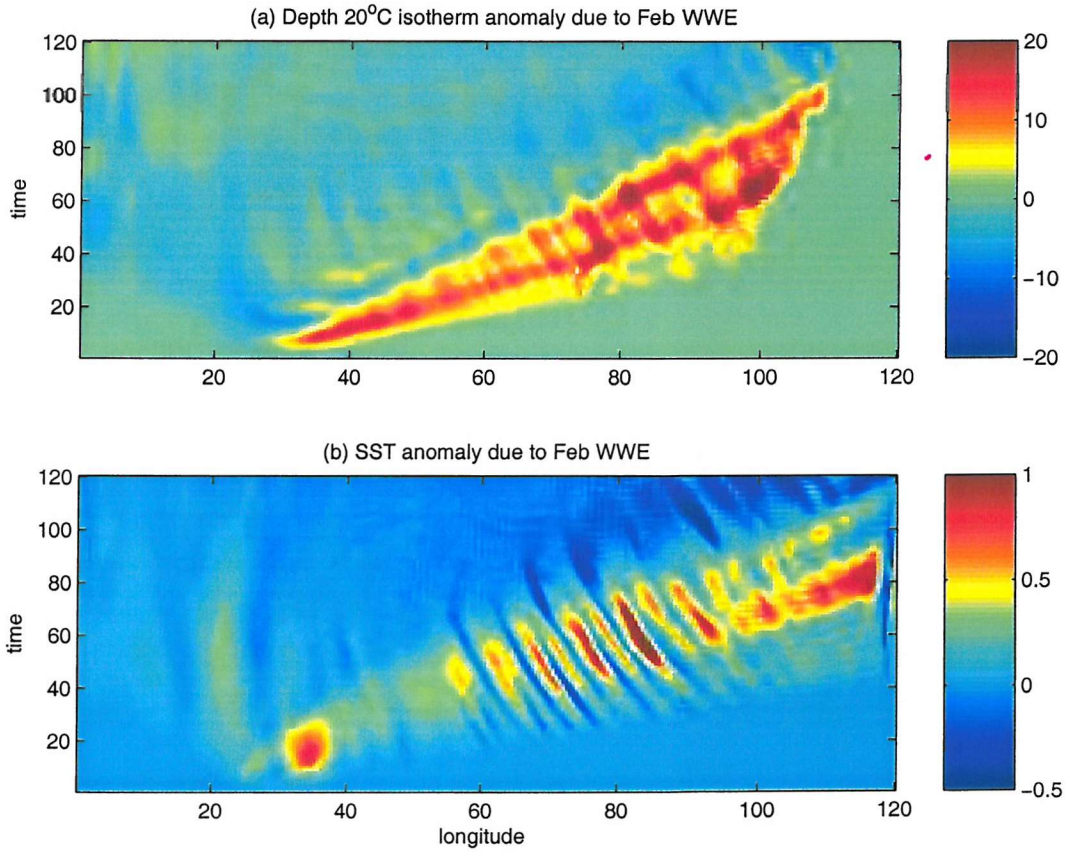

Figure 6.4: Hovmöller of depth of the 20°C isotherm and SST along the Equator for a WWE generated in February (s1c 2yr).

Figure 6.5 shows the projection onto vertical modes of the zonal velocity anomaly field along the Equator over 120 days following the occurrence of the WWE adjustment shown in Figure 6.4. The panels show the first, second, third and fourth baroclinic modes respectively. This modal decomposition gives an indication of the distribution of kinetic energy between the modes. The eastward propagating Kelvin wave signal is predominantly composed of the first and second modes. This is in agreement with previous findings, both observational (Eriksen et al., 1983; Lukas et al., 1984) and modelled (Busalacchi and Cane, 1985; Kessler and McPhaden, 1995), where the influence of the second baroclinic mode signal is comparable to that of the first baroclinic mode. These earlier studies found that the inclusion of the second mode, instead of just considering the first mode, improved the simulation of the overall interannual variability in the Pacific through its effect on the rate of propagation of wind-generated anomalies from the western part of the basin to the east.

Our results confirm that the second mode is an important component of the adjustment in this model and must be included to simulate the WWE forced adjustment. Other studies have generally reported that the first mode is the most important. The signature of the third and fourth is much weaker. Here we will focus mainly on the first two modes of the Kelvin wave due to the weak amplitude of the higher modes and the contamination of the higher modes by the dominant first and second modes. Busalacchi and Cane (1985) also found that the third and fourth modes were statistically negligible when considering their influence in the evolution of the sea level field.

The westward propagating Rossby wave is resolved in the first two modes, as is the Kelvin wave, and the whole domain is perturbed by the planetary wave adjustment. Strong, positive projection coefficient values result after the Kelvin wave has passed. These are westward propagating features that occur after the arrival of the Kelvin wave. The Kelvin wave signals are not damped as they propagate away from the WWE source, suggesting that these subsequent westward propagating perturbations could be the result of the mean state being perturbed by the Kelvin wave, instead of being related to the Kelvin wave itself.

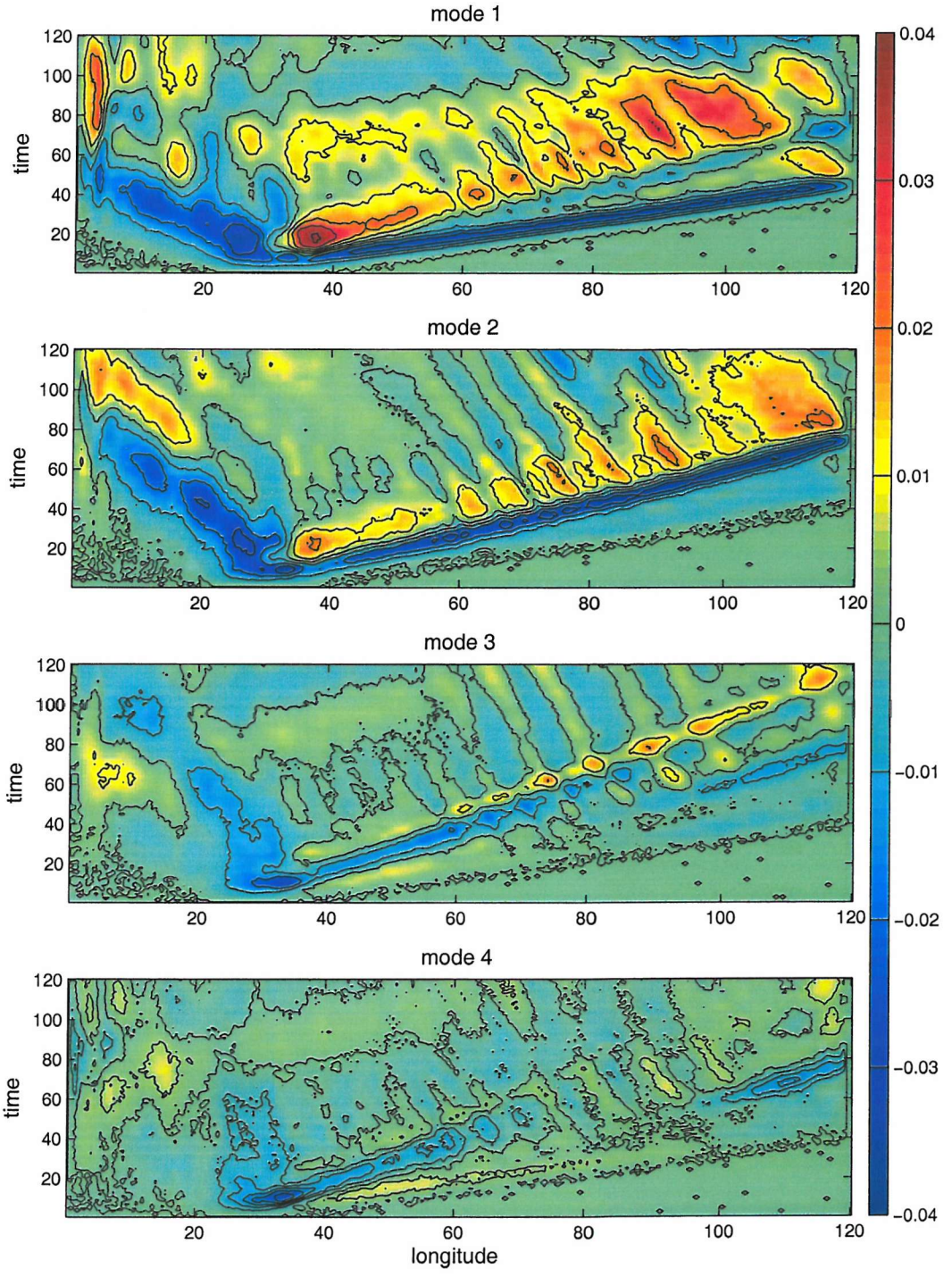

Figure 6.5: Projection of the zonal velocity anomaly onto the modal coefficient (ms^{-1}) for the first four baroclinic modes along the Equator for a February WWE (s1c 2yr).

If Figure 6.5 is compared with Figure 6.4 it becomes apparent that the anomalies generated in the depth of the 20°C isotherm and SST are mainly generated by the second and third modes.The first mode can be detected in the anomaly fields of Figure 6.4, though it does not lead to a strong perturbation of the depth of the 20°C isotherm and SST fields. We focus our attention on the first two modes as the third mode has a much weaker onto the velocity field used in the modal analysis, despite a strong thermocline signature. The amplitude of the first and second modes are of a similar magnitude in Figure 6.5. The westward propagating anomaly in the far eastern basin, mainly in the first and second modes, that occurs after the Kelvin wave has reached the eastern boundary is the result of the reflection of the Kelvin wave into a westward propagating Rossby wave. This coincides with the region of warm SST anomalies in the bottom panel of Figure 6.4.

Figure 6.6 shows the evolution of the first four modes and the vertical section of zonal velocity anomaly at 80° longitude on the Equator following a WWE in February. The dominant first two modes are plotted together in the top panel and the third and fourth modes in the second. The modes have been calculated by projecting the full depth velocity anomaly field, the top 500m of which is shown in the bottom panel. The Kelvin wave reaches 80° longitude after about 20 days. Both the first and second mode generate a subsurface zonal velocity anomaly maximum of $0.15ms^{-1}$. This is followed by a second subsurface anomaly maximum after another ten days also of $0.15ms^{-1}$. These maxima in zonal velocity are located at around 100m depth. The velocity anomalies close to the surface are the anomalies related to the perturbation of the TIW field, seen following an August WWE in the left panel of Figure 5.17. The third and fourth baroclinic modes are shown in the second panel of Figure 6.6. The third baroclinic mode is associated with a negative zonal velocity anomaly of $-0.2ms^{-1}$. The modal coefficient has a weak amplification 70 days after the WWE that corresponds to this velocity anomaly, though it is of the same magnitude as the level of variability of the signal generated by the first and second modes after the peak related to the Kelvin wave. There is no discernible signal in the fourth mode.

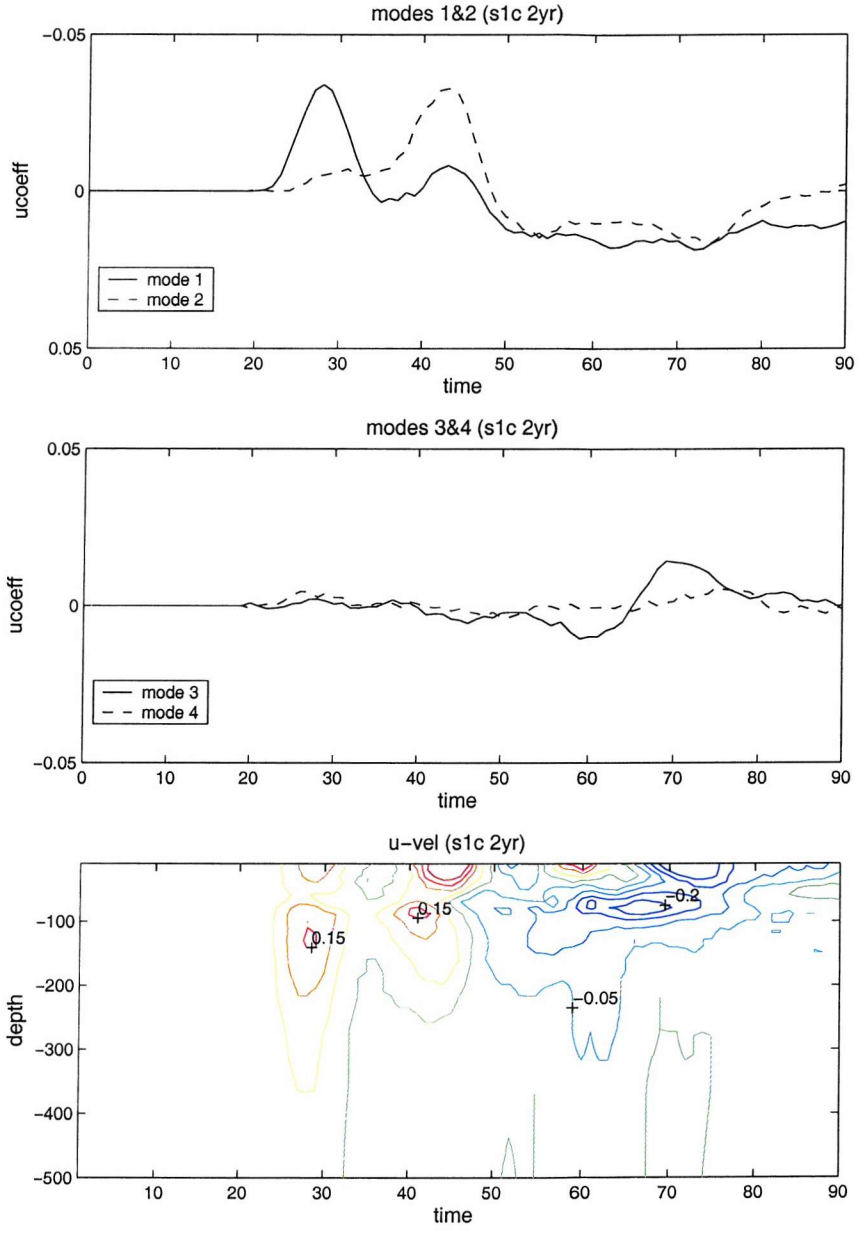

Figure 6.6: Modal analysis of zonal velocity anomaly and the zonal velocity anomaly field of a vertical section over the top 500m at 80° longitude on the Equator for a WWE generated in February (iso 2yr). The coefficient (ucoeff) is in units of ms^{-2} and the zonal velocity contour interval is $0.05ms^{-1}$.

6.4.1 Seasonal Variability

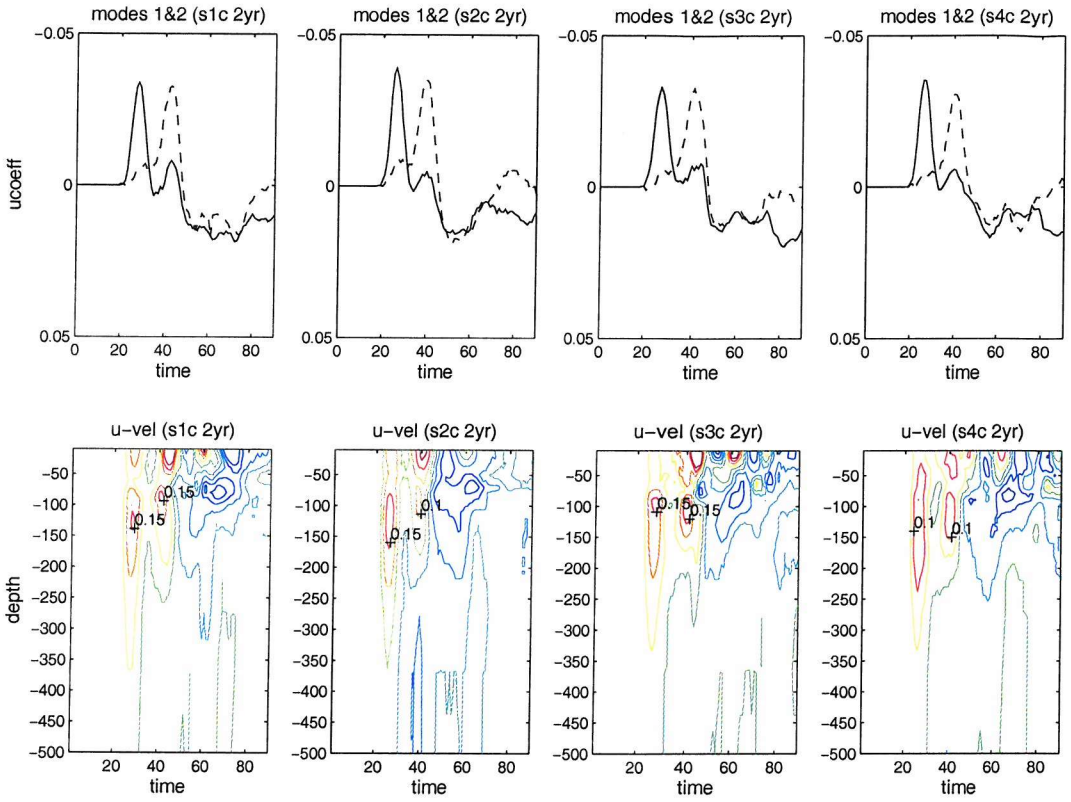

Figure 6.7: Modal analysis of zonal velocity anomaly and the zonal velocity anomaly field of a vertical section over the top 500m at 80° longitude on the Equator for a WWE generated in February, April, August and November (iso 2yr). The coefficient (ucoeff) is in units of ms^{-2} and the zonal velocity contour interval is $0.05ms^{-1}$.

The seasonal variability of the background wind field modulates the gradient of the thermocline along the Equator, as was shown previously in Figure 3.4. Four experiments are carried out with the standard configuration (iso 2yr) where the same WWE is applied at four different times of the year, one month preceeding the maxima and minima denoted by the vertical lines in Figure 3.4. The top panels of Figure 6.7 shows the projection of the zonal velocity anomaly onto the first and second baroclinic modes at 80° longitude at the Equator for each experiment. The temporal evolution of the vertical profile of the zonal velocity is shown for each case in the bottom panels.

The amplitude of the first and second baroclinic mode is comparable, as is shown in Table 6.1. The amplitude of the second mode relative to the first mode varies depending on the time of the year. The Kelvin wave generated by a February (s1c) and an August (s3c) WWE have an almost equal projection onto the first two modes. However, the amplitude of the second mode of the Kelvin wave generated by an

April (s2c) and a November (s4c) WWE is slightly weaker than that of the first mode. These differences are in accordance with the varying background conditions, with a weaker second mode when the thermocline is steeper. The zonal velocity anomaly field generated by the Kelvin wave exhibits the two subsurface maxima associated with the first two baroclinic modes. The maximum of the second mode is weaker when the projection is weaker, reaching only 1ms^{-1} in April and November, instead of the 1.5ms^{-1} maximum in February and August.

experiment	mode 1 ucoeff (10^{-2}ms^{-1})	mode 2 ucoeff (10^{-2}ms^{-1})
s1c (feb)	3.3	3.2
s2c (april)	3.9	3.5
s3c (aug)	3.3	3.3
s4c (nov)	3.5	3.1

Table 6.1: Amplitude of the first and second baroclinic modal coefficient (10^{-2}ms^{-1}) for a WWE generated in February, April, August and November (iso 2yr).

6.4.2 Sensitivity to Lateral Mixing

The Kelvin wave adjustment in isopycnal mixing configurations with different settings for the level of horizontal viscosity are compared. Figure 6.8 shows the projection onto the first two baroclinic modes of the zonal velocity anomaly along the Equator for the high ($10^4\text{m}^2\text{s}^{-1}$), standard ($10^3\text{m}^2\text{s}^{-1}$) and low ($10^3\text{m}^2\text{s}^{-1}$) viscosity regimes following a WWE in February. The first baroclinic mode is well resolved in all three cases, while the second mode is weaker in the low viscosity regime. The standard and low viscosity regimes exhibit considerable variability in addition to the Kelvin wave signal itself. This does not occur in the high viscosity regime, where the background Tropical Instability Wave (TIW) field is damped out and is absent. This again suggests that the westward propagating features that occur after the Kelvin wave passes are the result of interactions with the background TIW field.

The top panels of Figure 6.9 show the projection of the zonal velocity anomalies generated by a February WWE onto the first two baroclinic modes at 80° longitude on the Equator for each viscosity regime. The bottom panels show the temporal evolution of the vertical profile of zonal velocity anomaly at this location. Table 6.2 summarises the maximum amplitudes for the first two modes in each configuration. The high viscosity regime has a bi-modal structure, as does the standard configuration, though the amplitude of the modal coefficients are weaker. This is reflected by the zonal velocity anomaly that is deeper and an order of magnitude weaker than

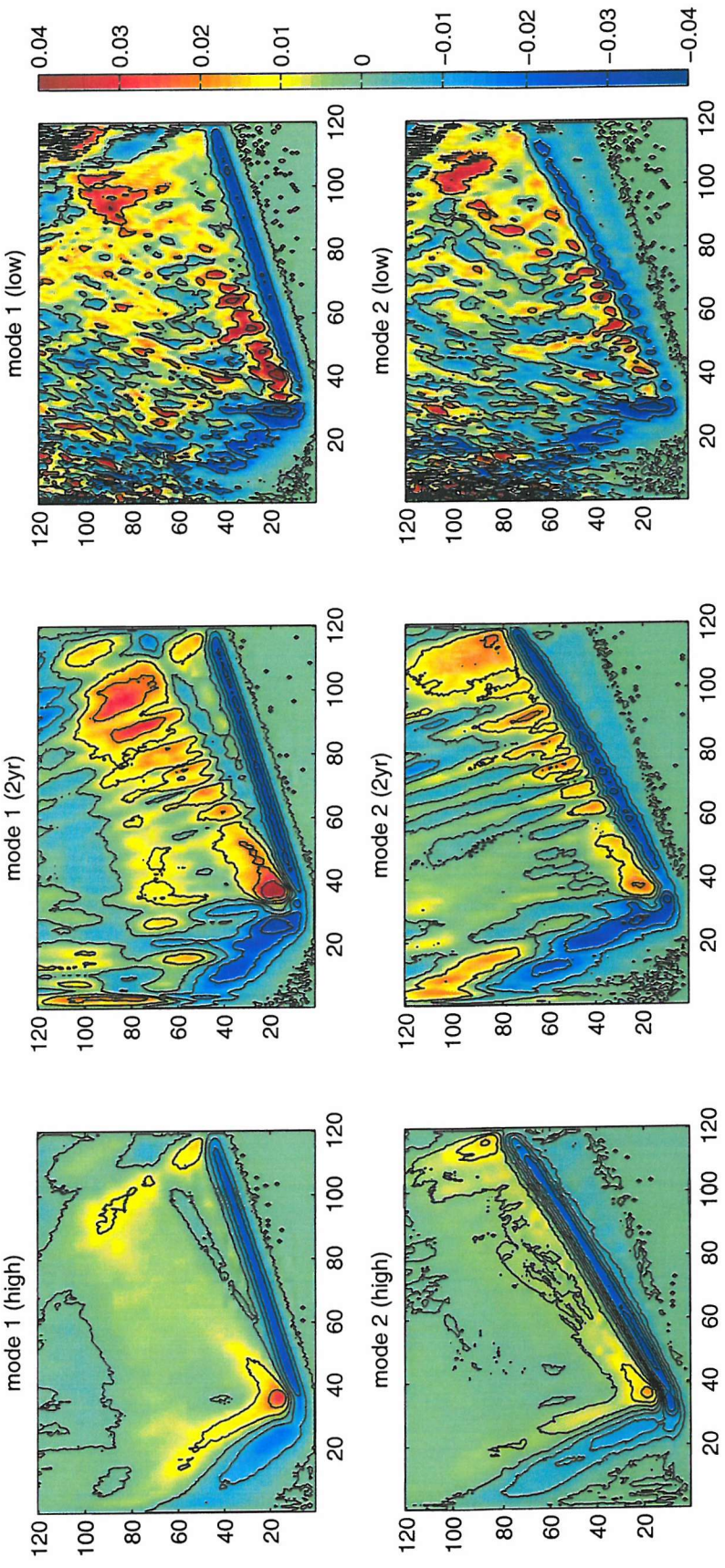

Figure 6.8: Modal analysis of zonal velocity anomaly along the Equator for a WWE generated in February (iso high 2yr low). The coefficient (ucoeff) is in units of ms^{-2}.

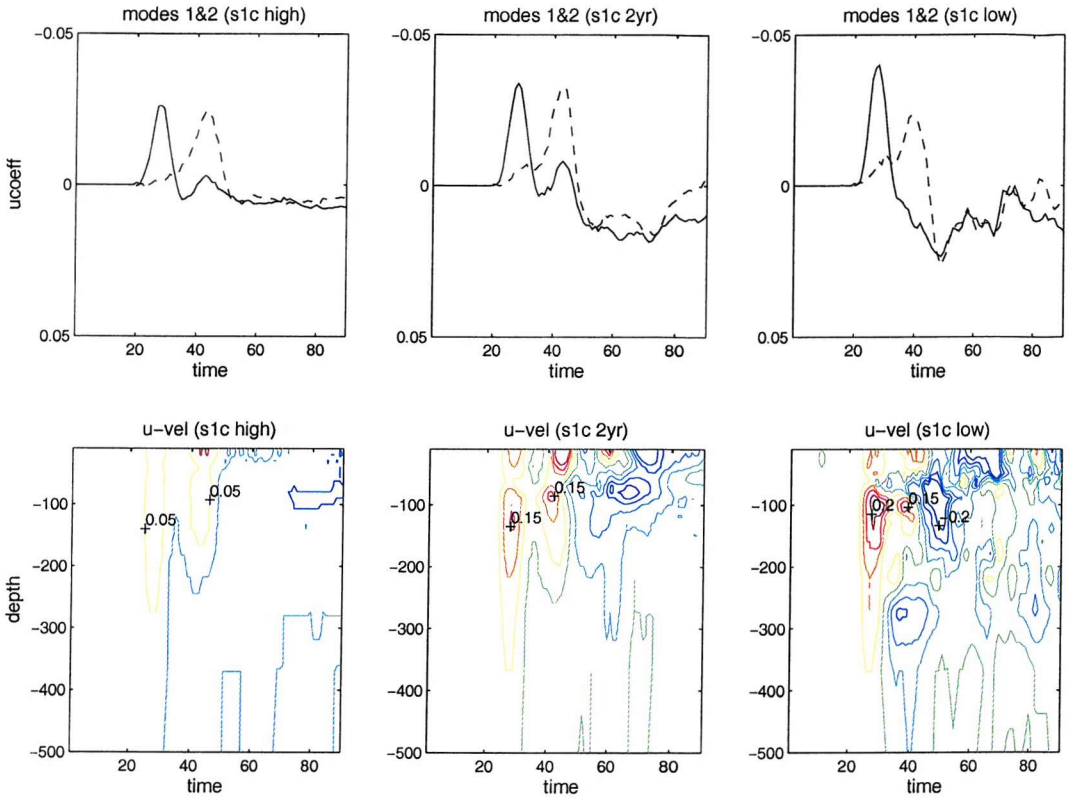

Figure 6.9: Modal analysis of zonal velocity anomaly at 80° longitude on the Equator for a WWE generated in February under different horizontal viscosity conditions (iso high, 2yr, low). The coefficient (ucoeff) is in units of ms^{-2} and the zonal velocity contour interval is $0.05ms^{-1}$.

in the standard configuration (iso 2yr), as expected for a more viscous ocean. In the low viscosity case, there is a marked reduction in amplitude of the second mode, with a slight increase in the amplitude of the first mode that is accompanied by a increase in the maximum zonal velocity anomaly associated with the arrival of the first mode, from $1.5ms^{-1}$ to $2.0ms^{-1}$.

viscosity (m^2s^{-1})	mode 1 ucoeff ($10^{-2}ms^{-1}$)	mode 2 ucoeff ($10^{-2}ms^{-1}$)
high - 10^4	2.5	2.3
standard - 10^3	3.3	3.2
low - 10^2	3.8	2.2

Table 6.2: Amplitude of the first and second baroclinic modal coefficient (ms^{-1}) under different horizontal viscosity conditions (iso high 2yr low).

6.5 Propagation Through a Sloping Thermocline

The interannual ENSO variability of the Equatorial Pacific region forces a basin-wide modulation of the equatorial thermocline. The intensification of the Trade winds during La Niña conditions leads to a steepening of the thermocline and a slackening of the Trades during El Niño leads to a gentler thermocline gradient. Benestad et al. (2002) have shown that when there is a steep, interannually-forced gradient the Kelvin wave signal is damped out before reaching the eastern boundary. A shoaling thermocline affects periodically-generated Kelvin wave propagation by leading to partial reflection as Rossby and inertia-gravity waves (Gill, 1985; Busalacchi and Cane, 1988).

The mechanisms by which a sloping thermocline can influence Kelvin wave propagation depend on whether the theory assumes conservation of the energy flux. Wave fronts propagating into a shoaling thermocline lead to changes in the mass flux that is associated with the wave front, while the energy flux is conserved (Long and Chang, 1990). Benestad et al. (2002) however found that partial reflection could not account for the levels of attenuation observed and that this is explained by the energy flux not being conserved as such high levels of attenuation would not result otherwise. The attenuation could be caused by the increased viscous dissipation, due to the increased vertical shear occurring in a region with a steeply sloping thermocline. When a Kelvin wave propagates into a shoaling thermocline the vertical redistribution of energy by intramodal scattering may occur leading to a change in amplitude.

A series of experiments is carried out here to study the propagation of a Kelvin wave through a sloping thermocline, focusing on the sensitivity of the baroclinic modal structure of the wave to the varying background stratification. A WWE is applied to three different mean states where the background Hellerman and Rosenstein (1983) wind stress is successively amplified from the standard wind field by doubling, then quadrupling for the f2 and f4 configurations respectively, as described in Chapter 3. Upwelling is amplified in the eastern basin and the along Equator thermocline is successively steepened, as Figure 4.2 showed. The vertical structure of the eigenmodes is expected to be sensitive to the changing vertical stratification along the sloping equatorial thermocline.

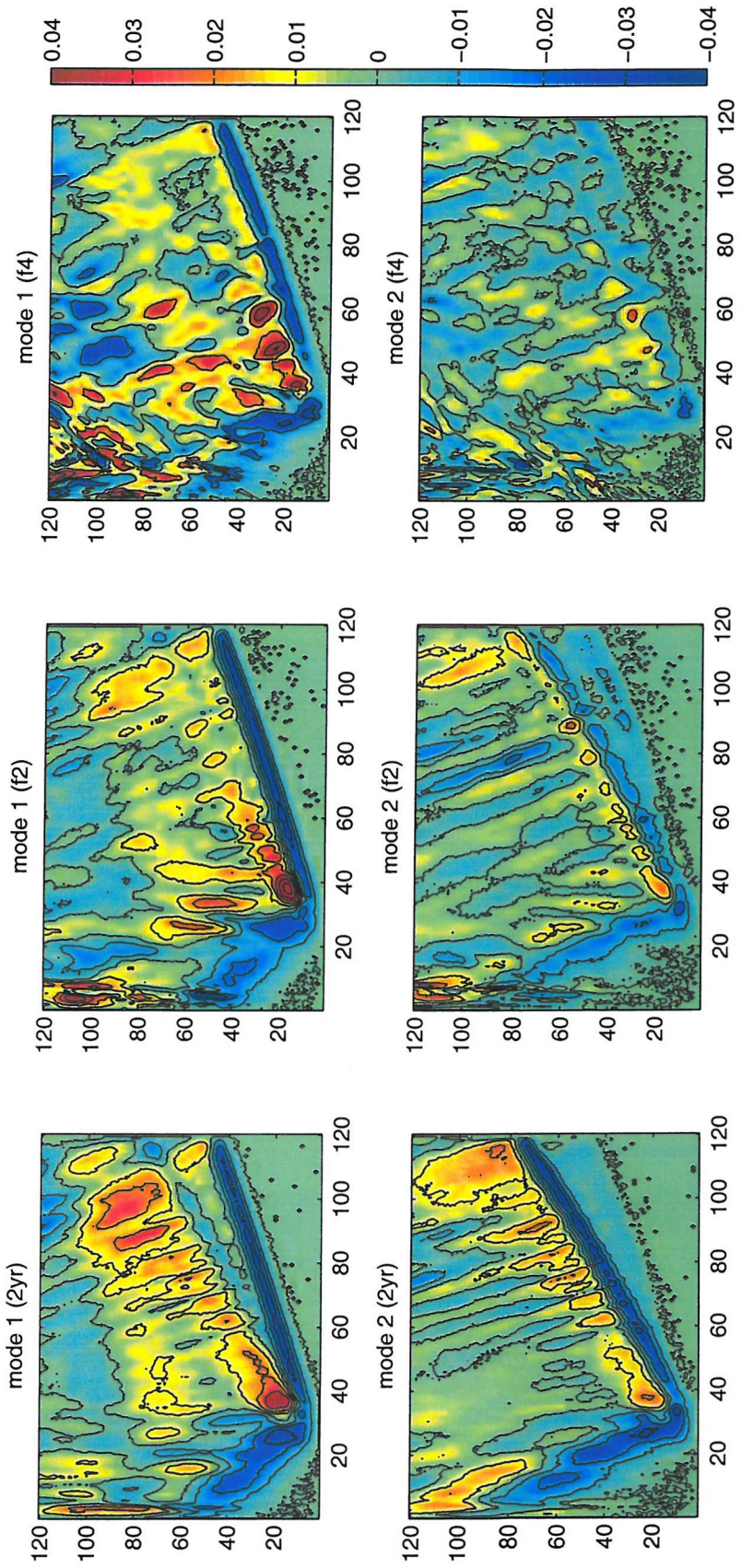

Figure 6.10: Projection of the zonal velocity anomaly onto the modal coefficient (ms^{-2}) along the Equator for a WWE generated in February where the backround wind stress is successively doubled (iso 2yr, f2, f4).

Figure 6.10 shows the along-Equator projection of the zonal velocity anomaly onto the first two baroclinic modes for experiments where the background Trade winds are successively augmented. The amplitude of the second mode in the standard configuration maximum, which at 80° longitude is -0.032ms^{-1} and is comparable to the magnitude of the first mode. As the background wind stress is amplified, the amplitude of the second mode weakens to the point where it is barely distinguishable in the f4 configuration, as seen in Figure 6.10. The sensitivity of the second mode to the changing along-Equator stratification in these experiments is due to the vertical structure of the eignmode having a maximum at depth, generally around 100m, which is comparable to the depth of the thermocline as shown by the along-Equator mean squared Brunt-*Väisälä* frequency in Figure 6.3.

The variability in the modal coefficient occurring in Figure 6.10 after the arrival of the Kelvin wave reduces as the background wind stress is increased from the standard to the f4 configuration. For example, the amplitude of the first mode in Figure 6.10 at 90°longitude after day 80 in the standard configuration is around 0.03ms^{-1}, while it only reaches an amplitude of 0.01ms^{-1} in the f4 configuration. This feature is also present in the bottom panel of Figure 5.19 and has been shown to be the result of a phase shift in the TIW field in Section 5.3. This reduction in the modal signal due to the TIW perturbation coincides with weakening in amplitude of the second mode of the WWE-generated Kelvin wave as the background wind stress is increased from the standard to the f4 configuration. This also corresponds with the weaker SST anomalies generated in the f4 configuration shown earlier in Figure 5.19. The Kelvin wave generates a stronger SST anomaly in the standard configuration compared with the configurations where the background wind stress is successively increased. The SST anomaly generated decreases as the thermocline gradient is increased, as a result of the weaker projection of the WWE onto the second baroclinic mode of the Kelvin wave. In the standard configuration, SST anomalies of 1°C result from the interaction with the TIW field, while in the f2 and f4 configurations, TIW-related SST anomalies are less than 0.5°C. This has shown that the evolution of the SST field is related to the sensitivity of the second baroclinic mode to a steepened thermocline. This is the result of the perturbation of the background ocean conditions by the Kelvin wave.

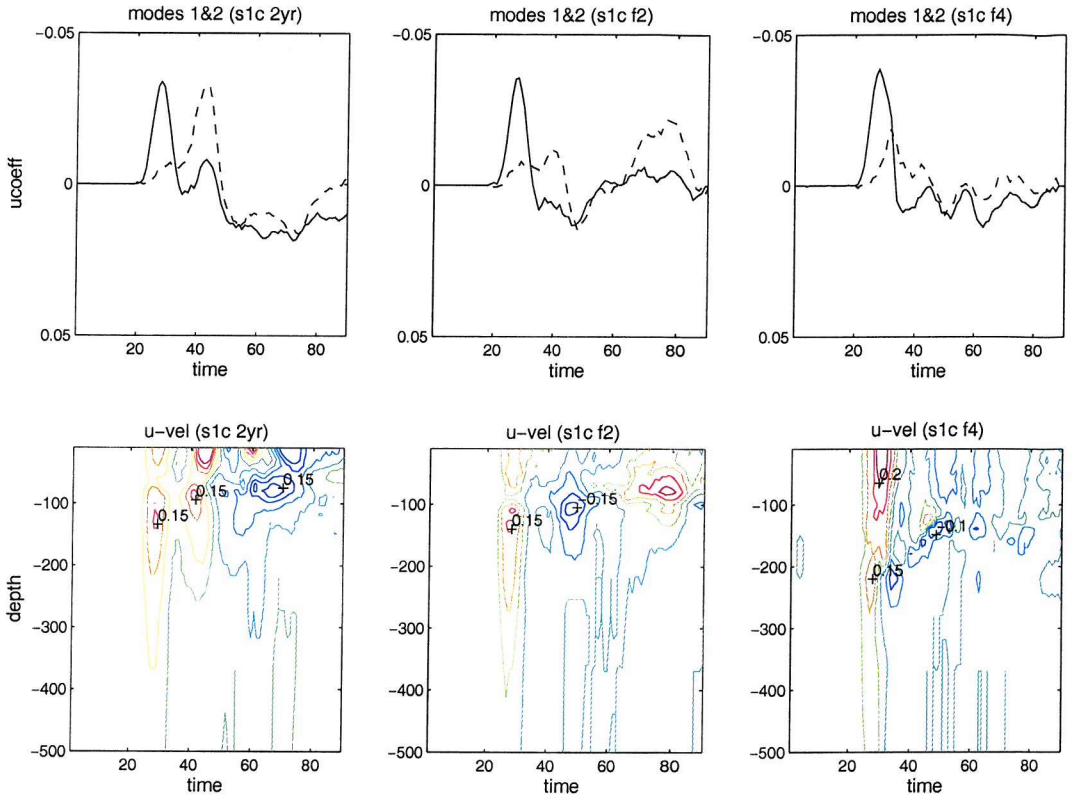

Figure 6.11: Modal analysis of zonal velocity anomaly at 80° longitude on the Equator for a WWE generated in February where the backround wind stress is successively doubled (iso 2yr, f2, f4). The contour interval is $0.05 \mathrm{ms}^{-1}$.

The top panels of Figure 6.11 show the arrival at 80° longitude on the Equator of the first and second baroclinic mode of a Kelvin wave generated by a February WWE. As the background wind stress is increased, the amplitude of the first mode increases slightly, while that of the second mode decreases so it is of the same magnitude as the variability in the modal coefficient after the Kelvin wave has passed. Table 6.3 summarises the maximum amplitude of the two modes in each configuration. While the amplitude of the first mode increases as the background wind stress increases, that of the second mode is halved in magnitude. The amplitude of the second mode, as measured at 80° longitude, is weakest for the f2 case, though this is the result of sampling at this particular location. When looking at the second mode in Figure 6.10, it is clear that the projection is weakest for the f4 configuration.

The bottom panels show the temporal evolution of the zonal velocity anomaly at this location over the top 500m. An eastward velocity anomaly maximum of $0.15 ms^{-1}$ is associated with the second mode in the standard and f2 configurations. However, a postive zonal velocity anomaly generated by the arrival of the second mode is not distinguishable in the f4 configuration.

background wind stress config.	mode 1 ucoeff ($10^{-2} ms^{-1}$)	mode 2 ucoeff ($10^{-2} ms^{-1}$)
standard	3.3	3.2
f2	3.4	1.1
f4	3.7	1.8

Table 6.3: Amplitude of the first and second baroclinic modal coefficient (ms^{-1}) under different background wind stress conditions (iso 2yr f2 f4).

6.6 Projection of a WWE onto modes

The wind stress forcing function can be expressed as a normal modes expansion (Gill and Clarke, 1974; Gill, 1982). In the case for zonal wind stress (τ^x) forcing, the zonal momentum equation becomes

$$u_t - \beta y v = -g\eta_x + \rho_o^{-1}\tau_z^x \tag{6.17}$$

The wind stress term then expands as

$$\rho_o^{-1}(\delta\tau_x/\delta z) = \tilde{X}_n(x,y,t)\hat{p}_n(z) \tag{6.18}$$

where $\hat{p}_n$ are the eigenfunctions and the coefficient $\tilde{X}_n$ is the temporal-horizontal function for each mode (n).

The vertically averaged modes are orthogonal to each other and equation 6.18 can be multiplied by $\hat{p}_m$ and integrated over depth so that we can obtain an expression for $\tilde{X}_m$.

$$\tilde{X}_m = \frac{\tau_s/H_1 \int_{-H_1}^{0} \hat{p}_m/\rho_o dz}{\int_{-H}^{0} \hat{p}_m^2/\rho_o g dz} \tag{6.19}$$

The wind stress is assumed to vary linearly with depth from its maximum value at the surface (τ_s) to zero at the bottom of the first model layer, $-H_1$, and is considered as a body force acting linearly with depth over the first layer. For the first two baroclinic modes, $\hat{p}_m$ is assumed to be approximately uniform in the mixed layer, close to its surface value. The amplitude of the coefficient $\tilde{X}_m$ quantifies the projection of the wind stress onto the different vertical modes.

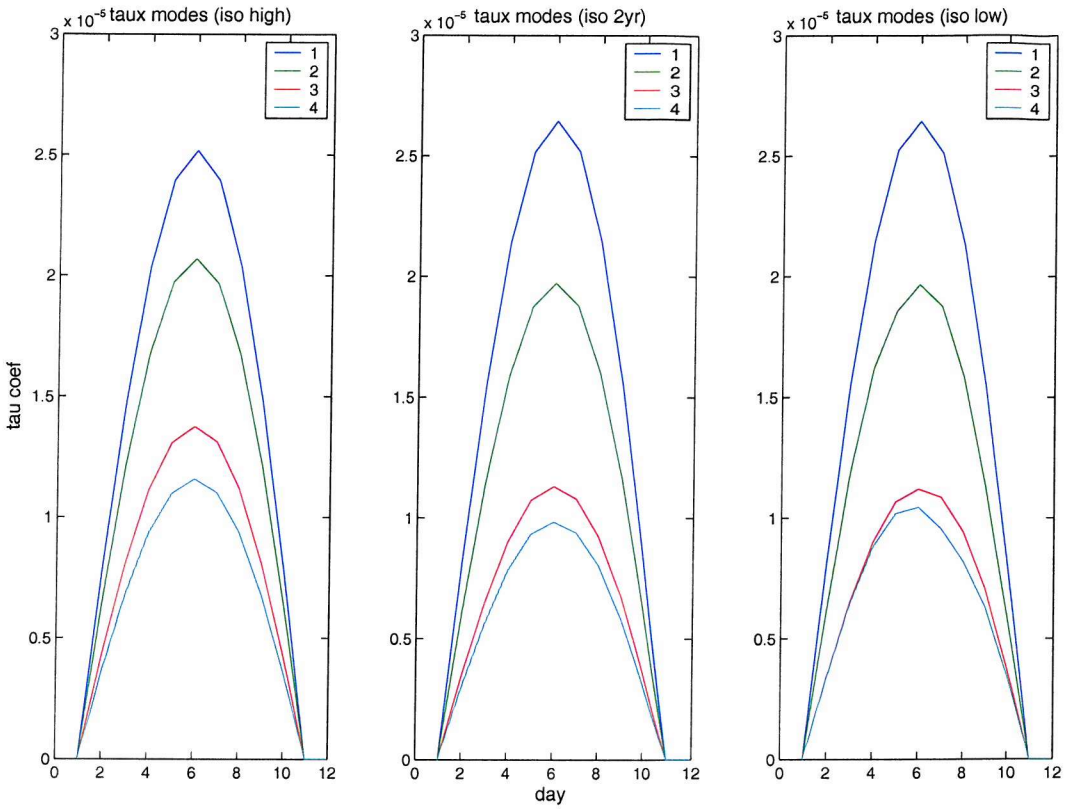

Figure 6.12: The temporal evolution of the modal projection coefficient $\tilde{X}_m$ (ms^{-2}) of modes 1 to 4 for a February WWE at the Equator, 30° longitude for the high, standard and low viscosity configurations(s1c high, 2yr, low).

Figure 6.12 shows the projection of a February WWE on the modal coefficient $\tilde{X}_m$ for the four gravest baroclinic modes for the different horizontal mixing configurations. The signal is predominantly distributed between the first and second mode for all three configurations. Table 6.4 shows the maximum amplitude of $\tilde{X}_m$ for the four modes in each configuration. The WWE projection of the standard and low viscosity configurations have a comparable maximum amplitude of the first and second mode coefficient, as shown in Table 6.4. For the high viscosity case, the amplitude of the first mode is reduced while that of the second is increased with respect to the other two configurations. The magnitude of the third and fourth modes is also greater than for the other two configurations. This is despite a weaker signal in the Kelvin wave generated in these conditions.

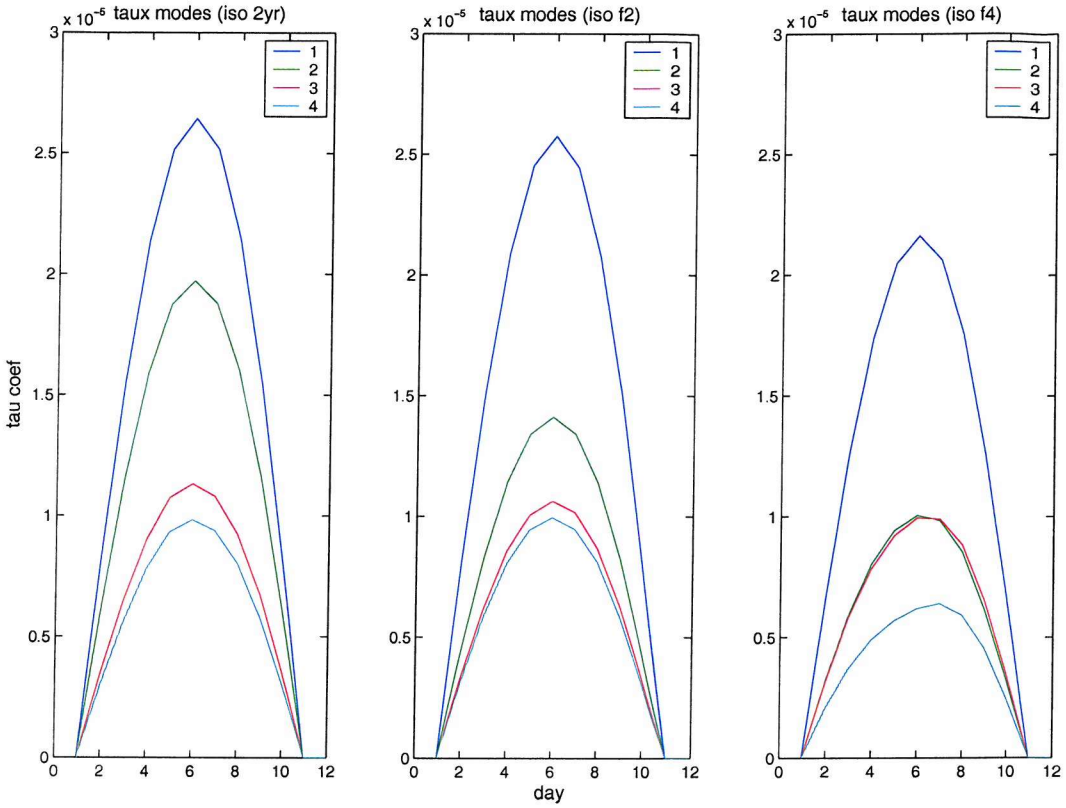

Figure 6.13: The temproal evolution of the modal projection coefficient $\tilde{X}_m$ (ms^{-2}) of modes 1 to 4 for a February WWE at the Equator, 30° longitude for the standard, f2 and f4 wind stress configurations(s1c 2yr, f2, f4).

The projection of the WWE onto the vertical modes in the different background wind stress configurations is shown in Figure 6.13. The maximum amplitude of the four modes is given in Table 6.5. The amplitude of the first mode reduces as the background wind stress is increased. The amplitude of the second mode is particularly sensitive, halving in magnitude from the standard to the f4 configuration, reaching the same amplitude as the much weaker third mode. The amplitude of the third mode is least affected by the changing wind field, while the amplitude of the fourth mode decreases as the background wind stress increases. It is not clear why the temporal evolution of the fourth mode appears to be slightly skewed on close examination of both Figures 6.12 and 6.13.

configuration	mode 1	mode 2	mode 3	mode 4
high	2.51	2.07	1.37	1.16
standard	2.64	1.97	1.13	0.98
low	2.64	1.96	1.12	1.04

Table 6.4: Projection coefficient maximum amplitude ($10^{-5}ms^{-2}$) for the gravest four baroclinic modes forced by a February WWE under different horizontal viscosity conditions (s1c high, 2yr, low).

configuration	mode 1	mode 2	mode 3	mode 4
standard	2.64	1.97	1.13	0.98
f2	2.57	1.41	1.06	0.99
f4	2.16	1.00	0.99	0.62

Table 6.5: Projection coefficient maximum amplitude ($10^{-5}ms^{-2}$) for the gravest four baroclinic modes forced by a February WWE under different background wind stress conditions (s1c 2yr, f2, f4).

Figure 6.14 shows the vertical profile of the Brunt-Väisälä frequency (N^2) located at the centre of the WWE at 30° longitude on the Equator, on day five of the WWE. This is where and when there is the maximum WWE perturbation amplitude of 0.3Pascals. The N^2 profile in the left hand panel shows the stratification for the mixing sensitivity configurations, and in the right hand panel that of the different wind stress configurations, where the maximum projection of the WWE perturbation onto the vertical baroclinic modes occurs. In the left hand panel of Figure 6.14, the profiles of the mixing sensitivity experiments are similar, all with a maximum in the vertical density gradient at a depth of 140m. However in the right hand panel of Figure 6.14, the maximum vertical density gradient varies significantly between the different wind stress configurations. As the background wind stress is increased, the pycnocline strengthens and deepens from a depth of 140m to 220m. An important feature of the stratification is the well mixed upper 150m of the f4 configuration, after which there is a steep increase in stratification. The development of this vertical structure in the f2 to the f4 configuration, due to the increase in wind mixing of the surface layers, is responsible for the reduction in amplitude of the second baroclinic mode forced by the wind perturbation.

Differences in the stratification are the main factor influencing the modal projection of the WWE in the different experiments. Associated to this is the vertical velocity structure and shear from the sea surface to the base of the thermocline that contains the surface wind-forced flow and subsurface Equatorial Undercurrent (EUC). This is not accounted for in the modal projection as a condition of zero mean flow is assumed in the calculation. The meridional stratification and velocity field variation across the Equator may also be important for how the WWE projects onto the Kelvin wave, particularly for WWE located off the Equator. The strongest velocity shear is associated with the core of the EUC, occurring at the Equator, as Figures 4.3 and 4.4 showed. The depth of the thermocline deepens poleward of the Equator (not show). The result of this meridional variability could be that the baroclinic structure of Kelvin waves generated by WWEs located off the Equator may be less sensitive to these factors since a deeper thermocline will be less sensitive to such configurations so that the amplitude of the second mode will also be less sensitive to these different configurations.

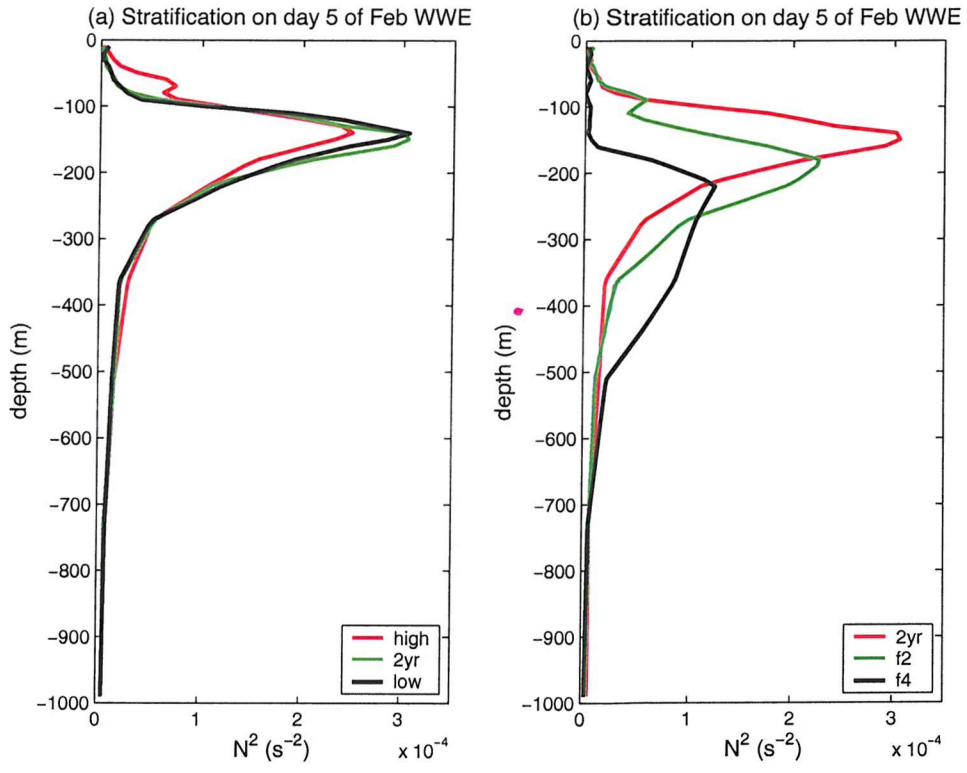

Figure 6.14: The Brunt-Väisälä frequency (s^{-1}) on day 5 of a February WWE at the Equator, 30° longitude for (a) the high, standard and low viscosity configurations (s1c high, 2yr, low) and (b) for the different background wind stress conditions (s1c 2yr, f2, f4).

6.7 Summary

The modal analysis of wind-generated Kelvin waves shows that the first baroclinic mode generally accounts for a large part of the signal that reaches the eastern boundary. We find the second baroclinic mode can be of the same magnitude as the first in some configurations. Simulations by level models (Harrison, 1989; Giese and Harrison, 1991) also give a large second mode response, while for a multi-layer reduced-gravity model (Kindle and Phoebus, 1995) the results showed that the second mode sea level response was only a third of that of the first mode. The Kelvin wave generated by the wind event in the standard configuration has a structure that is dominated by the first two modes, with a much weaker signal in the higher modes and an even distribution of energy between the first two baroclinic modes.

The second baroclinic mode is sensitive to changes in the background state of the ocean, simulated here in a series of configurations. The first mode was generally unaffected by the changes in the background state imposed by different mixing regimes and background wind stress regimes. The first baroclinic mode has already been shown to be unaffected by the background zonal circulation as it has a faster phase speed compared to the EUC velocities and the meridional extent of the EUC core is much smaller than the meridional extent of the first mode (Philander, 1979). The second mode however has a high amplitude in the thermocline region and its sensitivity is an important factor in terms of the remote response of the upper ocean to a WWE in the western part of the basin. In observations, wind events that are comparable in magnitude generate different surface signatures in the eastern basin. These process studies have shown that the Kelvin wave modal structure depends on the background ocean state, modulated by variations in the thermocline gradient. This sensitivity may also be important in realistic Equatorial Pacific conditions that are modulated on a basin scale by the ENSO cycle. The seasonal cycle was found not to have a noticable impact on the Kelvin wave adjustment to a WWE.

Variations in the second baroclinic mode may account for changes in the phase speed of a wind-generated Kelvin wave. Changes in phase speed could be related to changes in background mean current velocities. This is difficult to determine as the currents change in maximum velocity, depth and intensity along the Equator. While the simulated currents are unrealistic here, variations in a realistic EUC were found to have little influence on the phase speeds of Kelvin waves (Johnson and McPhaden, 1993). The resolution of the background TIW field in modelling studies of the Equatorial Pacific region is important in terms of how the mean state is affected by the wind-generated Kelvin wave. All the experiments showed a high level

of westward propagating variability occurring after the Kelvin wave arrival, except in the case of the high viscosity regime, where the background TIW field is damped out and the background velocity field is relatively unperturbed after the Kelvin wave has propagated through.

A steepened thermocline leads to an increase in westward propagating energy that could be the signature of reflection of the Kelvin wave as Rossby waves, in agreement with Long and Chang (1990). While the Kelvin wave always reaches the eastern boundary, the changes in thermocline inclination affect its amplitude, as shown by the linear reduced gravity wave model of Busalacchi and Cane (1988). When the thermocline gradient is increased the projection of the WWE onto the second baroclinic mode is weakened. As a result of this, the SST anomaly that is generated decreases as the thermocline gradient increases. A WWE generated in steep thermocline conditions will lead to a weaker coupling with the atmosphere, reducing the capacity for the possible feedback resulting from the WWE-generated anomalies. The interaction with the background TIW field was also reduced when the second baroclinic mode was only weakly excited.

The expansion of the WWE wind stress onto ocean modes has shown that the same WWE will lead to a different perturbation of the ocean modes, depending on the stratification at the WWE centre. The first mode is dominant in all configurations, and the amplitude of the second mode depends on the configuration. The amplitude of the first four modes does not vary greatly with different levels of lateral mixing. However, the second mode is successively weaker as the background wind stress is increased in the f2 and f4 configurations as this leads to the formation of a well mixed surface layer that is over 100m deep in the f4 case.

Chapter 7

Kelvin Wave Adjustment Case Studies

7.1 Introduction

The work done so far has only looked at idealised WWE perturbations in idealised model ocean configurations. Though the experiments described previously have served to highlight the sensitivity of the forcing and the Kelvin wave modal structure to the background ocean conditions, conclusions about the importance of these results can only be drawn by looking for similar results in observed WWEs in realistic conditions. The work in this chapter will apply the finding that the second baroclinic mode is sensitive to the background ocean conditions by studying the baroclinic modal structure of two WWE of a similar magnitude that occurred in the Equatorial Pacific that led to a very different ocean response.

Two observed WWEs were selected, one that occurred in March 1997 and the other in December 2002, with Figures 7.1 and 7.2 showing the associated zonal wind and depth of the 20°C isotherm anomalies (TAO web page). These WWEs were chosen as, though both WWEs had a maximum amplitude of over $6ms^{-1}$ and were of a similar duration, the ocean response was very different. The March 1997 WWE led to a strong ocean response (Bergman et al., 2001) and was accredited with having played an important role in the development of the particularly strong 1997-98 ENSO event (Lengaigne et al., 2002, 2003; Vitart et al., 2003). However, the WWE that occurred in December 2002 did not produce a strong ocean response and it did not lead to a growth of sea surface anomalies, despite the moderate El Niño anomalies that had developed at the end of 2002. The 20°C isotherm depth anomaly generated by the Kelvin wave in March 1997 was of 40m, while only deepening by 20m in December 2002.

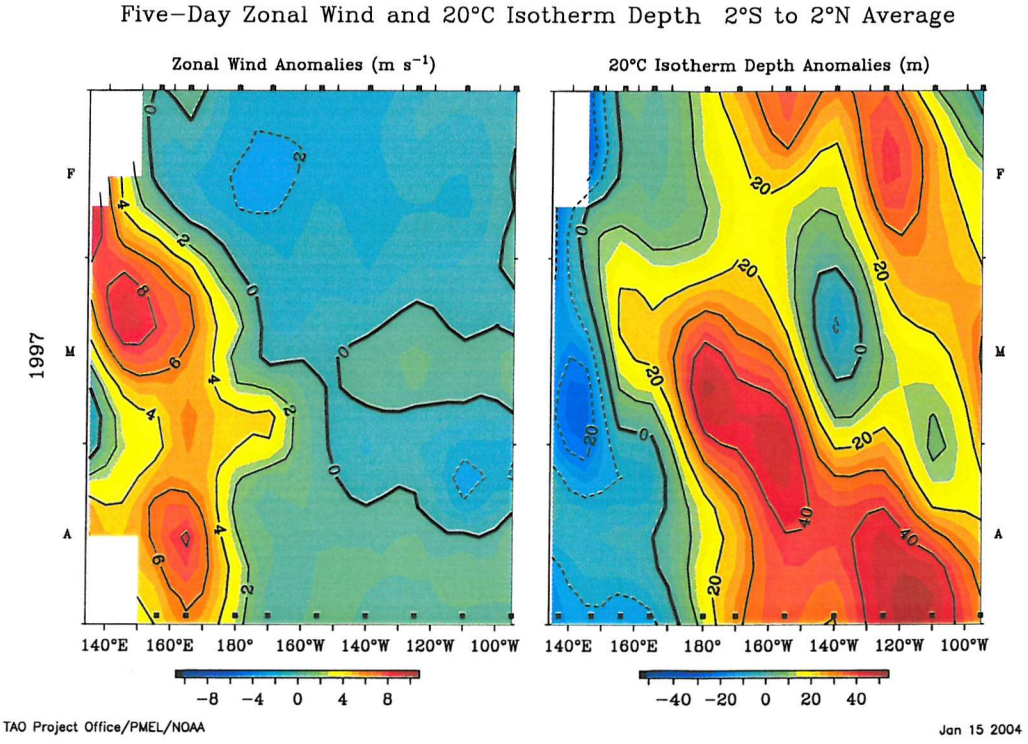

Figure 7.1: Zonal wind stress anomaly and depth of the 20° C isotherm depth anomaly along the Pacific Equator from the 1st February 1997 to the 30th April 1997 (TAO Project webpage: www.pmel.noaa.gov/tao).

The Kelvin waves from these case study periods are projected onto the vertical modes, in particular looking at the second baroclinic mode, to determine whether the modal structure is important in determining the ocean response. It is hypothesised that the WWE in March 1997 projected more strongly onto the second baroclinic mode than in December 2002 and that this is one of the reasons why the ocean response was greater in the 1997 case compared to that in 2002.

7.2 Ocean Analysis Data

Data is acquired from the ECMWF Seasonal Forecast System 2 (Anderson et al., 2003) Ocean Analysis. The model ocean is Version 2 of the Hamburg Ocean Primitive Equation (HOPE) model (Wolff et al., 1997). The ocean analysis is produced by five-ensemble analyses that are run daily forced by daily averaged atmospheric surface fluxes from the ECMWF operational analysis forecast system and with ocean thermal data that is assimilated every ten days.

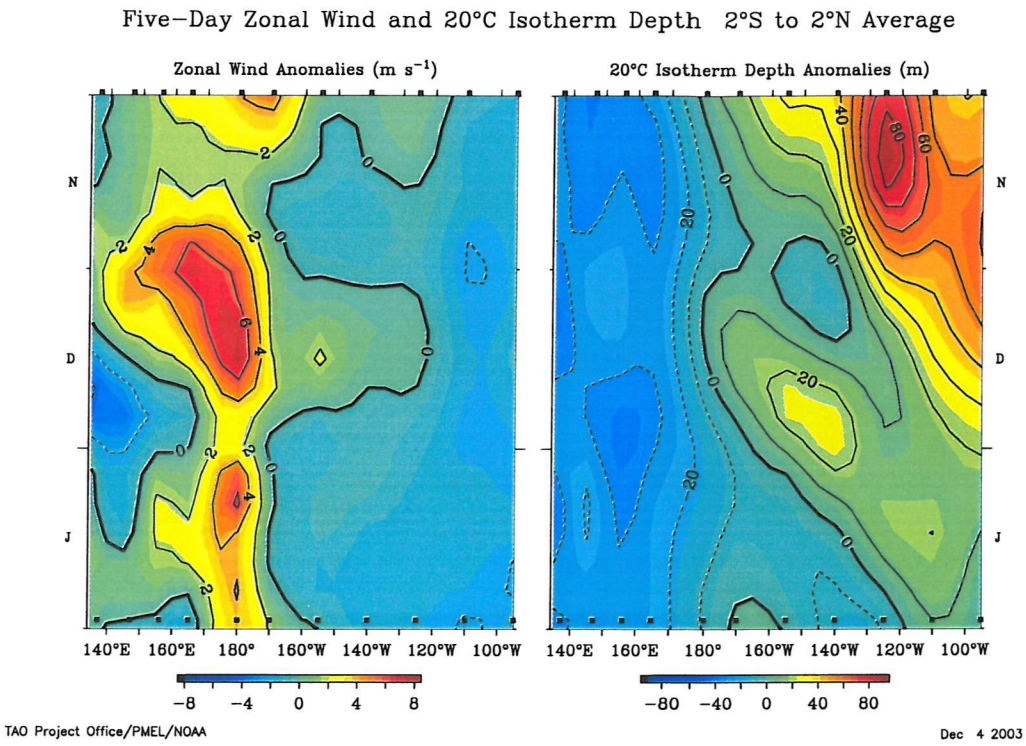

Figure 7.2: Zonal wind stress anomaly and depth of the 20° C isotherm depth anomaly along the Pacific Equator from the 1st November 2002 to the 31st January 2003 (TAO Project webpage: www.pmel.noaa.gov/tao).

Timeseries of three months, including the WWEs of interest, of full depth potential density and zonal velocity are extracted at the Equator. For the March 1997 WWE, data is extracted from 1st February to 1st April for years 1997, 1999, 2000, 2001 and 2002. The timeseries for the December 2001 WWE is collected from 1st November to 28th February for years with December in 1999, 2000, 2001 and 2002. A climatology is constructed from a mean of all the selected years in each case, with which the WWE anomaly is calculated. The unperturbed baroclinic modes are computed for the potential density climatology and then projected onto the zonal velocity anomaly related to the WWE. The Equatorial section from the ocean analysis data has a variable depth, though this does not pose a problem in the modal decomposition as it is carried out locally over the vertical profile at each longitude.

7.3 The Modal Structure of the Kelvin Wave

A timeseries of 60 days is isolated along the Pacific Ocean at the Equator for the March 1997 and December 2002 WWEs. The projection of the zonal velocity anomaly relative to the climatologies is shown for the first two baroclinic modes in Figure 7.3. The left hand panels show the March 1997 WWE and the right hand panels the December 2002 WWE. The colour scale for the first and second mode is the same for each WWE, though the scale differs between the two years. The Kelvin wave forced by the WWEs is clearly visible in both cases. The amplitude of the projection coefficient is greatest for the March 1997 case. In both cases, the Kelvin wave reaches the eastern boundary, though this is less clear in the second mode.

Results from Chapter 6 showed that the strongest upper ocean anomaly is generated when the WWE-forced Kelvin wave projects strongly onto the second baroclinic mode. It is difficult to diagnose whether the hypothesis posed earlier holds true here as the second baroclinic mode is of comparable magnitude to the first mode in both 1997 and 2002. However, it is suggested that the second mode in 1997 has a more coherent structure than that in 2002, particularly in the initial phase of the adjustment, in the central Pacific. The magnitude of the second mode in 2002 is much weaker, despite a weak maximum amplitude occurring in the central Pacific. The amplitude of the second mode in the eastern Pacific in 1997 is almost double that in 2002.

Figure 7.4 shows the modal structure at 80° longitude (referenced to the longitude axis of Figure 7.3) of the two case study WWEs. The top panels show the evolution of the first two modes with time and the bottom panels show the vertical zonal velocity anomaly from which the modes are calculated. Despite the presence of other background variability, there is a clear anomaly associated with the March 1997 Kelvin wave, both in the modal coefficients and the zonal velocity field. The arrival of the Kelvin wave leads to a zonal velocity anomaly maximum of $0.8 \mathrm{ms}^{-1}$ at around a depth of 100m. The December 2002 Kelvin wave leads to a weak peak in the first mode and a weak negative zonal velocity anomaly. There is no discernible signal in the second mode coefficient, though it is unclear whether the peak in the March 1997 second mode is indeed the second mode, or a manifestation of the first mode as it appears to have propagated to this location with the same phase speed.

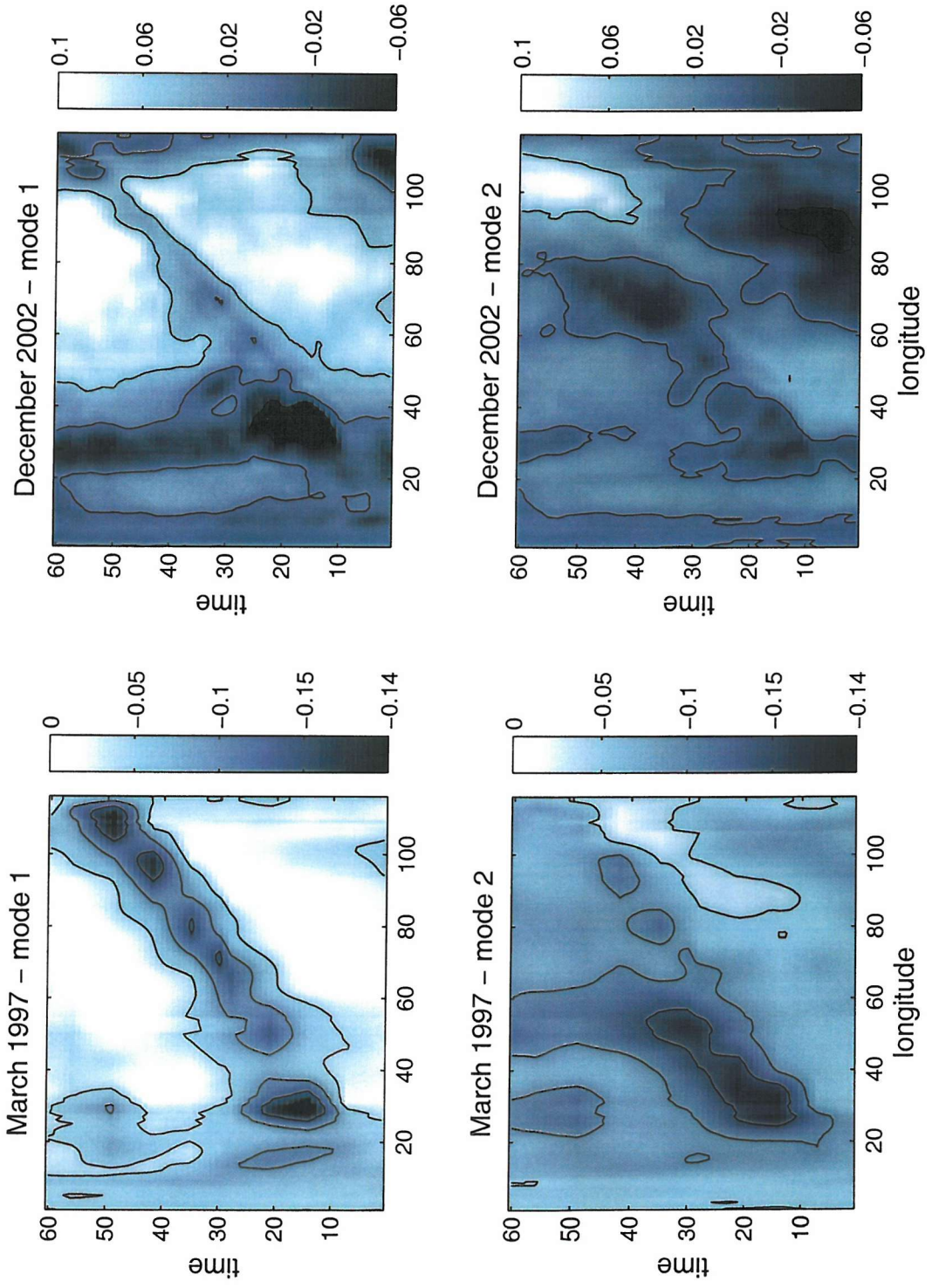

Figure 7.3: Modal decomposition of zonal velocity anomaly into the first two baroclinic modes along the Pacific Equator for the March 1997 WWE and the December 2002 WWE. The coefficient (ucoeff) is in units of ms^{-1}.

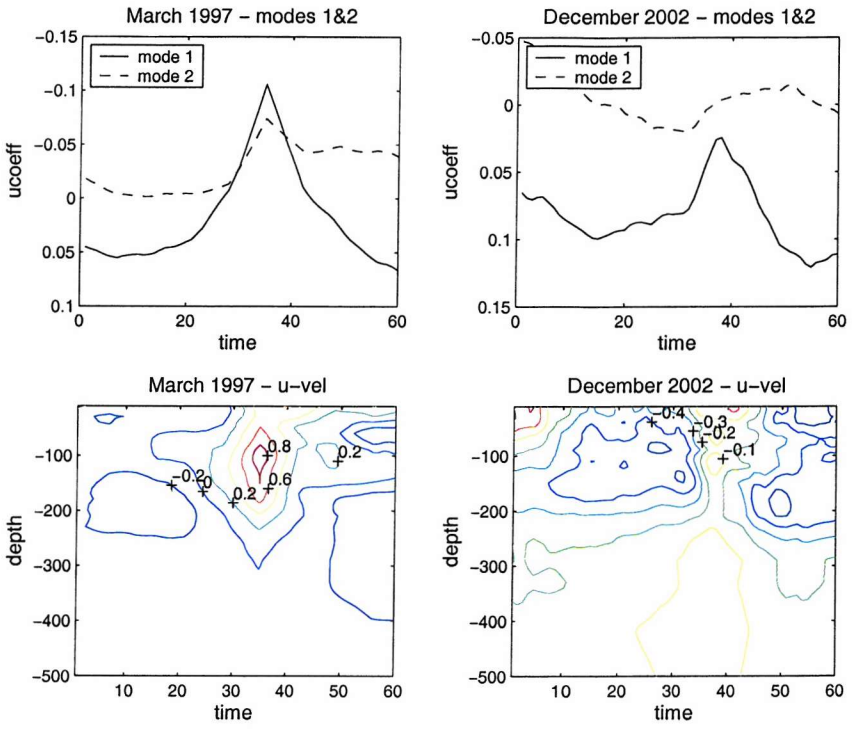

Figure 7.4: Modal decomposition of zonal velocity anomaly into the first two baroclinic modes and vertical profile of zonal velocity anomaly over the top 500m at 80° longitude (relative to the longitude axis of Figure 7.3), at the Equator for the March 1997 WWE (left hand panels) and the December 2002 WWE (right hand panels). The coefficient (ucoeff) is in units of ms^{-1} and zonal velocity is in ms^{-1}.

7.4 Projection of a WWE onto Modes

The results in Chapter 6 showed that the strength and baroclinic structure of the subsequent Kelvin wave was sensitive to how the WWE projected onto the ocean modes. In the absence of wind stress data of the observed WWEs, the idealised WWE used previously in the process studies is projected onto the ocean baroclinic modes at a location and time that corresponds to the occurrence of the WWEs in March 1997 and December 2002. The projection is computed from the unperturbed stratification at 30° longitude, commencing on day 10 of Figure 7.3.

Figure 7.5 shows the first four modes of the zonal wind stress decomposition in the March 1997 case on the left and December 2002 on the right. The WWE projects predominantly onto the first baroclinic mode. The maximum amplitude of the higher baroclinic modes is half that of the first mode, a structure that resembles that of the projection of the WWE onto the f4 configuration, shown in the right hand panel of Figure 6.13. The second mode is relatively stronger in March 1997, though it is not greater in amplitude than that in the December 2002 case and is due to the third and fourth modes being weaker.

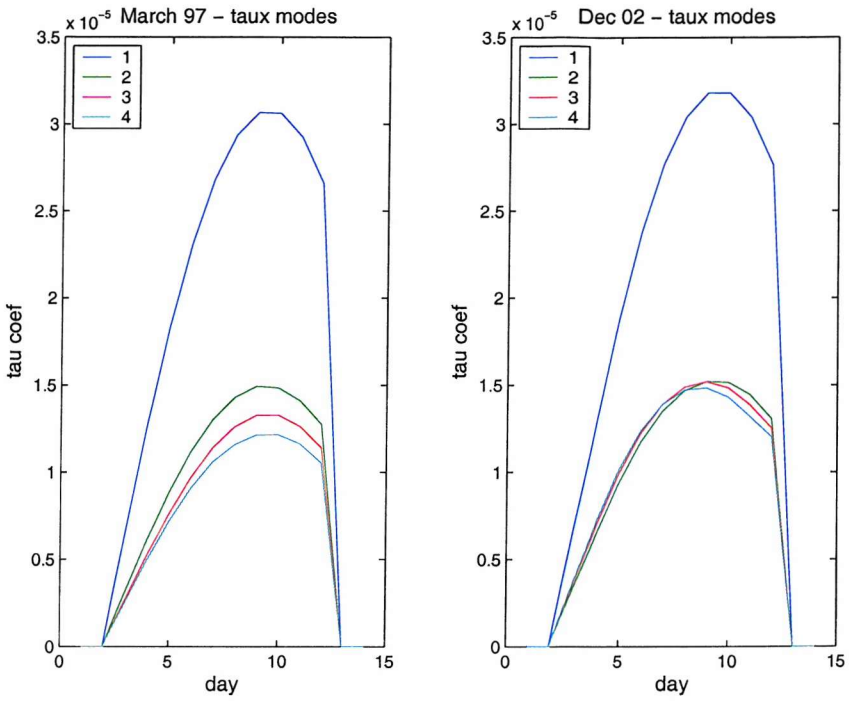

Figure 7.5: Modal projection of an idealised WWE onto the ocean baroclinic modes representing the March 1997 WWE and the December 2002 WWE. The coefficient (ucoeff) is in units of ms^{-1}.

7.5 Summary

The ocean response to two WWEs that are of a similar magnitude has been identified in ocean analysis data of the Equatorial Pacific Ocean. The ocean response, in terms of SST and depth of the 20°C isotherm anomalies is different, with the March 1997 WWE leading to strong anomalies and the December 2002 leading to weaker anomalies. Both WWEs led to an eastward propagating Kelvin wave that reached the eastern boundary. The Kelvin wave baroclinic modal structure has been studied and has shown that the March 1997 Kelvin wave projection onto the first and second baroclinic modes was around an order of magnitude stronger than that in December 2002.

Previous results from the process studies in Chapter 6 showed that stronger ocean anomalies are generated when the Kelvin wave has a strong second baroclinic mode, with the first mode having a much weaker impact on the upper ocean. There is an indication that this may also occur in the observed WWE ocean response, with the March 1997 Kelvin wave having a stronger and more coherent second mode. There are other factors that must be considered when determining causes for the ocean adjustment being different following these two WWEs other than the background stratification. These include differences in the ocean heat content, in the location of the WWE relative to the edge of the Warm Pool, and in the overall intraseasonal

variability. Both WWEs studied here took place during periods of high intraseasonal activity and were not isolated events, with prior strong WWEs having taken place. It is therefore not possible to isolate the overall significance of these individual WWEs on the Equatorial Pacific and draw any concrete conclusions here. However a weak sensitivity of the second mode to differing background conditions was observed and may be an important component of what determines the ocean response to any given WWE.

Chapter 8

Conclusions

The occurrence of the 1997-98 El Niño 'of the century' led to a proliferation of studies into the processes that take place in the Equatorial Pacific in an effort to explain the unusually rapid development and strength of this event, as well as to understand why most state-of-the art coupled models failed to forecast its growth. The period preceding the development of warm SST anomalies in the Central and Eastern Pacific experienced considerable intraseasonal MJO activity in the Western Pacific, characterised by a series of WWEs. These, and in particular a WWE that occurred in March 1997, forced an Equatoral wave response that is thought to have played an important role in the development of the El Niño anomalies.

The adjustment of the upper Equatorial ocean to a WWE has been studied here not only with the aim of studying how the mean ocean conditions are affected by the WWE forcing, but also focusing on the sensitivity of the ocean response to the background ocean conditions in an effort to understand why certain WWEs have a stronger impact on the Equatorial ocean than others. The OPA ocean GCM has been configured to an idealised Equatorial ocean domain and a series of process study experiments have been performed to study the Equatorial ocean and its adjustment to a WWE. This chapter will summarise the main results of this study, including its limitations, followed by some suggestions for future research and a discussion of the implications of the main results.

8.1 The Main Results

1. **Modelling the Equatorial Ocean**

   The Equatorial ocean circulation is sensitive to the prescribed levels of sub-grid scale lateral mixing. The mean flow is weakened in terms of current velocities, as well as thermal and velocity gradients as viscosity is increased. The transient Tropical Instability Wave field is most sensitive to levels of mixing. The instability processes that generate TIWs are destroyed when lateral viscosity is of the order $10^4 m^2 s^{-1}$, leading to a reduction in the equatorward transport of heat. In a low viscosity regime, where viscosity is of the order $10^2 m^2 s^{-1}$, the TIW field becomes more chaotic in structure with an increase in variance during the year due to an increase in numerical noise. The most suitable level of viscosity to simulate a TIW that more closely resembles the observations in the Equatorial Pacific is of the order $10^3 m^2 s^{-1}$. Simulating a realistic TIW field is not only important to model the principal characteristics of the Equatorial region, but also in terms of modelling the adjustment of the upper ocean to a WWE.

2. **The Ocean Adjustment to a WWE**

   A WWE in the western basin leads to an upper ocean adjustment by forcing an eastward propagating Kelvin wave and a westward propagating Rossby wave. The Kelvin wave forced by the analytical WWE leads to a perturbation of the background velocity field, both zonal and meridional, and SST anomalies that result from a phase shift occurring in the background TIW as the Kelvin wave propagates eastwards. These anomalies do not exist in the high viscosity regime when the background TIW is damped out.

   Increasing the background wind stress leads to a more energetic TIW field that extends across a greater latitudinal extent either side of the Equator. However, the SST and surface velocity anomalies caused by the Kelvin wave are reduced. Analysis of the baroclinic structure of the Kelvin wave has shown that the interaction of the Kelvin wave with the background TIW field depends on the strength of the second baroclinic mode, which is weaker in the increased background wind stress conditions.

3. **The WWE-Forced Kelvin wave**

   The results from process studies have shown that, while the amplitude of the first mode is generally greater than that of the second mode, the upper ocean conditions are most sensitive to the latter. The only other reference to the

importance of the second baroclinic mode forced by westerly wind anomalies in the Equatorial Pacific is in the work done by Bigg and Blundell (1989) who studied the normal mode structure of the Kelvin wave field prior to and during the 1982-83 El Niño. Most previous studies emphasise the role of the first mode, assigning secondary importance to the second and higher modes.

Experiments with a successively steepened thermocline have shown that the Kelvin wave always reaches the eastern boundary and that the steep thermocline gradient does not lead to the dissipation of the first and second baroclinic modes. The Kelvin wave does have a different modal structure in the different background wind stress configurations tested here, but the subsequent projection of the WWE onto the ocean modes shows that this structure is determined when the Kelvin wave is actually forced at the site of the WWE. The forcing of the second baroclinic mode is sensitive to the stratification at the WWE location and this structure is then maintained as the Kelvin wave propagates eastward.

4. **WWE Case Studies**

An attempt has been made to project the Kelvin wave forced by two case study WWEs onto the baroclinic modes. The Kelvin wave was isolated by subtracting a climatology from the WWE period, though this does not isolate the Kelvin wave forced by the WWE as the anomaly will also include unrelated variability from that year including the varying background mean state. For this reason it is difficult to compare directly the two Kelvin waves and equate the different modal structure to the nature of the ocean response for each case without taking into consideration the different background ocean conditions.

These preliminary results nonetheless suggest that the sensitivity of the second mode to the background ocean conditions may be a factor involved in determining the strength of the ocean response to the WWE. The March 1997 WWE led to much stronger upper ocean anomalies compared to the December 2002 WWE, and the Kelvin wave had a stronger second baroclinic mode relative to the 2002 Kelvin wave, though the second baroclinic mode signature is not as well defined as in the process study results.

8.2 Limitations

The WWE perturbation is limited to only considering the dynamic forcing by wind stress and the thermodynamic forcing has been ignored. While this simplification is useful for isolating the dynamic ocean adjustment, a more complete study would include the thermodynamic adjustment. WWEs lead to a localised heat flux perturbation and are often associated with intense precipitation that can lead to the formation of a fresh water lens that acts as a barrier layer to the dynamic adjustment. The WWE applied here is limited to being stationary, while observed WWEs tend to have an eastward propagation. The experiments here have also only focused on an isolated WWE, while periods when the MJO is active often have a series of WWEs that may lead to a cumulative effect that is more important that the effect of an individual WWE.

The results from the main body of this work have been produced by only a limited set of process study experiments, mainly due to computational and data storage constraints. Through the careful choice of a series of configurations it has been possible to model the key processes of interest in a simplified way to isolate sensitivities of the adjustment process that may be important in the Equatorial Pacific Ocean itself. A wider range of configurations would provide a more comprehensive sensitivity study. Greater spatial coverage of data output would enable a more detailed analysis of the background ocean state against which the effect of the WWE can be more thoroughly studied. Global spatial coverage of data would, for example, enable a more detailed study of the energetics of the TIW and whether this is modified by the WWE-forced Kelvin wave.

The initial comparison of results from process study experiments with a study of observed WWEs increases the applicability and relevance of the process study results. However, analysis of the case study WWEs only provides preliminary results as the Kelvin waves are only crudely isolated by removing an average calculated over four or five years and the rest of the variability during the WWE periods was not considered. The direct comparison of the adjustment to these two WWEs is inappropriate as they are different events, unlike the process study experiments that considered identical WWEs in different ocean conditions. To study the Kelvin wave in realistic ocean conditions, it would have been preferential to perform experiments in an ocean-only realistic configuration model applying an identical idealised WWE.

8.3 Future Work

A more systematic gradual study of the sensitivity of the Kelvin wave to the ocean state would allow us to build on the limited range of sensitivity studies performed here is needed. While those carried out in this study were useful to identify an important sensitivity of the adjustment process, in order to be able to bring information from these process study results to a real world application where the variability in mean state is less dramatic. For example, the sensitivity of the WWE projection onto the ocean baroclinic modes depending on the local stratification could be tested using gradually varied analytical stratification.

Since the case study analyses gave a preliminary positive result, there is scope for studying observational examples in more detail to test the robustness of the process study result that indicated the importance and sensitivity of the second baroclinic mode. Confirming such attributes of the baroclinic structure of the WWE-forced Kelvin wave could provide an additional element of predictability of the evolution of the system. The baroclinic structure of the Kelvin wave is determined at the WWE location in the process study results, with the characteristics of the Kelvin wave not changing significantly as is propagates eastward. It is not possible to ascertain whether this is applicable in the case of the observed WWEs and this should be studied in greater detail. If the structure of the Kelvin wave is indeed determined at the point of formation, then knowledge of the WWE location and local ocean conditions could give an indication of whether the Kelvin wave will lead to a strong ocean response.

The impact of the WWE-forced Kelvin wave adjustment on the Equatorial ocean and whether it leads to a rectification of the mean state needs to be studied further. This requires the initial study of the evolution of a realistic ocean model configuration that can then be furthered with a fully-coupled model as the rectification of the mean ocean state would be sensitive to coupled feedbacks. While the surface ocean adjustment is most important in terms of a coupled response, more needs to be understood about the development of the subsurface ocean mean state as the formation of ENSO SST anomalies are related to the development of subsurface temperature anomalies.

One of the main unresolved questions is whether the upper ocean is modulated by the mean intraseasonal variability or by individual or a sum of stochastic events. This would depend on whether the ocean response to intraseasonal variability is linear or non-linear. Experiments with an ocean-only model could be forced by the low frequency component of the intraseasonal wind field or by individual or a series of high frequency perturbations. To fully model the evolution of the upper ocean it would be necessary to progress onto experiments where a coupled feedback would be enabled. Applying analytical wind fields allows some control on understanding what determines the oceanic adjustment, after which subsequent experiments could be carried out using observed individual events or a composite wind field.

8.4 Summary

The results of the process studies have shown that the response of the Equatorial ocean to a WWE depends on the background state of the ocean and that this affects how the WWE projects onto the ocean baroclinic modes. The modal structure of the Kelvin wave is predominantly composed of the first and second modes. The second mode is important as its amplitude depends on the background ocean conditions and is mainly responsible for perturbing the upper ocean. Stronger sea surface anomalies are generated by a stronger second baroclinic mode.

The implications of these results can only be suggested when considering the application of the process study results to the analysis of case studies taken from observations in the Pacific Ocean. The idealised nature of the process studies is intended to aid in the search for deterministic mechanisms and processes for how the upper Equatorial ocean adjusts to WWEs and how the response leads to an effect on the evolution of the mean state. It is impossible to consider any of the dynamical process of the Equatorial Pacific in isolation as they are all intrinsically interconnected. The complexity of the adjustment of the Equatorial ocean to wind variability should be adressed using a complementary approach ranging from further simplified process studies to fully-coupled realistic model integrations.

Bibliography

Allen, M. R., Lawrence, S. P., Murray, M. J., Mutlow, T., Stockdale, T. N., Llewellyn-Jones, D. T., and Anderson, D. L. T. (1995). Control of Tropical Instability Waves in the Pacific. *Geophysical Research Letters*, 22:2581–2584.

Anderson, D., Stockdale, T., Balmaseda, M., Ferranti, L., Vitart, F., Doblas-Reyes, P., Hagedorn, R., Jung, T., Vidard, A., Troccoli, A., and Palmer, T. (2003). Comparison of the ECMWF seasonal forecast Systems 1 and 2, including the relative performance for the 1997/8 El Niño. Technical Report 404, European Centre for Mid Range Weather Forecasting.

Balmaseda, M. A., Vitart, F., Ferranti, L., and Anderson, D. L. T. (2002). Westerly wind events and the 1997 El Niño event in the ECMWF seasonal forecasting system: a case study. Technical Report 370, European Centre for Mid Range Weather Forecasting.

Barnston, A. G., He, Y., and Glantz, M. H. (1999). Predictive skill of statistical and dynamical climate models in SST forecasts of the 1997-98 El Niño episode and the 1998 La Niña onset. *Bull. Amer. Meteor. Soc.*, 80:217–244.

Battisti, D. S. (1988). The dynamics and thermodynamics of a warming event in a coupled tropical atmosphere-ocean model. *J. Atmos. Sci.*, 45:2889–2919.

Battisti, D. S. and Hirst, A. C. (1989). On the role of off-equatorial oceanic Rossby waves during ENSO. *J. Phys. Oceanogr.*, 19:551–560.

Belamari, S., Redelsperger, J. L., and Pontaud, M. (2003). Dynamic role of a Westerly Wind Event in triggering and Equatorial Pacific Warm Event. *J. Climate*, 16(12):1869–1890.

Benestad, R. E., Sutton, R. T., Allen, M. R., and Anderson, D. L. T. (2001). The influence of subseasonal wind variability on Tropical Instability Waves in the Pacific. *Geophysical Research Letters*, 28:2041–2044.

Benestad, R. E., Sutton, R. T., and Anderson, D. L. T. (2002). The effect of El Nino on intraseasonal Kelvin waves. *Quart. J. Roy. Meteorol. Soc.*, 128:1277–1291.

Bergman, J. W., Hendon, H. H., and Weickmann, K. M. (2001). Intraseasonal air-sea interactions at the onset of El Nino. *J. Climate*, 14:1702–1719.

Bigg, G. R. and Blundell, J. R. (1989). The equatorial Pacific Ocean prior to and during El Niño of 1982/83: A normal mode model view. *Quart. J. Roy. Meteorol. Soc.*, 115:1039–1069.

Bjerknes, J. (1969). Atmospheric teleconnections from the Equatorial Pacific. *Monthly Weather Review*, 97:163–172.

Boulanger, J. P., Cravatte, S., and Madec, G. (2003). Reflected and locally wind-forced interannual equatorial Kelvin waves in the western Pacific Ocean. *J. Geophys. Res.*, 108(C10).

Boulanger, J. P., Delecluse, P., Maes, C., and Levy, C. (1997). Long equatorial waves in a high resolution OGCM simulation of the Tropical Pacific during the 1985-1994 TOGA period. *Monthly Weather Review*, 125:972–984.

Boulanger, J. P. and Menkes, C. (1995). Propagation and reflection of long equatorial waves in the Pacific Ocean during the 1992-1993 El Nino. *J. Geophys. Res.*, 100:25041–25059.

Brady, E. C. and Bryden, H. L. (1987). Estimating vertical velocity at the Equator. *Oceanologica Acta*, 10:33–37.

Brentnall, S. J. (1999). *The Impact of the Galápagos Islands on the Dynamics of the Equatorial East Pacific.* PhD thesis, School of Ocean and Earth Science, University of Southampton.

Bryan, K. and Cox, M. D. (1987). A nonlinear model of an ocean driven by wind and differential heating: Part 1. Descriprion of the three-dimensional velocity and density field. *J. Atmos. Sci.*, SP:945–967.

Bryden, H. L. and Brady, E. C. (1985). Diagnostic model of the three-dimensional circulation in the upper equatorial Pacific Ocean. *J. Phys. Oceanogr.*, 15:1255–1273.

Bryden, H. L. and Brady, E. C. (1989). Eddy momentum and heat fluxes and their effects on the circulation of the equatorial Pacific Ocean. *Journal of Marine Research*, 47:55–79.

Busalacchi, A. J. and Cane, M. A. (1985). Hindcasts of sea level variations during the 1982-83 El Niño. *J. Phys. Oceanogr.*, 15:213–221.

Busalacchi, A. J. and Cane, M. A. (1988). The effect of varying stratification on low-frequency equatorial motions. *J. Phys. Oceanogr.*, 18:801–812.

Chang, C. P. (1977). Viscous internal gravity waves and low-frequency oscillations in the Tropics. *J. Atmos. Sci.*, 34:901–910.

Contreras, R. F. (2002). Long-term observations of Tropical Instability Waves. *J. Phys. Oceanogr.*, 32:2715–2722.

Cox, M. D. (1980). Generation and propagation of 30-day waves in a numerical model of the Pacific. *J. Phys. Oceanogr.*, 10:1168–1186.

Cronin, M. F., McPhaden, M. J., and Weisberg, R. H. (2000). Wind forced reversing currents in the western equatorial Pacific. *J. Phys. Oceanogr.*, 30:657–676.

Delcroix, T., Boulanger, J. P., Masia, F., and Menkes, C. (1994). Geosat-derived sea level and surface current anomalies in the Equatorial Pacific during the 1986-89 El Nino and La Nina. *J. Geophys. Res.*, 99:25093–25107.

Delcroix, T., Eldin, G., McPhaden, M., and Moliere, A. (1993). Effects of Westerly Wind Bursts upon the Western Equatorial Pacific Ocean, February-April 1991. *J. Geophys. Res.*, 98:16379–16385.

Delcroix, T. and Picaut, J. (1998). Zonal displacement of the Western Equatorial Pacific Warm Pool. *J. Geophys. Res.*, 103:1087–1099.

Düing, W. P., Hisard, P., Katz, E., Meincke, J., Miller, L., Moroshkin, K. V., Philander, G., Ribnikov, A. A., Voigt, K., and Weisberg, R. (1975). Meanders and long waves in the equatorial atlantic. *Nature*, 257:280–284.

Eriksen, C. C., Blumenthal, M. B., Hayes, S. P., and Ripa, P. (1983). Wind-generated equatorial Kelvin waves observed across the Pacific Ocean. *J. Phys. Oceanogr.*, 13:1622–1640.

Fedorov, A. V., Philander, S. G., Winter, B., and Wittenberg, A. (2002). How predictable is El Niño? *Bull. Amer. Meteor. Soc.*, 84:911–919.

Flament, P. J., Kennan, S. C., Knox, R. A., Niiler, P. P., and Bernstein, R. L. (1996). The three-dimensional structure of an upper ocean vortex in the tropical Pacific Ocean. *Nature*, 383:610–613.

Gaspar, P., Gregoris, Y., and Lefevre, J. M. (1990). A simple eddy-kinetic-energy model for simulations of the ocean vertical mixing: Tests at station Papa and Long-Term Upper Ocean Site site. *J. Geophys. Res.*, 95:16179–16193.

Gent, P. R. and McWilliams, J. C. (1990). Isopycnal mixing in ocean circulation models. *J. Phys. Oceanogr.*, 20:150–155.

Giese, B. S. and Harrison, D. E. (1990). Aspects of Kelvin wave response to episodic wind forcing. *J. Atmos. Sci.*, 95:1761–1780.

Giese, B. S. and Harrison, D. E. (1991). Eastern Equatorial Pacific response to three composite westerly wind types. *J. Geophys. Res.*, 96:3239–3248.

Gill, A. E. (1982). *Atmosphere-Ocean Dynamics.* Academic Press.

Gill, A. E. (1983). An estimation of sea-level and surface current anomalies during the 1972 El Nino and consequent thermal effects. *J. Phys. Oceanogr.*, 13:586–606.

Gill, A. E. (1985). Elements of coupled ocean-atmosphere models for the tropics. *Coupled Ocean-Atmosphere Models*, Elsevier Oceanography Series 40:303–327.

Gill, A. E. and Clarke, A. J. (1974). Wind-induced upwelling, coastal currents and sea-level changes. *Deep-Sea Research*, 21:325–345.

Goddard, L. and Philander, S. G. (2000). The energetics of El Niño and La Niña. *J. Climate*, 13:1496–1516.

Gualdi, S., Navarra, A., and Fischer, M. (2000). The tropical intraseasonal oscillation in a coupled ocean-atmosphere general circulation model. *Geophysical Research Letters*, 26:2973–2967.

Gualdi, S., Navarra, A., and Tinarelli, G. (1999). The interannual variability of the Madden-Julian Oscillation in an ensemble of GCM simulations. *Climate Dynamics*, 15:643–658.

Guilyardi, E., Madec, G., and Terray, L. (2001). The role of lateral ocean physics in the upper ocean thermal balance of a coupled ocean-atmosphere GCM. *Climate Dynamics*, 17:589–599.

Harrison, D. E. (1984). The appearance of sustained equatorial surface westerlies during the 1982 Pacific warm event. *Science*, 224:1099–1102.

Harrison, D. E. (1989). Local and remote forcing of ENSO oceanic waveguide response. *J. Phys. Oceanogr.*, 19:691–695.

Harrison, D. E. and Giese, B. S. (1988). Remote wersterly wind forcing of the eastern equatorial Pacific: Some model results. *Geophysical Research Letters*, 15:804–807.

Harrison, D. E. and Giese, B. S. (1991). Episodes of surface westerly winds as observed from islands in the Western Tropical Pacific. *J. Geophys. Res.*, 96:3221–3237.

Harrison, D. E. and Vecchi, G. A. (1997). Westerly wind events in the Tropical Pacific, 1986-95. *J. Climate*, 10:3131–3156.

Hellerman, S. and Rosenstein, M. (1983). Normal monthly wind stress over the World Ocean with error estimates. *J. Phys. Oceanogr.*, 13:1093–1104.

Hendon, H. H. (2000). Impact of air-sea coupling on the Madden-Julian Oscillation in a General Circulation Model. *J. Atmos. Sci.*, 57:3939–3952.

Hendon, H. H., Liebmann, B., and Glick, J. D. (1998). Oceanic Kelvin waves and the Madden-Julian Oscillation. *J. Atmos. Sci.*, 55:88–101.

Hendon, H. H., Liebmann, B., Newman, M., and Glick, J. D. (2000). Medium-range forecast erors associated with active episodes of the Madden-Julian Oscillation. *Monthly Weather Review*, 128:69–128.

Hisard, H., Meerle, J., and Vioturiez, B. (1970). The Equatorial Undercurrent at 170°E in March and April 1967. *Journal of Marine Research*, 28:281–303.

Inness, P. M. and Slingo, J. M. (2003). Simulation of the Madden-Julian Oscillation in a coupled General Circulation Model. Part I: Comparison with observations and an atmosphere-only GCM. *J. Climate*, 16:345–364.

Inness, P. M., Slingo, J. M., Guilyardi, E., and Cole, J. (2003). Simulation of the Madden-Julian Oscillation in a coupled General Circulation Model. Part II: The role of the basic state. *J. Climate*, 16:365–382.

Jackett, D. R. and McDougall, T. J. (1995). Minimal adjustment of hydrographic profiles to achieve static stability. *Journal of Atmospheric and Oceanic Technology*, 12:381–398.

Johnson, E. S. and McPhaden, M. J. (1993). Structure of intraseasonal Kelvin waves in the Equatorial Pacific Ocean. *J. Phys. Oceanogr.*, 23:608–625.

Johnson, G. C., McPhaden, M. J., Rowe, G. D., and McTaggart, K. E. (2000). Upper Equatorial Pacific Ocean current and salinity variability during the 1996-1998 El Niño-La Niña cycle. *J. Geophys. Res.*, 105:1037–1053.

Josey, S. A., Kent, E. C., and Taylor, P. K. (2002). On the wind stress forcing of the ocean in the SOC Climatology: Comparisons with the NCEP/NCAR,ECMWF,UWM/COADS and Hellerman and Rosenstein Datasets. *J. Phys. Oceanogr.*, 32(7):1993–2019.

Keen, R. A. (1982). The role of cross-equatorial tropical cyclone pairs in the Southern Oscillation. *Monthly Weather Review*, 110:1405–1416.

Kennan, S. C. and Flament, P. J. (2000). Observations of a Tropical Instability Vortex. *J. Phys. Oceanogr.*, 30:2277–2301.

Kessler, W. S. (2001). EOF representations of the Madden-Julian Oscillation and its connection with ENSO. *J. Climate*, 14:3055–3061.

Kessler, W. S. and Kleeman, R. (2000). Rectification of the Madden-Julian Oscillation into the ENSO Cycle. *J. Climate*, 13:3560–3575.

Kessler, W. S. and McPhaden, M. J. (1995). Oceanic Equatorial Waves and the 1991-93 El Niño. *J. Climate*, 8:1757–1774.

Killworth, P. D., Chelton, D. B., and de Szoeke, R. A. (1997). The speed of observed and theoretical long extra-tropical planetary waves. *J. Phys. Oceanogr.*, 27:1946–1966.

Kindle, J. C. and Phoebus, P. A. (1995). The ocean response to operational Westerly Wind Bursts during the 1991-1992 El Niño. *J. Geophys. Res.*, 100:4893–4920.

Kirtman, B. and Vernekar, A. (1993). On wave CISK-and the evaporation-wind feedback for the Madden-Julian Oscillation. *J. Atmos. Sci.*, 50:2811–2814.

Landsea, C. W. and Knaff, J. A. (2000). How much skill was there in forecasting the very strong 1997-1998 El Niño? *Bull. Amer. Meteor. Soc.*, 81:2107–2120.

Latif, M., Sterl, A., Maier-Reimer, E., and Junge, M. M. (1993). Climate variability in a coupled GCM. Part I: The Tropical Pacific. *J. Climate*, 6:5–21.

Lau, K. M. and Chan, P. H. (1988). Intraseasonal and interannual variations of tropical convection: A possible link between the 40-50 day oscillation and ENSO? *J. Atmos. Sci.*, 45:506–521.

Lau, K. M. and Peng, L. (1987). Origin of low-frequency (intraseasonal) oscillations in the tropical atmosphere. *J. Atmos. Sci.*, 44:850–972.

Lau, K. M. and Sui, C. H. (1997). Mechanisms for short-term sea surface temperature regulation: Observations during TOGA COARE. *J. Climate*, 10:465–472.

Lawrence, S. P., Allen, M. R., Anderson, D. L. T., and Llewellyn-Jones, D. T. (1998). Effects of subsurface ocean dynamics on instability waves in the tropical Pacific. *J. Geophys. Res.*, 103(C9):18649–18663.

Lawrence, S. P. and Angell, J. P. (2000). Evidence for Rossby Wave control of Tropical Instability Waves in the Pacific Ocean. *Geophysical Research Letters*, 27:2257–2260.

Legeckis, R. (1977). Long waves in the eastern equatorial Pacific Ocean: A view from a geostationary satellite. *Science*, 197:1179–1181.

Lengaigne, M., Boulanger, J. P., Menkes, C., Madec, G., Delecluse, P., Guilyardi, E., and Slingo, J. (2003). The March 1997 Westerly Wind Event and the onset of the 1997/98 El Niño: Understanding the role of the atmospheric response. *J. Climate*, 16:3330–3343.

Lengaigne, M., Boulanger, J. P., Menkes, C., Masson, S., Madec, G., and Delecluse, P. (2002). Ocean response to the March 1997 Westerly Wind Event. *J. Geophys. Res.*, 107:1179–1181.

Levitus, S. and Boyer, T. (1994). World Ocean Atlas 1994. Tech. Report (Salinity and Temperature). *Tech. Report, US Dept of Commer., Washington DC*, 3-4.

Long, B. and Chang, P. (1990). Propagation of an Equatorial Kelvin wave in a varying thermocline. *J. Phys. Oceanogr.*, 20:1826–1842.

Lukas, R., Hayes, S. P., and Wyrtki, K. (1984). Equatorial sea level response during the 1982-83 El Niño. *J. Geophys. Res.*, 89(C6):10425–10430.

Madden, R. A. and Julian, P. R. (1971). Detection of a 40-50 day oscillation in the zonal wind in the Tropical Pacific. *J. Atmos. Sci.*, 28:702–708.

Madden, R. A. and Julian, P. R. (1972). Description of global-scale circulation cells in the tropics with a 40-50 day period. *J. Atmos. Sci.*, 29:1109–1123.

Madec, G., Delecluse, P., Imbard, M., and Lvy, C. (1998). *OPA 8.1 Ocean General Circulation Model Reference Manual.* Laboratoire D'Ocanographie Dynamique et de Climatologie.

Maes, C., Madec, G., and Delecluse, P. (1997). Sensitivity of an Equatorial Pacific OGCM to lateral diffusion. *Monthly Weather Review*, 125:958–972.

Masina, S. and Philander, S. G. H. (1999). An analysis of tropical instability waves in a numerical model of the Pacific Ocean. 1) Spatial variability of the waves. *J. Geophys. Res.*, 17:29613–29636.

Masina, S., Philander, S. G. H., and Bush, A. B. G. (1999). An analysis of tropical instability waves in a numerical model of the Pacific Ocean. 2) Generation and energetics of the waves. *J. Geophys. Res.*, 17:29637–29661.

Matsuura, T. and Iizuka, S. (2000). Zonal migration of the Pacific Warm Pool tongue during El Niño events. *J. Phys. Oceanogr.*, 30:1582–1600.

McCreary, J. P. (1983). A model of tropical ocean-atmosphere interaction. *Monthly Weather Review*, 111:370–387.

McPhaden, M. J. (1999). Genesis and evolution of the 1997-98 El Niño. *Science*, 283:950–954.

McPhaden, M. J., Busalacchi, A. J., Cheney, R., Douguy, J. R., Gage, K. S., Halpern, D., Ji, M., Julian, P., g. Meyers, Mitchum, G. T., Niiler, P. P., Picaut, J., Reynolds, R. W., Smith, N., and Takeuchi, K. (1998). The Tropical Ocean-Global Atmosphere observing system: A decade of progress. *J. Geophys. Res.*, 103:14169–14240.

McPhaden, M. J., Freitag, H. P., Hayes, S. P., Taft, B. A., Chen, Z., and Wyrtki, K. (1988). The response of the Equatorial Pacific Ocean to a Westerly Wind Burst in May 1986. *J. Geophys. Res.*, 93:10589–10603.

McPhaden, M. J. and Picaut, J. (1990). El Niño-Southern Oscillation displacements of the Western Equatorial Pacific Warm Pool. *Science*, 250:1385–1388.

Megann, A. and New, A. (2001). The effects of resolution and viscosity in an isopycnic-coordinate model of the Equatorial Pacific. *J. Phys. Oceanogr.*, 31:1993–2018.

Moore, A. M. and Kleeman, R. (1999). Stochastic forcing of ENSO by the Intraseasonal Oscillation. *J. Climate*, 12:1199–1220.

Nakamoto, S., Kumar, S. P., Oberhuber, J. M., Ishizaka, J., Muneyama, K., and Fourin, R. (2001). Response of the equatorial Pacific to chlorophyll pigment in a mixed layer isopycnal ocean general circulation model. *Geophysical Research Letters*, 28:2021–2024.

Nakazawa, T. (1988). Tropical super clusters within intraseasonal variations over the western Pacific. *Journal of the Meteorological Society of Japan*, 66:823–830.

National Research Council (1996). Learning to Predict Climate Variations Associated with El Niño and the Southern Oscillation: Accomplishments and Legacies of the TOGA Program.

Neelin, J. D. (1991). The slow sea surface temperature mode and the fast-wave limit: Analytic theory for tropical interannual oscillations and experiments in a hybrid coupled model. *J. Atmos. Sci.*, 48:584–606.

Neelin, J. D. and Cook, K. H. (1987). Evaporation-wind feedback and low frequency variability in the tropical atmosphere. *J. Atmos. Sci.*, 44:2341–2348.

Penland, C., Flugel, M., and Chang, P. (2000). Identification of dynamical regimes in an intermediate couple ocean-atmosphere model. *J. Climate*, 13:2105–2115.

Pezzi, L. P. and Richards, K. J. (2003). The effects of lateral mixing on the mean state and eddy activity of an equatorial ocean. *J. Geophys. Res.*, 108,3371,doi:10.1029/2003/JC001834.

Philander, S. G. H. (1976). Instabilities of zonal equatorial currents. *J. Geophys. Res.*, 81:3725–3735.

Philander, S. G. H. (1978). Forced oceanic waves. *Reviews of Geophysics*, 16:15–46.

Philander, S. G. H. (1979). Equatorial waves in the presence of the Equatorial Undercurrent. *J. Phys. Oceanogr.*, 9:254–262.

Philander, S. G. H. and Pacanowski, R. C. (1980). The generation of equatorial currents. *J. Geophys. Res.*, 85:1123–1136.

Philander, S. G. H., Pacanowski, R. C., Lau, N. C., and Naith, M. J. (1992). Simulation of ENSO with a global atmospheric GCM coupled to a high-resolution, tropical Pacific Ocean GCM. *J. Climate*, 5(4):308–329.

Philander, S. G. H., Yamagata, T., and Pacanowski, R. C. (1984). Unstable air-sea interactions in the Tropics. *J. Atmos. Sci.*, 41:604–613.

Picaut, J. and Delcroix, T. (1995). Equatorial wave sequence associated with Warm Pool displacements during the 1986-1989 El Nino-La Niña. *J. Geophys. Res.*, 100:18393–18408.

Pontaud, M. and Thual, O. (1998). Coupled processes for equatorial Pacific interannual variability. *Quart. J. Roy. Meteorol. Soc.*, 124:527–555.

Qiao, L. and Weisberg, R. H. (1995). Tropical instability wave kinematics: Observations from the Tropical Instability Wave Experiment. *J. Geophys. Res.*, 100:8677–8693.

Richardson, R. A., Ginis, I., and Rothstein, L. M. (1999). A numerical investigation of the local ocean response to Westerly Wind Burst forcing in the Western Equatorial Pacific. *J. Phys. Oceanogr.*, 29:1334–1352.

Salby, M. L. and Hendon, H. H. (1994). Intraseasonal behaviour of clouds, temperature, and motion in the Tropics. *J. Atmos. Sci.*, 51:2207–2224.

Schopf, P. S. and Suarez, M. J. (1988). Vacillations in a coupled ocean-atmosphere model. *J. Atmos. Sci.*, 45:549–566.

Seigel, A. D. (1985). A comment on long waves in the Pacific Ocean. *J. Phys. Oceanogr.*, 15:1881–1883.

Semtner, A. J. and Holland, W. R. (1980). Numerical simulation of equatorial ocean circulation. Part I: A basic case in turbulent equilibrium. *J. Phys. Oceanogr.*, 10:667–693.

Shinoda, T. and Hendon, H. H. (2001). Upper-ocean heat budget in response to the Madden Julian Oscillation in the Western Equatorial Pacific. *J. Climate*, 14:4147–4165.

Slingo, J. M., Rowell, D. P., Sperber, K. R., and Nortley, F. (1999). On the predictability of the interannual behaviour of the Madden-Julian Oscillation and its relationship with El Niño. *Quart. J. Roy. Meteorol. Soc.*, 125:583–609.

Slingo, J. M., Sperber, K. R., Boyle, J. S., Ceron, J. P., Dix, M., Dugas, B., Ebisuzaki, W., Fyfe, J., Gregory, D., Gueremy, J. F., Hack, J., Harzallah, A., Innes, P., Kitoh, A., Lau, W. K. M., McAvaney, B., Madden, R., Mathews, A., Palmer, T. N., Park, C. K., Randall, D., and Renno, N. (1996). Intraseasonal oscillations in 15 atmospheric general circulation models: results from an AMIP diagnostic subproject. *Climate Dynamics*, 12:325–357.

Smyth, W. D., Hebert, D., and Moum, J. N. (1996). Local ocean response to a multiphase westerly wind burst, 1, Dynamic response. *J. Geophys. Res.*, 101:22495–22512.

Stockdale, T. D., D.Anderson, Davey, M., Delecluse, P., Kattemberg, A., Kitamura, Y., Latif, M., and Yamagata, T. (1993). Intercomparison of tropical Pacific ocean GCMs. Technical Report WCRP 79, WMO/TD-545.

Suarez, M. J. and Schopf, P. S. (1988). A delayed action oscillator for ENSO. *J. Atmos. Sci.*, 45:3283–3287.

Torrence, C. and Compo, G. P. (1998). A practical guide to wavelet analysis. *Bulletin of the American Meteorological Society*, 79:61–78.

Vialard, J., Menkes, C., Anderson, D. L. T., and Balmaseda, M. A. (2003). Sensitivity of Pacific Ocean Tropical Instability Waves to initial conditions. *J. Phys. Oceanogr.*, 33:105–121.

Vialard, J., Menkes, C., Boulanger, J. P., Delecluse, P., Guilyardi, E., McPhaden, M. J., and Madec, G. (2001). A model study of oceanic mechanisms affecting Equatorial Pacific sea surface temperature during the 1997-98 El Niño. *J. Phys. Oceanogr.*, 31:1649–1675.

Vitart, F., Balmaseda, M. A., Ferranti, L., and Anderson, D. (2003). Westerly wind events and the 1997/98 El Niño event in the ECMWF Seasonal Forecasting System: A case study. *J. Climate*, 16:3153–3170.

Waliser, D. E., Lau, K. M., and Kim, J. H. (1999). The influence of coupled sea surface temperatures on the Madden-Julian Oscillation: A model perturbation experiment. *J. Atmos. Sci.*, 56:333–358.

Wang, B. and Xie, X. (1998). Coupled modes of the Warm Pool climate system. Part 1: The role of air-sea interaction on maintaining the Madden-Julian Oscillation. *J. Climate*, 11:2116–2135.

Weisberg, R. H. and Qiao, L. (2000). Equatorial upwelling in the Central Pacific estimated from moored velocity profilers. *J. Phys. Oceanogr.*, 30:105–124.

Wolff, J., Maier-Reimer, E., and Legutke, S. (1997). The Hamburg Ocean Primitive Equation Model. Technical Report 13, Deutsches Klimarechenzentrum, Hamburg.

Woolnough, S. J. and Slingo, J. M. (2000). The relationship between convection and sea surface temperature on intraseasonal timescales. *J. Climate*, 13:2086–2104.

Xie, S. P. (1998). Ocean-atmosphere interaction in the making of the Walker Circulation and Equatorial Cold Tongue. *J. Climate*, 11:189–201.

Yoshida, K. (1959). A theory of the Cromwell Current (the EUC) and of the Equatorial Upwelling. *Journal of the Oceanographic Society of Japan*, 15:1–12.

Yu, Z., McCreary, J. P., and Prohel, J. A. (1995). Meridional asymmetry and energetics of Tropical Instability Waves. *J. Phys. Oceanogr.*, 25:2997–3007.

Zhang, C. (1997). Intraseasonal variability of the upper ocean thermal structure observed at 0° and 165°E. *J. Climate*, 10:3077–3092.

Zhang, C. and Gottschalck, J. (2002). SST anomalies of ENSO and the Madden-Julian Oscillation in the Equatorial Pacific. *J. Climate*, 15:2429–2445.

Zhang, K. Q. (1995). *The oceanic response to atmospheric forcing in the Western Equatorial Pacific.* PhD thesis, University of Rhode Island.